Characterization of Process Influences on Microstructure and Mechanical Properties of Long Glass Fiber Reinforced Polyamide 6 Plates in Compounding and Compression Molding

Zur Erlangung des akademischen Grades eines

Doktors der Ingenieurwissenschaften (Dr.-Ing.)

von der KIT-Fakultät für Maschinenbau des
Karlsruher Instituts für Technologie (KIT)

angenommene

Dissertation

von

M.Sc. Christoph Stephan Schelleis

Tag der mündlichen Prüfung	16.10.2025
Hauptreferent	Prof. Dr.-Ing. Frank Henning
Korreferent	Prof. Andrew Hrymak, Ph.D.

Kurzfassung

Das Fahrzeuggewicht beeinflusst erheblich den Energieverbrauch. Strategien zur Gewichtsreduktion sind für eine nachhaltige Mobilität unerlässlich. Der Langfaser-Thermoplast-Direkt (LFT-D) Fließpressprozess erlaubt die wirtschaftliche Produktion maßgeschneiderter Verbundbauteile. Solche Materialinnovationen erfordern eine strukturierte Herangehensweise in der Entwicklung, von der Produktion über die Charakterisierung bis hin zur Bewertung.

In dieser Arbeit wird der Einfluss der Prozessparameter auf mechanische Eigenschaften von glasfaserverstärktem Polyamid 6 untersucht. Eine DoE-Studie zu den Schlüsselfaktoren der LFT-D Extrusion, Polymer Durchsatz, Extruder Drehzahl und Roving Anzahl, wurde durchgeführt. Resultierende Fasergewichtsanteile liegen zwischen 20 % und 60 %. Zug-, Biege- und Schlageigenschaften wurden in Einlege- und Fließbereich charakterisiert und als Qualitätsmerkmale der Studie ausgewertet. Neue Charakterisierungsmethoden entlang der Prozesskette wurden entwickelt.

Die Dichte des Halbzeuges, des Plastifikates, wurde charakterisiert und als inhomogen befunden. Eine Fließstudie wurde durchgeführt und charakterisiert. Die Fließfront des LFT-D Materiales ist aufgrund des Dichtegradienten im Plastifikat schief. Dies wiederum ist die Ursache für gemessene Faserorientierungsabweichungen im Fließbereich. Der Fasergehalt entmischt und steigt zum Ende des Fließwegs kontinuierlich an. Alle Eigenschaften und Abweichungen der LFT-D Mikrostruktur werden im Hinblick auf Faktoreinflüsse diskutiert.

Die Auswertung der DoE-Studie führt zu keiner klaren Faktorempfehlung. Eine hohe Roving Anzahl hat jedoch die meisten negativen Wechselwirkungen, und entsprechend sollte die Extruder Drehzahl auf ein mittleres bis hohes Niveau eingestellt werden. Mehr als die Faktoren beeinflusst der Fasergehalt alle Eigenschaften, sowohl mechanisch als auch mikrostrukturell. Mit diesem hier präsentierten Rahmen können neue LFT-D Materialkombinationen effizient und ganzheitlich abgemustert, charakterisiert und bewertet werden.

Abstract

Vehicle weight significantly influences energy consumption. Lightweighting strategies are essential for weight reduction. The long fiber thermoplastic direct (LFT-D) compression molding process is characterized by the economical production of thin composite parts. Material innovations require a development framework from production over characterization to evaluation.

This work revolves around the material characterization during process factor optimization for a compression molded glass fiber reinforced polyamide 6 composite. A DoE study with key LFT-D extrusion factors, polymer throughput, screw speed, and roving amount, was conducted. Resulting fiber weight contents range from 20 % to 60 %. Tensile, flexural and impact properties were characterized in flow direction and chosen as quality features in the DoE evaluation. New characterization methods were developed and are presented here.

The density of the semi-finished material, the plastificate, was characterized and found to be inhomogeneous. A short-shot study was conducted, and flow front skewness was characterized. This skewness was found to originate in the density differences along the extrusion direction of the plastificate. This skewness is, in turn, the origin of fiber orientation deviations in the flow area after molding. Fiber content is migrating towards the end of the flow path during compression molding. All properties of the LFT-D microstructure are discussed with regards to factor influences.

Neither coefficient nor response contour plots offer a clear factor recommendation. A high roving count, however, has the most negative interactions and accordingly, the screw speed should be set at a medium to high level. More than processing factors, the fiber content is the decisive influence on all properties, mechanically and microstructurally. In this framework presented here, new LFT-D material combinations can be processed and characterized in an efficient and holistic manner.

Table of Contents

Index of Figures

Index of Tables

Index of Abbreviations

µCT	Micro-computed tomographical
ABS	Acrylonitrile butadiene styrene
ASTM	American Society for Testing and Materials
C	Charge area
Co	Continuous (fiber reinforced)
CV	Coefficient of variation
DiCo	Discontinuous (fiber reinforced)
DIN	Deutsches Institut für Normung
DoE	Design of Experiments
EN	Europäische Norm (Euronorm)
F	Flow area
FASEP	Is not an abbreviation
FCCCD	Face-Centered-Central-Composite-Design
FIP	Fraunhofer Innovation Platform
FLD	Fiber length distribution
FO	Fiber orientation
FOD	Fiber orientation distribution
FRP	Fiber reinforced polymer
GFA	Gleichlauf Förderelemenent Auskämmend
GFM	Gleichlauf Förderelemenent Mischend
GMT	Glass mat thermoplast
ICT	(Fraunhofer) Institute of Chemical Technology
ILC	In line compounding
IQR	Interquartile range
IRTG	International Research Training Group
ISO	International Organization for Standardization
LFT	Long fiber (reinforced) thermoplast
LFT-D	LFT-Direct (process)
NDT	Non destructive testing
PA6	Polyamide 6
PA66	Polyamide 66
PC	Polycarbonate
PET	Polyethylene terephthalate
PP	Polypropylene
SAN	Styrene acrylonitrile resin

SD	Standard deviation
SFT	Short fiber (reinforced) thermoplast
SME	Specific mechanical energy
TGA	Thermogravimetric analysis
TSE	Twin screw extruder
ZSE	Zweischneckenextruder (german for TSE)
ZSG	Zweischnecken “Gerät” (Dieffenbacher TSE)

Index of Symbols

Symbol	Description	Unit
Uppercase letters		
A_1	Conveying parameter	-
CV	Coefficient of variation	%
D	Extruder housing diameter	mm
E	Young's modulus	GPa
E^*	Pseudo Young's modulus	GPa
E_f	Young's modulus of the fiber	GPa
E_m	Young's modulus of the matrix	GPa
F_{max}	Maximum force	kN
H_0	Null hypothesis	-
H_a	Alternative hypothesis	-
L	Clamping height (tensile testing)	mm
M_f	Fiber mass	kg
M_p	Polymer mass	kg
M_{TSE}	Torque at screw	Nm
$\dot{Q}$	Total throughput	kg/h
$\tilde{Q}^*$	Simplified throughput ratio	g
R	Lankford coefficient	-
R_a	Axis ratio	-
SME	Specific mechanical energy	kWh/kg
$T_{mold,l}$	Lower mold temperature	°C
$T_{mold,u}$	Upper mold temperature	°C
Tt	Linear fiber density	Kg/km
T_{Zx}	Temperature in Zone x	°C
$\dot{V}^*$	Dimensionless throughput ratio	-
V_s	Substitute volume element	cm³
Lowercase letters		
$\%pt.$	Percentage points	-
a_r	Aspect ratio	-
d_b	Diameter of the extruder barrel	mm

Symbol	Description	Unit
d_f	Fiber diameter	mm
h	Sample thickness	mm
l_{crit}	Critical fiber length	mm
l_f	Fiber length	mm
l_n	Number averaged fiber length	mm
l_w	Weight averaged fiber length	mm
m_f	Fiber mass (throughput)	kg/h
m_{LFT-D}	LFT-D mass (throughput)	kg/h
m_p	Polymer mass (throughput)	kg/h
n_{rov}	Fiber roving amount	-
n_{TSE}	TSE screw speed, general	rpm
n_{TSE2}	Screw speed of the ZSG extruder	rpm
p	Polydispersity	-
$\mathbf{p}$	Unit vector	-
r	Radius	mm
r_f	Fiber radius	mm
s_{ff}	Flow-front skewness	%
t_{res}	Residence time	s
v_f	Fiber volume fraction	%
v_{intake}	Fiber intake speed	m/rev
$\boldsymbol{v}_m$	Material velocity	m/s
w_b	Bracket width (tensile test)	mm
w_f	Fiber mass fraction	%
Greek letters		
μ	Mean value of a standard distribution	-
$\dot{\gamma}$	Shear rate (mold)	1/s
$\Delta\rho$	Density gradient	kg/m³
ε	Strain	%
η	Viscosity	Pa s
ρ_f	Fiber density	kg/m³
ρ_{LFT}	Density of LFT	kg/m³
ρ_p	Polymer density	kg/m³
ρ_{plast}	Plastificate density	kg/m³
σ	Standard deviation	-
σ	Tensile strength	MPa
σ_B	Tensile strength at break	MPa

Symbol	Description	Unit
σ_f	Fiber tensile strength	MPa
σ_F	Flexural strength	MPa
σ_I	Impact strength	kJ/m²
σ_M	Maximum tensile strength	MPa
τ	Shear rate (extruder)	1/s
τ_y	Interfacial shear strength	MPa
φ	Fiber orientation	°
ϕ	Tensile disc orientation angle	°
φ_v	Main fiber orientation	°
ψ_φ	Distribution function of fiber orientations	-
θ	Fracture angle	°
indices		
$()_{calc}$	A calculated value	-
$()_{charge}$ or $()_C$	Concerning the Charge area	-
$()_{flow}$ or $()_F$	Concerning the Flow area	-
$()_{max}$	A maximum	-
$()_{mean}$	A mean value	-
$()_{min}$	A minimum	-
$()_{nominal}$	A theoretical value (eg. datasheet)	-

Preface

This work was written during my time as a researcher at both the Fraunhofer Institute for Chemical Technology ICT and Karlsruhe Institute of Technology KIT. I would like to thank my supervisor Prof. Frank Henning for all the resources and the freedom granted during the preparation of the thesis. I equally thank Prof. Andrew Hrymak for many words of encouragement and interest in this work.

In the framework of the DFG IRTG “Integrated engineering of continuous-discontinuous long fiber reinforced polymer structures” under the leadership of Prof. Thomas Böhlke, I enjoyed many in-depth discussions with my esteemed colleagues Juliane Blarr, Benedikt Scheuring, Louis Schreyer and Nicolas Christ. I would like to thank Benedikt especially for supporting sample preparation and characterization for this thesis.

Thank you, Jonathan Haas and Michael Wilhelm for keen eyes and honest commentary. Andreas Menrath for suggesting the IRTG in the first place and letting me balance my work as needed. Björn Beck for his support and for proofreading the thesis. Stephan Ihle for his eye for detail and technical discussions during all our LFT-D trials. Thank you, my students, Yoshihiko Kobayashi, Sven Löwe, Luca Meckes and all other researchers and technicians who contributed to this work.

Thank you, dear parents, for your unconditional and everlasting support no matter what.

Thank you, Jennifer, for being more than patient with me while I went through the ups and downs of this project. I am eternally grateful for your support.

Karlsruhe, May 2025

Christoph Schelleis

1 Motivation

Overconsumption of limited resources (Wackernagel et al. 2002) and climate change seemingly out of control (O'Neill and Oppenheimer 2002, p. 1972) have resulted in great societal pressure on political decision-making. Billion Euro Initiatives like the European Unions “Green Deal” call for a carbon neutral European continent by 2050. On this trajectory, passenger cars as well as light commercial vehicles shall be zero emission by 2035 (Regulation (EU) 2023/851).

Mobility has been a driver for prosperity and the number of motorized vehicles is predicted to increase. Independent of propulsion, be it fossil fueled or electrified, vehicle weight is a key determining factor of energy consumption and application of targeted lightweighting strategies is the way to weight reduction. One such strategy is material lightweighting where requirements are met by the lightest possible material. (Henning and Moeller 2020, p. 57 ff.)

Composites are defined as a synergy between substantially different components that make up a product better than its constituents (Gandhi et al. 2020, p. 1). It is a collective term for well-established engineering materials with a worldwide market volume of around thirteen million tons in 2022. In that year the European composite market share accounted for 22 % of the world market similar to the American market with Asia leading composite production by tonnage. (Witten and Mathes 2023, p. 5)

Used by mankind for thousands of years in various forms, nowadays and especially in context of this work, “composite” is limited to the combination of a polymer matrix system and a fiber reinforcement. Fiber reinforced polymers (FRP) can be classified according to their fiber length in continuous (Co) and discontinuous (DiCo) FRPs (Böhlke et al. 2019). Key advantages, and subsequently uses, of DiCo FRPs are tailored, good material properties, low costs and high-volume production capability (Gandhi et al. 2020, p. 9). These advantages combined with high integration potential in comparison to other

available materials lead to ever growing use in technical applications (Schemme 2008, p. 34).

The automotive sector is a high-volume market with high initial costs for development and processing equipment but low costs per part due to economy of scale. The choice of processing route is a crucial decision that is highly specific to every product, quantity and quality.

Demand for mass production of, often brand independent, parts restricts the process selection (Kampker and Heimes 2024, p. 88). In FRP production only highly automated processing routes, injection, and compression molding of various semi-finished materials remain feasible.

Good mechanical performance position long fiber thermoplastic (LFT) compression molding materials between the advantages of injection molding (e.g. high flowability and complex moldability) and glass mat reinforced thermoplasts (GMT) (e.g. high mechanical properties). The LFT-Direct (LFT-D) compression molding process is characterized by short cycle times, economical production of thin parts (AVK-Industrievereinigung Verstärkte Kunststoffe e.V. 2014, p. 429; Henning et al. 2005, p. 29) and an inherent ability to include recyclates in the compounding process (Henning 2001). Compression molding causes less fiber damage than injection molding because of lower shear forces during mold filling, leading to higher fiber lengths and mechanical properties (Henning et al. 2005, p. 30). Cost advantages over other compression molding materials derive from the in-line production of the semi-finished material directly from raw materials (AVK-Industrievereinigung Verstärkte Kunststoffe e.V. 2014, p. 438).

2 State of the Art

DiCo FRPs are, by definition, limited in fiber length. These fiber lengths are greatly affected by processing route chosen and will, in turn, affect FRP mechanical properties. A detailed, experiment-based investigation of parameters affecting composite quality was given in various publications by Thomason for short fiber reinforced polypropylene (PP)[1] and polyamide (PA)[2]. These studies serve as an illustrative template where fiber fraction, fiber length distribution (FLD) and fiber orientation distribution (FOD) were identified among the crucial factors and optimization goals for DiCo FRP (Thomason 2005, p. 998).

In this chapter, the basic concepts of composites are discussed, starting from the relevance of fiber morphology and what general influences on morphology are known. Processing of composites in extrusion and compression molding will be discussed, with a special focus on microstructure during and after the process. A comprehensive overview of process and material developments of LFT-D materials is given. Rounding off the chapter is a list of open questions in research and a formulation of the goals of this work.

2.1 Fiber Fraction

The relation of both FRPs constituents, matrix and fiber, can be expressed in fiber fraction by mass w_f or volume v_f in percent (ISO 80000-1). The usage of mass fraction is often process driven as in production the mass of the material is regulated. Fiber mass fraction w_f is calculated from the fiber mass M_f and polymer mass M_p according to the following equation (2.1).

1 Thomason 2002, 2005; Thomason and Groenewoud 1996; Thomason and Vlug 1996, 1997; Thomason et al. 1996.

2 Thomason 2006, 2007.

$$w_\mathrm{f} = \frac{M_\mathrm{f}}{M_\mathrm{f} + M_\mathrm{p}}$$

(2.1)

Fiber volume fraction v_f is used in theoretical considerations and to compare different material systems as w_f is dependent on the densities (and thus also the volume) ρ_f of the fiber and ρ_p of the polymer material. Conversion from w_f to v_f is done via equation (2.2) (Osswald and Menges 2012, p. 401).

$$v_\mathrm{f} = \frac{w_\mathrm{f}}{w_\mathrm{f} + (1 - w_\mathrm{f}) \cdot \frac{\rho_\mathrm{f}}{\rho_\mathrm{p}}}$$

(2.2)

2.1.1 Influence of Fiber Fraction on Mechanical Properties

Theoretical considerations like the Halpin-Tsai model for aligned FRPs show that elastic modulus in fiber direction is directly related to v_f (S. Tsai and N. Pagano 1968). The stiffness for a quasi-isotropic short fiber material follows the same principles (Halpin and Pagano 1969, p. 720). Findings are backed up in experiments (Osswald and Menges 2012, p. 401).

Increasing v_f will, in principle, increase the mechanical properties of a DiCo FRP up to some point (Tucker 2022, p. 258). In reality, fiber morphology will not be homogeneous and FRP performance will depend on the distributions of fiber length and orientation, both influenced by v_f (Gandhi et al. 2020, p. 21), as will be touched upon in the next paragraphs. Processing FRPs from continuous fiber rovings, not ideal filaments, fibers tend to concentrate in bundles that will lead to reduced mechanical performance (Gandhi et al. 2020, p. 111; Rohde-Tibitanzl 2015, p. 95). Visualizing relative performance of mechanical properties in Figure 2.1 a qualitative picture can be formed (Gandhi et al. 2020, p. 113).

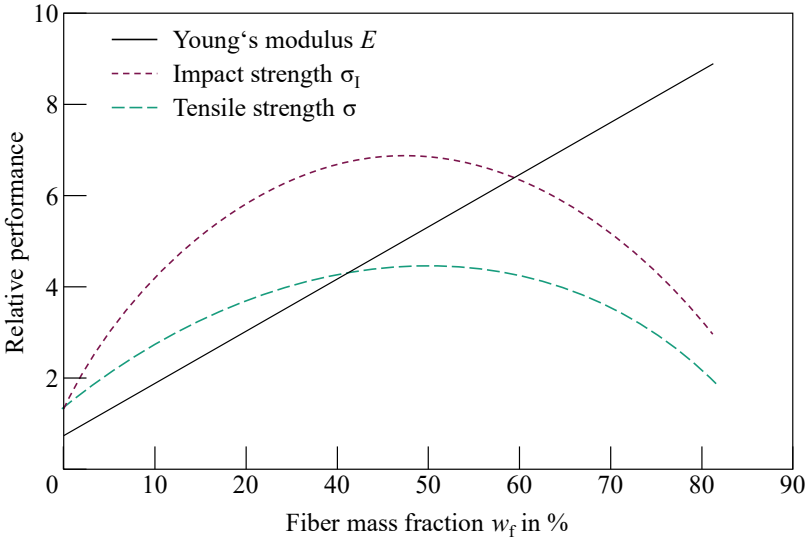

Figure 2.1 Qualitative progression of relative mechanical performance for different properties shown over w_f. Adapted from (Thomason 2007).

While modulus increases steadily with w_f, strengths do hit a maximum between $w_f = 40$ to 50 % as was experimentally shown by Thomason for injection molded FRP materials (Thomason 2005). Impact strength is more strongly influenced by w_f than tensile strength.

2.1.2 Measuring Fiber Fraction

Thermogravimetry (TGA) can be used to determine fiber fraction. Samples are placed in a crucible and burned at high temperatures. The change in sample weight over time is tracked and once the matrix material is burned off M_f is known and w_f can be calculated. (Osswald and Menges 2012, p. 104)

2.2 Fiber Length

Fiber length l_f is another important aspect of FRP. While improving mechanical properties, longer fibers are more difficult to process, an optimization problem (Thomason 2005, p. 996). The impact of l_f on mechanical properties is discussed. Measuring techniques for l_f and characteristic parameters are introduced.

2.2.1 Influence of Fiber Length

Important factors in addition to l_f in FRP, include the aspect ratio a_r, the ratio of l_f and fiber diameter d_f (Cox 1952).

$$a_r = \frac{l_f}{d_f} \tag{2.3}$$

For large a_r, stiffnesses of DiCo FRP plateau at values similar to Co FRP. This plateau depends on constituent stiffnesses as well as modulus of fiber E_f and matrix E_m. (Halpin and Pagano 1969, p. 721)

Classification of polymer fiber suspensions

Polymer fiber suspensions can be categorized into three regimes via the relation of the dimensionless quantities v_f and inverse a_r. In the dilute regime, defined as $v_f < (d_f/l_f)^2$ the distance between fibers is greater than l_f. Fibers can rotate freely, and interactions are rare. Folgar and Tucker noted the rare use of dilute suspensions in commercial applications. The highly concentrated regime is defined as $v_f > (d_f/l_f)$. The room for fiber movement is in the order of d_f. The semi-concentrated regime lies in between dilute and highly concentrated and is thus defined by $(d_f/l_f)^2 < v_f < (d_f/l_f)$. (Folgar and Tucker 1984, p. 99)

Fiber diameters for industrial applications are set in a certain range and cannot be influenced in processing. Diameters of reinforcement fibers for FRP are usually in the range 5 µm to 20 µm (Teschner 2021, p. 254). Thus, the focus in

FRP processing remains on l_f. When l_f increases, the possibilities for interactions as well as bundling increase as well (Gandhi et al. 2020, p. 20). This will negatively affect mechanical properties. Shorter l_f can orient themselves better in material flow improving modulus without changing strength and impact properties (Priebe and Schledjewski 2011, p. 378).

Qualitatively illustrating these connections is Figure 2.2., where relative mechanical properties with respect to l_f are shown. Note the logarithmic scale of l_f. While, in theory, steadily increasing modulus and strength with longer fibers, the fibers will bundle and restrict their movement and alignment. With bundles present, tensile performance is impaired, indicated by dashed lines. This bundle effect is absent if only l_f is considered. (Gandhi et al. 2020, p. 323) Because properties converge towards their maximum over large sections of l_f, a 95 % level is introduced to define realistic l_f limits for different load types.

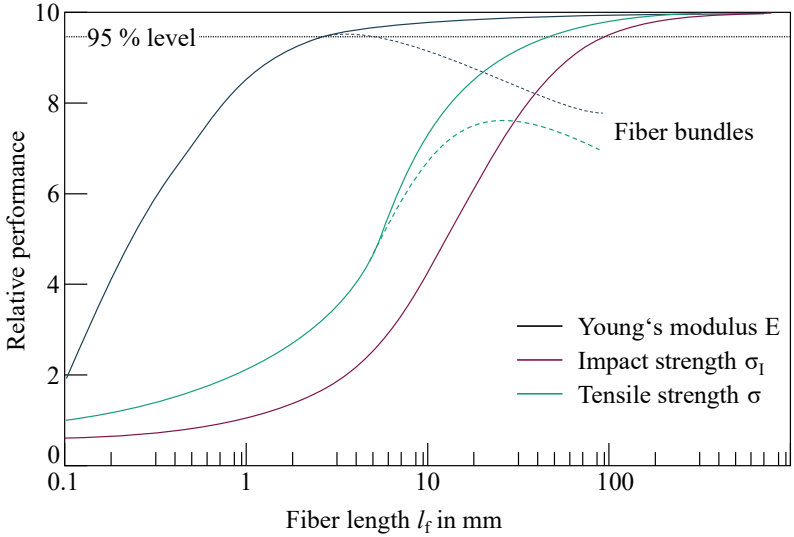

Figure 2.2 Relative mechanical performance for different properties shown with respect to l_f. The 95 % level is reached at different l_f. Fiber bundling impedes performance gain indicated by dashed lines. Adapted from (Gandhi et al. 2020, p. 323).

2.2.2 Measuring Fiber Length

A comprehensive study of existing characterization methods was conducted by Goris et al. (Goris et al. 2018). Most methods rely on separating fiber and matrix material either by chemical means or by a preceding characterization of fiber fraction via TGA for example. An image of the fibers is taken and analyzed by suitable software. (Goris et al. 2018, p. 4059)

Due to the sheer number of fibers present, a selection or subsampling step is often needed. Here, a great deal of inaccuracy is introduced and a bias towards longer (Nguyen et al. 2008; Nghiep Nguyen et al. 2009) or shorter (Bondy et al. 2017, p. 193) fibers is suspected.

The single viable, commercially available, method identified by Goris et al characterizing l_f is FASEP (not an abbreviation) because following a formalized subsampling method allows for qualitative comparisons (Goris et al. 2018, p. 4068). FASEP is a semi-automated image processing method for l_f analysis (Hartwich et al. 2009, 738921-1).

When comparing actual mechanical properties achieved with measured l_f, Bondy et al. found that much longer fibers should have been present according to calculations (Bondy et al. 2017, p. 195). Other sources in the LFT-D space cast doubts on the validity of measured l_f as they were expected to be higher every time, as the corresponding mechanical properties did not match and inferred a longer mean FLD (Radtke 2009, p. 54). Overall, fiber length measurement methods for long l_f are subject to research and improvement.

2.2.3 Characteristic Parameters in Fiber Length Discussion

The l_f measurement of DiCo FRP is not a single value but a distribution (FLD) in the form of a histogram of all fibers N comprising all measured l_f. A key figure in this context is the number average fiber length l_n calculated via equation (2.4) (Gandhi et al. 2020, p. 97)

$$l_{\mathrm{n}} = \frac{\sum_{i=1}^{n}(l_i \cdot N_i)}{\sum_{i=1}^{n}(N_i)}$$

(2.4)

Where the totality of fibers N is divided into n buckets (ranges of l_{f}). Every bucket comprises N_i fibers with length l_i. Comparisons with experiments have shown that l_{n} is an inappropriate basis for calculating mechanical properties as they are disproportionately influenced by longer fibers (Inceoglu et al. 2011, p. 1844). To account for the characteristic shape of the FLD, a sharp peak followed by a long tail, one can calculate the weight average fiber length l_{w} (2.5) (Gandhi et al. 2020, p. 97).

$$l_{\mathrm{w}} = \frac{\sum_{i=1}^{n}(l_i^2 \cdot N_i)}{\sum_{i=1}^{n}(l_i \cdot N_i)}$$

(2.5)

Parameters l_{n} and l_{w} are equal if all fibers have the same length, and in all other cases l_{w} will exceed l_{n} (Yilmazer and Cansever 2002, p. 62). The ratio of l_{n} and l_{w} is the polydispersity p which is a measure for FLD broadness (Barbosa and Kenny 2000, p. 21).

$$p = \frac{l_{\mathrm{w}}}{l_{\mathrm{n}}}$$

(2.6)

In FRPs the load is transferred from the weaker matrix to the stronger fiber reinforcement over the entire length of the fiber (Osswald 2018, p. 42). The load is not transferred equally over the entire length, but mostly at the free ends dropping off completely towards the middle of the fiber. The length needed to transfer the entire load is the critical fiber length l_{crit}.

$$l_{\mathrm{crit}} = \frac{\sigma_{\mathrm{f}} \cdot r_{\mathrm{f}}}{\tau_{\mathrm{y}}} \tag{2.7}$$

with fiber tensile strength σ_f, fiber radius r_f and interfacial shear strength τ_y, as defined by Kelly and Tyson (Kelly and Tyson 1965, p. 343). Above l_{crit} the fiber will break in tension mode while under l_{crit} the fibers will be pulled out of the matrix (Fliegener 2015, p. 145).

Classification of DiCo FRP

In literature and advertisement various definitions and delimitations between short and long FRPs exist. What constitutes a "long" fiber might sometimes be incentivized by monetary interest (Schemme 2008, p. 33).

Classification between short fiber thermoplastics (SFT) and LFT can be done by absolute l_f. A $l_f = 5$ mm is presented as a delimitation by Oelgarth et al. referencing the then state of the art (Oelgarth et al. 1998, p. 480). Another commonly used demarcation is $l_f = 1$ mm (Inceoglu et al. 2011, p. 1845). Other ranges exist, for example l_f between 3 mm and 25 mm (Thattaiparthasarathy et al. 2008, p. 1512) and even 50 mm (Teschner 2021, p. 242). This approach seems arbitrary.

Another approach is to classify by aspect ratio, a_r, (2.3) which considers fiber diameter. Here, $a_r >= 100$ is proposed by Cox as he found the load transfer between fiber and matrix plateaus here and strengths do only marginally increase for longer l_f (Cox 1952, p. 79). This a_r is accepted and repeated in literature. However, critical a_r depends on fiber and matrix properties (Halpin and Pagano 1969, p. 721). Commonly used (glass-) fiber systems have diameters of $d_f = 10$ to 20 µm. Calculating the resulting fiber length with $a_r = 100$ would put the demarcation line between $l_f = 1$ to 2 mm as noted by Henning et al.. The frame of reference, the production process, is disregarded. Fiber lengths of 1 mm, considered long for injection molding, would be perceived short for compression molding processes. (Henning et al. 2005, pp. 24–25)

The third possibility is to check whether l_f, or a relevant portion of l_f, exceeds l_{crit} (2.7) so that the maximum reinforcement effect is attained (Osswald 2018, p. 43). This considers actual material combinations instead of blanket assumptions.

2.3 Definition and Influence of Fiber Orientation

While fiber orientation can be defined in three dimensions, a simplified planar approach shall suffice for this work. Here the orientation is described by angle φ and a unit vector **p** comprising dependent components *p1*, *p2* and *p3* with *p3* = 0 (making it planar). FRPs contain thousands of individual fibers. Instead of describing all orientations, many φ can be measured and displayed as a histogram serving as a discrete approximation of the FOD function $\psi_\varphi(\varphi)$. (Tucker 2022, p. 12 f.) Existence of a distribution indicates that fibers are not fully aligned. The dispersity of ψ_φ increases with v_f as well as a_r (Folgar and Tucker 1984, p. 117). The vertex of $\psi_\varphi(\varphi)$ is at the angle φ_v also called main fiber orientation. A measure of anisotropy *R* is the Lankford coefficient denoting orientation dependent properties in rolled steel (Lankford et al. 1950).

2.3.1 Influence of Fiber Orientation

Reinforcement effects are strongest in φ_v and drop off deviating from load direction. Following Figure 2.3 illustrates qualitative correlations. Shorter fibers, a few hundred microns, can orient themselves better as smaller a_r allow for higher mobility (cf. 2.2.1 (p. 6)) and are more sensitive to the relation of load direction to φ_v. Calculating *R* for the anisotropy between 0° and 90°, R_{90} would be higher for lower l_f as the drop off is stronger (cf. Figure 2.3 differences of solid and dashed curve between 0° and 90°).

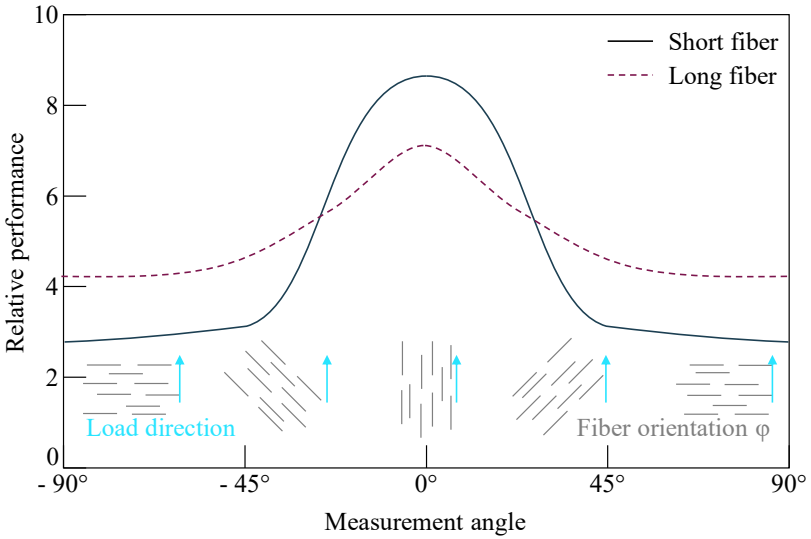

Figure 2.3 Relative mechanical performance for short and long fiber depending on fiber orientation, load direction and measurement angle. Adapted from (Gandhi et al. 2020, p. 21).

2.3.2 Measuring Fiber Orientation

Fiber orientation can be determined with various testing methods, destructive as well as non-destructive testing (NDT). Composites can be sliced, polished, and evaluated under a microscope. On polished cross section surfaces, fibers present as oval shaped areas. Fiber orientation can be determined by basic math evaluating the major axis of the ellipses (Folgar and Tucker 1984, p. 100; Barbosa and Kenny 2000, p. 12). Micro-computed tomographical (µCT) scans can be done for small subsections to derive FOD (Garesci and Fliegener 2013, p. 145; Perez et al. 2013, p. 1121; Blarr et al. 2024, p. 120).

Both methods presented require preparation and characterization work and, in part, specialized equipment followed by evaluation algorithms. The correlation of mechanical properties and fiber orientation is well established in the state of the art (Folgar and Tucker 1984, pp. 98–99).

Tensile discs

Tensile discs are flat circular specimens used in a NDT method introduced by Tröster (Tröster 2004). Discs (r = 170 mm) are clamped in a testing machine, loaded in the linear elastic range up to ε = 0.3 % strain, relaxed and rotated in 10° increments to be tested again. The resulting force-displacement curve is attributed to a substitute material volume V_s spanned between the bracket width of the testing machine w_b, clamping height L and sample thickness h. Not congruent to the definition of Young's modulus E, Tröster called the derived property "pseudo E-Modul" or E*. (Tröster 2004, p. 84)

Plotting an entirely characterized disc in a polar plot shows the resulting ellipse to be axially symmetrical with the major axis shifted out of the nominal material flow direction of 0°. Correspondingly the lowest stiffness is found at the co-vertex shifted out of the 90° alignment of the cross-flow direction. Material anisotropy (R) can be derived from the ratio of these axes. (Tröster 2004, p. 85 f.)

Tröster concluded the main fiber orientation φ_v direction to be parallel to the major axis of the ellipse (Tröster 2004, p. 86). Derived φ_v was validated by microwave raster image method (Tröster 2004, p. 93) as well as radiography followed by image processing software FIBORAS (Tröster 2004, p. 94).

Radtke extensively used tensile discs and expanded the scope of application to flexural testing (Radtke 2009). Fiber interaction coefficients and applicability of the testing method was validated by coupled mold filling and structural simulation (Radtke 2009, p. 83). Tensile and flexural discs were successfully simulated and deviations from characterizations were found to be less than 5 % (Radtke 2009, p. 87). Work on tensile discs was further conducted by Maertens (Maertens 2022) as well as Scheuring (Scheuring 2024).

2.4 Fiber Degradation Mechanisms

Literature addresses three main mechanisms of fiber degradation resulting from fiber interactions (Rohde-Tibitanzl 2015, p. 5; Gandhi et al. 2020, p. 96):

- Fiber-Fiber: When colliding, fibers break due to bending and friction.
- Fiber-Polymer: Hydrodynamic force causes fibers to break.
- Fiber-Machine: Collision with housing, screw elements etc..

Fiber-fiber interaction

With rising w_f in the FRP the opportunity for this type of interaction increases and additional fiber damage must be expected (Goris et al. 2018, p. 4068). Additionally, l_f, via a_r, increases the opportunities for fiber-fiber interaction because the fiber rotation takes up more volume in which a collision can happen (Folgar and Tucker 1984, p. 99) (cf. Classification of fiber polymer suspensions in 2.2.1 (p.6)).

Fiber-polymer interaction

Fibers in polymer melt are subjected to deforming stresses during compounding and molding. Bending and buckling was described by Forgacs et al. as the main reason for fiber fracture dependent on fiber a_r and polymer viscosity η (Forgacs and Mason 1959, p. 471).

Fiber-machine interaction

As with fiber polymer interaction, contact with the machine, housing as well as screw or die, will damage l_f. Especially if fibers are embedded in semi-molten polymer, as is the case with processing LFT pellets in the feeding zones. Here, the biggest initial fiber damage is to be expected (Bumm et al. 2012, p. 2147; Kohlgrüber 2016, p. 624).

The same is observed as fibers interact with freezing polymer in the mold. Fibers are subjected to pull out as well as breakage when the melt is moved parallel to the solid sections close to the mold surface. (Goris and Osswald 2018, p. 332). This is elaborated further in 2.6.1 (p.25).

2.5 LFT-Direct and In Line Compounding Process

In Europe, thermoplastic composite materials were on the rise in the last years accounting for around 60 % of market share focused on automotive and electronics applications. Of this amount, SFTs account for 90 % of European thermoplastic composite production. (Witten and Mathes 2023, p. 11)

Commodity polymers dominate the entire market down to the LFT segment where 65 % of products are PP-based, 20 % are PA-based with specialty materials making up the rest (Ning et al. 2020, p. 164).

Processing options for LFT materials are diverse and can be broadly categorized by way of molding, either in injection or compression molding process, and nature of raw materials (Schemme 2008, p. 33). Direct processing of LFT materials appeared in the 1990s when compounding directly from raw materials and part production was coupled, cutting out semi-finished products and saving costs (Schemme 2008, p. 37).

A note on the use of terminology in this work

LFT-Direct (LFT-D) or LFT In Line Compounding (ILC) are specialized processes comprising two twin screw extruders (TSE). A differentiation between these abbreviations was given by Henning and refers to processing a premixed matrix system directly (LFT-D) and compounding the matrix with additives “in line” (Henning 2001, p. 6). Though differently named, both routes work on the same machine.

This work deals with LFT materials processed in the LFT-D process. While various definitions of those abbreviations exist, in this work, LFT-D shall be used for the specific production process where LFT-D material is produced in the form of a plastificate. The designation “-D” for semi-finished material and products of the process is deliberately continued to ease the differentiation between general findings for LFT materials (including injection molding materials) and findings specifically for this process variant with compression molding.

2.5.1 Processing Scheme of a Dieffenbacher LFT-D Line

A schematic depiction of the LFT-D process is given in Figure 2.4 (modified from (Schelleis et al. 2023c, p. 2043)). The first TSE (TSE1) is an industry standard compounding extruder tasked with homogenization and melting the granulates fed gravimetrically at the beginning of the process (Eyerer et al. 2006, p. 1). Connected perpendicularly in series it provides a melt film at the transition to the second TSE (TSE2). This is the mixing extruder where the continuous fiber rovings are incorporated at the same time. Semi-finished LFT-D is shaped in the die at the end of TSE2 and transferred onto a heated chain belt. Until the material is cut to length it is enveloped by an insulated tunnel with infrared heaters to avoid cooling of the material. Once enough material is compounded and cut it is transferred into a press for compression molding. (Henning et al. 2005, pp. 26–29)

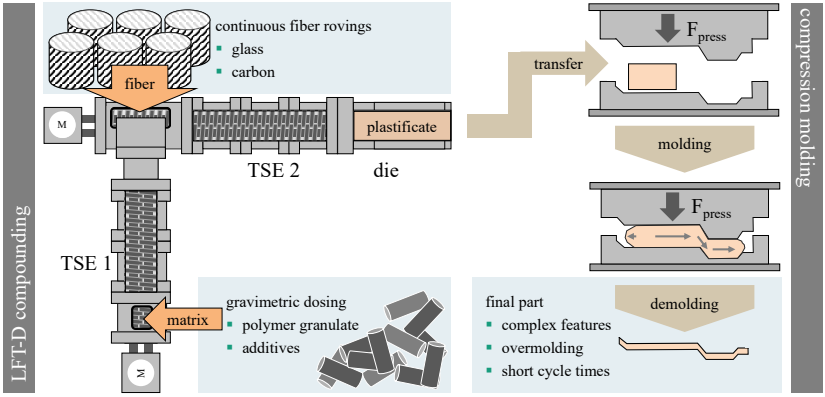

Figure 2.4 Schematic depiction of the LFT-D process (left) with subsequent compression molding step (right). Based on (Schelleis et al. 2023c, p. 2).

Since its first patent in 1944 nearly every polymer is processed on some form of extruder (Kohlgrüber 2016, p. 12). Twin screw extruders comprise two co-rotating screws. Screws are modular in design comprising elements that can be classified by their geometry and task. The base element of any extruder is the

conveying element GFA[3]. This element moves an amount of material per revolution. Another commonly used element is a mixing element GFM[4], here the stream of material is split and diverted to achieve mixing effects. Kohlgrüber's work on Co-Rotating TSEs is recommended to the interested reader (Kohlgrüber 2020).

2.5.2 Key Characteristics in Extrusion

Materials are subjected to a complex interdependence of effects during TSE compounding. For this work, an overview of key characteristics suffices.

Throughput ratio $\dot{V}^*$ and $\dot{Q}^*$

The dimensionless throughput ratio $\dot{V}^*$ of machine throughput by volume $\dot{V}$ per revolution n_{TSE} is introduced as the most important TSE characteristic (Kohlgrüber 2016, p. 577). The ratio $\dot{V}^*$ is defined in the following equation.

$$\dot{V}^* = \frac{\dot{V}}{n_{\mathrm{TSE}} \cdot D^3} \tag{2.8}$$

Where $\dot{V}$ is the volume of the material and D represents the housing diameter of the TSE (Kohlgrüber 2016, p. 371). $\dot{V}^*$ is closely related to the conveying parameter A_1 quantifying conveying performance of single screw elements considering their geometry (Kohlgrüber 2016, p. 337). The ratio $\dot{V}^*$ is constant over the entirety of the TSE, independent of machine size and can be used to scale extrusion processes (Kohlgrüber 2016, p. 338). $\dot{V}^*$ is dependent on several process parameters making it difficult to manipulate in a controlled fashion and complex to understand. Lower $\dot{V}^*$ will improve dispersion. Shear rates $\dot{\gamma}$ are proportional to n_{TSE} and higher shear conditions will increase fiber-polymer interactions. Residence times are inversely proportional to $\dot{V}$, so "work"

[3] Gleichlauf (co-rotating) Förderelement (conveying element) Auskämmend (self-cleaning)
[4] Gleichlauf Förderelement Mischend (mixing)

done on fibers decreases with increased throughput. Consequentially, increasing n_{TSE} relative to $\dot{V}$, one way or the other, will improve absolute shear stresses and the kneading frequency. (Hirata et al. 2013, p. 372)

Hirata et al. introduce a simplified ratio $\dot{Q}^*$ comprising total throughput $\dot{Q}$ in kg/h and n_{TSE} in min^{-1} (Hirata et al. 2013). For this work $\dot{Q}$ is equivalent to $m_{LFT\text{-}D}$.

$$\dot{Q}^* = \frac{m_{LFT-D}}{n_{TSE}} \tag{2.9}$$

Specific mechanical energy

Specific mechanical energy (*SME*) input is called the most important process characteristic, and a measure of the intensive work done to the material. It is machine independent and specific to material combinations. Energy flow through the TSE housing is not easy to measure, but also negligible next to the shear energy from n_{TSE}. *SME* is the common value used in literature. It is defined as

$$SME = \frac{2 \cdot \pi \cdot n_{TSE} \cdot M_{TSE}}{m_{LFT-D}} \tag{2.10}$$

With screw speed n_{TSE}, torque at screw M_{TSE} and $m_{LFT\text{-}D}$ as throughput (Kohlgrüber 2016, p. 67). Note, that the definition is neither specific to TSE nor LFT-D. Use of LFT-D specific parameters here and throughout this work serves clarity without significantly increasing the abbreviations introduced.

Inceoglu et al. proposed *SME* as a measure for fiber attrition as many relevant parameters are implied in it (Inceoglu et al. 2011, p. 1849). The direct relationship between n_{TSE} and the shear stresses needed to properly disperse fiber bundles was also noted (Stratiychuk-Dear et al. 2017, 150002-1).

2.5.3 Process Parameter Interactions

Fiber mass fraction of the resulting LFT-D product depends, based on equation (2.1) (p. 4), on the mass flow of both constituents. While polymer throughput is set at TSE1, fiber throughput from continuous rovings is dependent on more than one parameter (Truckenmüller and Fritz 1991, p. 1317). The following equation (2.11) calculates total fiber throughput m_f in kg/h from the amount of rovings n_{rov} in pcs., linear fiber density Tt in tex (g/km), screw speed of the mixing extruder n_{TSE2} in rpm and the fiber intake factor v_{intake} in m/rpm (Schelleis et al. 2023c, p. 2044).

$$m_f = n_{rov} \cdot Tt \cdot n_{TSE2} \cdot v_{intake} \tag{2.11}$$

The fiber intake factor v_{intake} has to be determined for all material combinations and processing parameters individually to account for fiber slippage (Tröster 2004, p. 57). Fiber fraction is always dependent on a combination of processing parameters m_p, n_{TSE2} and n_{rov} and cannot be set independently from these factors. Figure 2.5 depicts a parameter space defined by n_{TSE2}, fiber properties and n_{rov} while m_p is constant at 30 kg/h. Curves of constant w_f span the n_{rov} and n_{TSE2} space. Choosing a process parameter combination on these curves result in the same total LFT-D throughput m_{LFT-D}. (Schelleis et al. 2023c, p. 2047)

LFT-D is a continuous process with constant material output while compression molding is sequenced by the molding step. Material will exit TSE2 at constant throughput m_{LFT-D}. Considering die dimensions, material densities and w_f the speed of the chain belt is calculated and set by the LFT-D line to match the exit speed of LFT-D material. If those speeds do not match, the plastificate is stretched or staunched on the chain belt. Once enough material is extruded, shears cut the material to size (Tröster 2004, p. 44). This size is set by the operator, the goal is to fill the tool to specified part thickness.

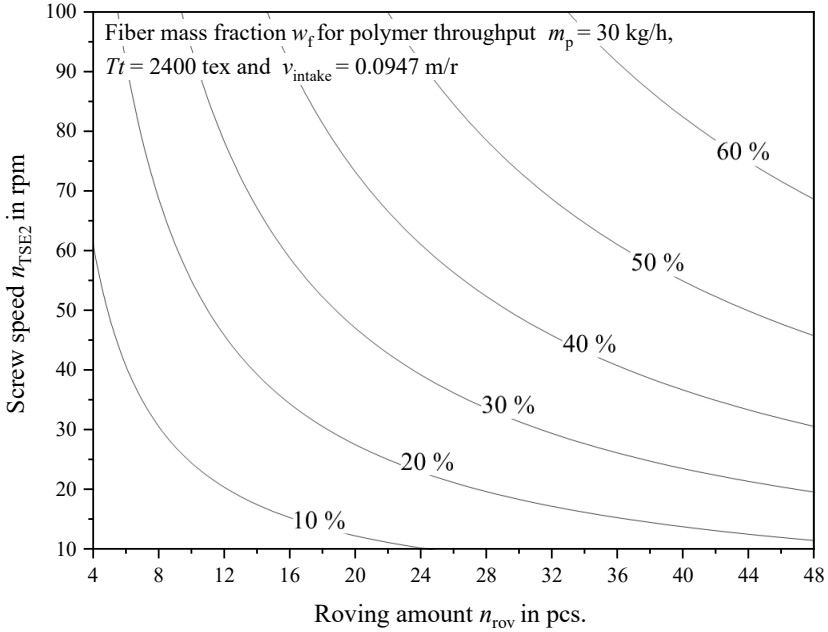

Figure 2.5 Parameter space of screw speed and roving amount resulting in w_f for a constant polymer throughput m_p = 30 kg/h. Adapted from (Schelleis et al. 2023c, p. 6).

2.5.4 LFT-D Semi-Finished Material – the Plastificate

At the die of TSE2, the end of the core LFT-D process, a mass of LFT-D is generated. After being cut, this semi-finished material has a plethora of names. It is called “extruded log”[5], “strand”[6], “extrudate”[7], “initial charge” or “charge”[8]. In this work it shall be named plastificate as in some of the original

[5] McLeod et al. 2010, p. 112.

[6] Henning et al. 2005, p. 26; Perez et al. 2013, p. 1115; Buck et al. 2015, p. 167; Priebe and Schledjewski 2011, p. 375; Fliegener 2015, p. 20.

[7] Knutsson et al. 1981, p. 2360; Truckenmüller and Fritz 1991, pp. 1320–1321.

[8] Gandhi et al. 2020, p. 376; Perez et al. 2013; Song et al. 2017, p. 244; Bondy et al. 2017, p. 195; Buck et al. 2015, p. 167; Osswald and Menges 2012, p. 241.

works on the topic (Henning 2001, p. 9; Bondy et al. 2017, p. 195; Rohan et al. 2014, p. 3; Tröster 2004, p. 22; Radtke 2009, p. 8).

Plastificate geometry and microstructure influence part quality as initial placement in the mold will influence material flow and mold filling which has substantial implications on the resulting microstructure (Tröster 2004, p. 49; Song et al. 2017, p. 253; Schreyer et al. 2022, p. 685). Height and especially width are dictated by the TSE2 die used. Length and height are adjusted to provide sufficient material to fill the mold geometry to specified part thickness. Length is constrained by mold dimensions, under processing considerations a certain distance to the mold edges is also added. (Henning et al. 2005, p. 27)

Lofting, also called “swelling” (Knutsson et al. 1981, p. 2360) or “foaming” (Truckenmüller and Fritz 1991, pp. 1320–1321), describes plastificate deviation from its ideal form by increasing its volume. The plastificate is not a perfect mixture of polymer and fiber but also contains “considerable amounts of air” (Bondy et al. 2017, p. 189). Lofting was observed to be stronger with increasing w_f (Rohan et al. 2014, p. 11). Stiff fibers will resist the shape given by soft polymer material and relax once the constraints of the die are gone (Radtke 2009, p. 62; Truckenmüller and Fritz 1991, pp. 1320–1321).

Measuring material temperatures (surface as well as inside) is reportedly difficult as the surface is jagged, and air will insulate probes. Evaluation of thermal imaging revealed a temperature difference of 10 K to 30 K from front to back for a PP GF30 LFT-D. (Radtke 2009, p. 62)

2.5.5 Initial Microstructure of the Plastificate

Knowledge of the initial fiber orientation is vital for all development tasks and especially attempting to simulate mold filling of LFT materials in compression molding (Gandhi et al. 2020, p. 273). Mapped fiber orientations of the plastificate improve models predicting fiber orientations in finished products (Song et al. 2017, p. 253)).

Brast reported a helical pre-orientation in the material for a single screw extruder depending on the chosen screw geometry (Brast 2001, p. 48). In twin screw extrusion two such helical shapes are found (Perez et al. 2013, p. 1120). Studying the macro- and microstructures of fiber bundles and single filaments, Perez et al. found good agreement in orientation for both (Perez et al. 2013, p. 1121).

Tröster found via radiography, that the preorientation of macrostructures in a PP GF plastificate amounted to ± 60° in relation to the extrusion direction (0°) with a deviation between measurements of 2 % - 7 % (Tröster 2004, p. 50). A fishbone shaped pattern was suggested for macroscopic fiber orientation in the plastificate (Tröster 2004, p. 51). Radtke, scanning five layers of a PP plastificate suggested, that fibers in the mantle area of the plastificate are oriented in extrusion direction while fibers in the middle are oriented increasingly perpendicular to this direction (Radtke 2009, p. 76).

2.6 Microstructure Development during Molding of FRPs

Having established how important fiber morphology is for FRPs and how compounding influences it, we will now examine how these key factors (FOD, FLD and w_f) change during the compression molding step. Figure 2.6 expands upon the processing scheme in Figure 2.4 (p. 16) highlighting the situation in the mold.

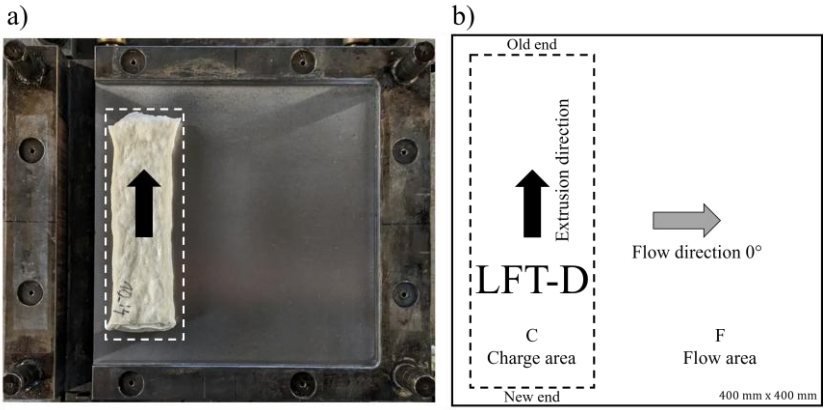

Figure 2.6 Compression molding scheme for an LFT-D plastificate. Position of the plastificate directly before press closure a). Schematic explanation of relevant terms, extrusion and flow direction, charge, and flow area as well as old and new end b).

The important element is the plastificate charge area of the mold surface before molding. It is indicated by a dashed line around the plastificate on the left and repeated schematically on the right. From here the plastificate will flow towards all edges of the mold during compression molding. The main flow direction is indicated by a light grey arrow (Figure 2.6, b)). The area occupied during molding is called the flow area. Extrusion direction from TSE2 is continued in the plastificate (Figure 2.6, black arrow). Sequenced molding after continuous extrusion results in an age gradient along the direction of extrusion

in the plastificate (Radtke 2009, p. 61). The ends are called old and new (Figure 2.6, b)) in reference to them exiting TSE2 first or last (Schelleis et al. 2023b, p. 3).

During mold filling, the FRP melt is subjected to two patterns, shear and radial flow, shown in Figure 2.7. Shear flow (Figure 2.7 a)) can be seen as one-dimensional mass flow with a flow-front of constant width. Radial flow (Figure 2.7 b)) can be seen as a two-dimensional mechanism where the width of the flow-front changes with flow progression and orientation effects perpendicular to flow direction are found. In reality, a superposition of both patterns exists. (Eyerer et al. 2008, p. 219)

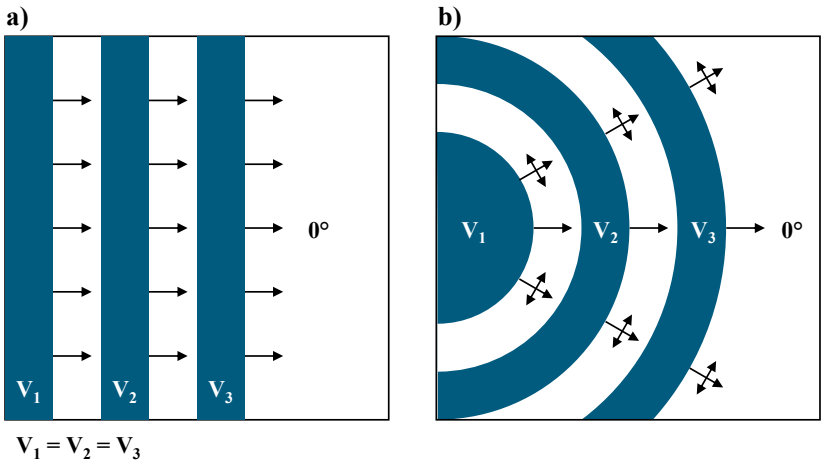

Figure 2.7 Schematic depiction of shear flow a) and radial flow b). Adapted from (Eyerer et al. 2008, p. 219)

As the flow-front progresses thermoplastic material freezes to the cold mold walls (no-slip condition) and a fountain flow effect can be observed, adding to shear and radial flow (Tadmor 1974, p. 1756). During mold filling the material velocity $\boldsymbol{v}_m$ is highest around the mid plane of the part thickness while shear

rate $\dot{\gamma}$ is lowest here as well as at the mold wall where $\boldsymbol{v}_m$ and $\dot{\gamma}$ are zero. (Gandhi et al. 2020, p. 75)

2.6.1 In-Mold Fiber (Re-) Orientation and Migration

The first stage in LFT-D compression molding starts with an open mold. The material is placed in the mold before closing, which results in two very distinct part areas. Upon contact with the relatively cold mold surface, the fiber orientation of the plastificate mantle is frozen in place in the charge area. Once the press transmits force onto the FRP, the material is pressed out of its original position into the flow area (Osswald and Menges 2012, p. 240) (cf. terminologies in Figure 2.6 (p. 23)).

Assuming planar flow, two main rules of fiber orientation in suspensions can be formulated from Jefferey's equation (Jeffery 1922). Rigid fibers will align in flow direction for shearing flows and across radial direction for radial flows (Tucker 2022, p. 93 ff.). The flow direction is defined as 0° direction (cf. Figure 2.7 (p. 24)).

From injection molding the existence of a shell-core structure is known. Here, fiber orientation in the middle of the geometry is different from the border areas (Truckenmüller and Fritz 1991, p. 1324).

In LFT-D compression molding a shell layer is only formed in the charge area (Figure 2.6, r. (p. 23)) where an initial orientation in the extrusion direction is frozen upon mold contact (Osswald 20.05.2014, p. 18). Similar morphology was found for PC LFT-D parts analyzed via micrographic analysis (Schelleis et al. 2023c, p. 2054).

In Figure 2.8 a micrograph depicting a slice across the entire thickness of the plate in the charge area on the left a) and the flow area on the right b) is shown. Based upon analysis of the fiber orientation (cf. 2.3.1 (p.11) analyzing cut surface ellipses) shell and core are marked in the charge area a) while the flow area b) exhibits a uniform FOD. Flow orientation is noted in the center of

Figure 2.8. Fibers are generally aligned in flow direction with process induced deviations explained in further sections.

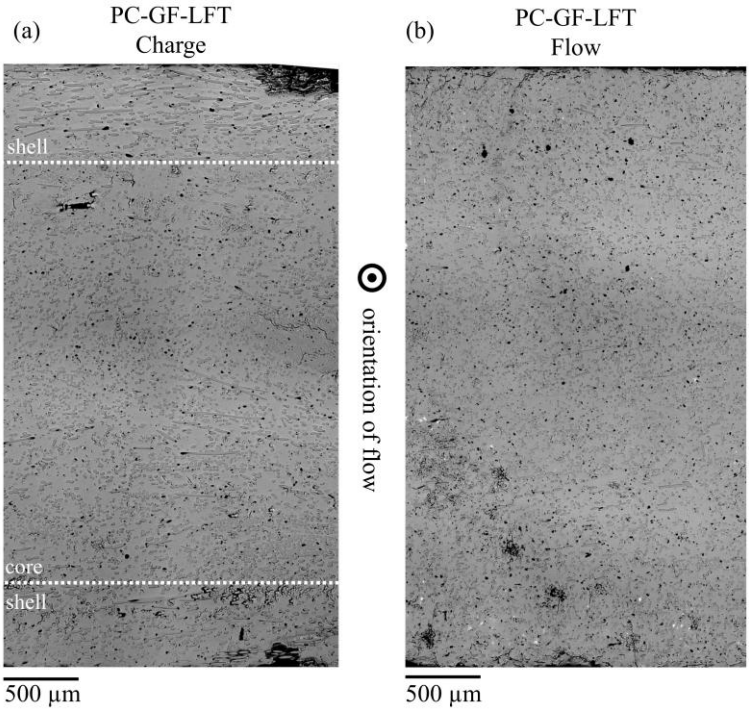

Figure 2.8 Micrograph over the entire thickness (h = 3 mm) of a compression molded PC GF LFT-D plate. The charge area with distinct shell and core area a). The flow area shows a uniform fiber orientation b). (Schelleis et al. 2023c, p. 13)

2.6.2 Fiber Migration – Location Dependent Fiber Fraction Change

In Jeffery's equation we assume that fibers are transported with their surrounding fluid (Jeffery 1922). This is true for dilute suspensions where the distance between fibers is greater than l_f (Folgar and Tucker 1984, p. 99). LFT materials

in commercial use are categorized as highly concentrated, where the distance between fibers corresponds to fiber diameter (Rohde-Tibitanzl 2015, p. 7). A "global fiber concentration gradient" (Gandhi et al. 2020, p. 106) along the flow path of the material is present for most compression molded material systems reported in varying degrees.

Goris and Osswald conducted a global w_f gradient analysis for injection molded PP GF05-60, where entire plates were pyrolyzed and characterized. For $w_f = 10$ % to $w_f = 60$ % the fiber fraction concentrates towards the very end of the flow path. Fiber fraction at the gate is 5 % below and at the end 11 % above nominal w_f. (Goris and Osswald 2018, p. 328)

For LFT injection molding not only fiber migration over the flow path is reported but also in the thickness direction of the plate. In the same study Goris and Osswald characterized the through-thickness fiber concentration via µCT. For all non-dilute suspensions, the core layer was found to contain significantly more fiber than the shell layers (peaking at 1.5 times nominal w_f for PP GF40). (Goris and Osswald 2018, p. 328)

These data indicate that fiber migration is sensitive to local shear flow. Shear-induced migration pushes fibers into areas of lower shear rate, found along the center line of the material. The material velocity in this midplane is higher than in surrounding areas and the fibers are moved to the flow-front (Mavridis et al. 1992). Fibers at the flow-front are distributed across the entire gap height before rolling onto the mold wall and freezing. At the end of the flow part towards the mold wall this redistribution ends and fiber fraction peaks. (Tucker 2022, p. 262 ff.)

Fiber migration is not yet fully understood and suspected to be very complex as all factors (w_f, FOD, FLD, η) involved influence each other (Tucker 2022, p. 268; Laun 1984; Huq and Azaiez 2005; Tozzi et al. 2013).

2.6.3 Fiber Length Changes along the Flow Path

As discussed, l_f decreases over processing length being subjected to various degradation mechanisms (cf. chapter 2.4 (p. 13)). Stresses during molding act the same way as in compounding for fiber breakage (Bechara et al. 2021, 073318-1). In some cases, however, an increase in measured l_w towards the end of the flow path is observed for both injection (22 % increase in l_w) (Goris and Osswald 2018) and compression molding (38 % increase in l_w) (Osswald 20.05.2014). Especially longer fibers are directed towards the areas of higher velocity and then transported towards the flow-front resulting in an FLD skewed towards the longer l_f.

2.7 Comprehensive Overview of LFT-D/ ILC Process and Material Development

Discussed towards the end of this section are trials and publications working with the Dieffenbacher LFT-D ILC machine scheme found at Fraunhofer ICT, Pfinztal, Germany and Fraunhofer Innovation Platform for Composites Research at Western University (FIP-Composites@Western), London, Ontario (cf. Figure 2.4 (p. 16) for the process scheme). Leading up to this, a general overview of reported process-microstructure relations is given as literature is sparse for LFT-D alone.

2.7.1 Choice and Influence of Processing Parameters

The desired quality of LFT-D products hinges on a favorable microstructure defined during compounding and molding by choice of processing parameters (Gandhi et al. 2020, p. 101). From the state of the art review, screw speed, throughput, barrel zone temperatures as well as screw design were identified as the most important parameters to optimize for processing (Kohlgrüber 2016, pp. 683–684).

In the following tables, every parameter mentioned is put in global context to the other parameters as well as general extrusion characteristics (cf. 2.5.2 (p. 17)) first. General, as in cross-process route, effects on fiber properties are listed and deepened with reported LFT-D findings where available. The findings are summarized and presented in tabular form for ease of use and reference inspired by Rohde-Tibitanzl (Rohde-Tibitanzl 2015, pp. 19–22). A short conclusion on the influence of each parameter is made.

Screw speed

Screw speed is a central factor in twin-screw extrusion. As a general recommendation, FRP shall be processed at low screw speed n_{TSE} (Kohlgrüber 2016, p. 72). This was considered for early LFT-D process development to improve dispersion and l_f retention (Tröster 2004, p. 57). In discussions with technical

personnel, both internally as well as externally at industry partners, the consensus is to run the machine at lowest n_{TSE}.

As Table 2.1 demonstrates, n_{TSE} is involved in many factors, especially shear conditions, that are in turn relevant to microstructure. Good dispersion of fiber bundles, which is better at higher shear stresses (Kohlgrüber 2016, p. 470), is key for good mechanical properties (cf. Figure 2.2 (p. 7)). Fiber lengths are generally higher for lower n_{TSE}: however, this can be mitigated by increasing throughput as well. Both n_{TSE} and $m_{LFT\text{-}D}$ influence the residence time t_{res} of the material in the TSE. A general statement about an ideal setting cannot be formulated from the literature considered.

This discrepancy between established procedure “in the field” and theoretical background will be central to this work and subject of the research hypothesis in chapter 2.9 (p. 46).

Table 2.1 Influence of processing parameters: screw speed n_{TSE}. Sorted global to specific effects from general twin-screw extrusion to LFT-D compression molding.

n_{TSE} ($\wedge\vee$)	Effect on ($\wedge\vee$)	Summarizing statement	Source (*LFT-D)
Global influences of screw speed, n_{TSE}			
$\wedge$	m_f $\wedge$	Fiber intake is regulated by screw speed.	i.a. (Priebe and Schledjewski 2011, p. 375)
$\wedge$	Dispersion $\wedge$	Dispersive mixing effects are correlated to n_{TSE}.	(Kohlgrüber 2016, p. 60)
$\wedge$	t_{res} $\vee$	Residence time t_{res} decreases with increased n_{TSE}. Distribution of t_{res} stays the same.	(Gogoi and Yam 1994, p. 178)
$\wedge$ $\vee$	$t_{res,mean}$ $\wedge$ $\vee$	In partially filled screw segments t_{res} is dependent on n_{TSE} and $m_{LFT\text{-}D}$.	(Kohlgrüber 2016, p. 69)

n_{TSE} (∧∨)	Effect on (∧∨)	Summarizing statement	Source (*LFT-D)
∧	T ∧	Viscous heating is proportional to the square of the shear rate.	(Hirata et al. 2013, p. 372)
∧	SME ∧	Proportional to energy input.	i.a. (Maertens et al. 2021, p. 139)
∧	τ ∧	Shear rate increases. Stress on fiber increases, but η drops.	(Inceoglu et al. 2011, p. 1846)
∧	T ∧	T increase higher for higher w_f.	*(Rohan et al. 2014, p. 10)
Influence of screw speed, n_{TSE}, on fiber length l_f (l_n, l_w)			
∨	l_f ∧	Reduced shear stresses decrease fiber breakage. Optimization problem as dispersion suffers.	(Kohlgrüber 2016, p. 74)
∧	l_f >	When increasing throughput simultaneously.	(Kohlgrüber 2016, p. 597)
∧	l_f ∨	l_f decreased and FLD narrowed.	(Inceoglu et al. 2011, p. 1842)
∧	l_n, l_w ∨	Overall fiber lengths decrease.	(Inceoglu et al. 2011, p. 1846)
∧	l_f ∨	High n_{TSE}, high fiber damage.	(Priebe and Schledjewski 2011, p. 379)
∧	l_n ∨	Shear stress via n_{TSE} has the biggest influence on fiber fracture. With the total number of revolutions being the most significant, albeit not proportional, factor.	(Hirata et al. 2013, p. 374; Inceoglu et al. 2011, p. 1843)
∧	l_n ∧ >	Tendency, only insignificant though, for increased l_n at higher screw speeds.	*(Schelleis et al. 2023c, p. 2052)
Influence of screw speed, n_{TSE2}, on mechanical properties			

n_{TSE} (∧∨)	Effect on (∧∨)	Summarizing statement	Source (*LFT-D)
∧	E, σ ∧	Average flexural properties better. Suspected reduction in bundles	*(Rohan et al. 2014, p. 16)
∧	E, σ ∧	Slightly, not significant, higher tensile properties.	*(Dahl et al. 2012, p. 12)
∧ ∨	E, σ >	Mixed results for n_{TSE} increase. No effect found.	*(Schelleis et al. 2023a, p. 10)
∧	E, σ ∧	Increased tensile properties for increased n_{TSE} in four steps.	*(Schelleis et al. 2023b, p. 6)

Screw configuration

Choosing the right screw configuration is a challenging task. To discretize screw configurations, the differentiation between low and high shear configurations, characterized by screw elements chosen, is made. Kneading blocks (Kohlgrüber 2016, p. 131) as well as GFM mixing elements are high shear elements (Kohlgrüber 2016, p. 150). In Table 2.2, screw design variations reported in the literature are summarized as increasing or decreasing “shear”, meaning the overall shear stress the material is subjected to. The GFM used in the LFT-D sources (marked by *) are exclusively hedgehog elements.

Table 2.2 Influence of processing parameters: screw design. Sorted global to specific effects from general twin-screw extrusion to LFT-D compression molding.

Shear (∧∨)	Effect on (∧∨)	Summarizing statement	Source (*LFT-D)
Influence of screw design (high/low shear) on l_f (l_n, l_w) and a_r			
∧	l_f ∨	Even conveying elements can cause severe attrition to the fiber.	(Priebe and Schledjewski 2011, p. 379)

Shear (∧∨)	Effect on (∧∨)	Summarizing statement	Source (*LFT-D)
∧ +	a_r ∧	More chaotic flow instead of just high shear screws will improve de-bundling.	(Hirata et al. 2013, p. 369; Kuroda and Scott 2002, p. 405)
∧ ∨	l_f >	Little effect on l_f.	(Hirata et al. 2013, p. 375)
∧	l_n ∨	At high $\dot{V}^*$, l_n reduces	* (Hümbert 2016, p. 51)
∧	FLD ∧	GFM increases shear effects and widens FLD	*(Tröster 2004, p. 55)
∧	l_n ∨	Added GFM almost halve l_n	
Influence of screw design on mechanical properties			
∧	E, σ ∧	More GFM, higher average tensile properties.	*(Hümbert 2016, p. 56)
∨	σ ∨	Low mean tensile strength due to insufficient de-bundling and poor wetting.	*(Dahl et al. 2012, p. 7)
∧ ∨	E, σ >	For highly viscous PC LFT-D the presence of a GFM does not influence mechanical properties.	*(Schelleis et al. 2023a, p. 10)

It was noted that a certain amount (one, in most sources) of GFM was needed to de-bundle fiber rovings in LFT-D processing for PP as well as PA6. This is not the case for PC GF LFT-D where shear forces in the extruder are high enough by the matrix alone. Generally, a low shear setup will increase fiber length, however the mechanical properties suffer in the suspected presence of fiber bundles.

Total throughput

While total throughput $m_{LFT\text{-}D}$ in industrial application is dictated by the part to be manufactured and available machinery, it is a factor in process development. Investigating literature regarding $m_{LFT\text{-}D}$, it becomes clear that only parameter combinations are key to process optimization as $m_{LFT\text{-}D}$ does not ever stand alone as the primary factor. Its alteration in relation to *SME* or $\dot{V}^*$ is identified as influence on fiber length, dispersion, and mechanical performance.

Table 2.3 Influence of processing parameters: material throughput $m_{LFT\text{-}D}$. Sorted global to specific effects from general twin-screw extrusion to LFT-D compression molding.

$m_{LFT\text{-}D}$ (∧∨)	Effect on (∧∨)	Summarizing statement	Source
Global influences of throughput, $m_{LFT\text{-}D}$			
∧ ∨	$t_{res,mean}$ ∧ ∨	In filled screw segments residence time depends on $m_{LFT\text{-}D}$.	(Kohlgrüber 2016, p. 69)
∧ ∨	$t_{res,mean}$ ∧ ∨	In partially filled screw segments residence time is dependent on n_{TSE} and $m_{LFT\text{-}D}$.	(Kohlgrüber 2016, p. 69)
∧	~t_{res} ∨	Distribution of t_{res} tightens for higher $m_{LFT\text{-}D}$.	(Gogoi and Yam 1994, p. 178)
∨	Dispersion ∧	Better mixing quality.	(Kohlgrüber 2016, p. 60)
Influence of throughput, $m_{LFT\text{-}D}$, on fiber length l_f (l_n, l_w)			
∧	l_w ∧	Probability of finding longer fibers increased. Stronger effect than n_{TSE}.	(Inceoglu et al. 2011, p. 1846; Ville et al. 2013, p. 52)

m_{LFT-D} (∧∨)	Effect on (∧∨)	Summarizing statement	Source
∧	l_f ∧	Relating to degree of fill, the probability of fiber damage is lower for higher throughputs.	(Kohlgrüber 2016, p. 74)
∧	l_n ∧	Lower t_{res} leads to less fiber attrition and higher mean l_n.	(Kloke et al. 2011, p. 68)
Influence of throughput, m_{LFT-D}, on mechanical properties			
∧	E, σ >	Increasing m_{LFT-D} allows for higher n_{TSE}.	(Kohlgrüber 2016, p. 597)

Amount of fiber rovings

Exclusively relevant to processes dealing with continuous fiber intake the number of fiber rovings n_{rov} (in pieces) together with n_{TSE} dictate m_f (cf. Equation (2.11) (p. 19)). Despite being a primary factor in direct fiber processing, n_{rov} is usually set after m_{LFT-D} and n_{TSE} to match desired w_f (i.a. (Tröster 2004, p. 57; Priebe and Schledjewski 2011, p. 378)).

Working with direct fiber feed in injection molding, higher fractions of l_w were reported for higher n_{rov} (Rohde-Tibitanzl 2015, p. 103). Lower w_f deviations were noticed for higher n_{rov} (Truckenmüller 1996, p. 90).

Processing temperatures

Experiments conducted in LFT-D process development have not reported investigating TSE temperatures. Material temperature in extrusion is significantly influenced by shear forces induced via n_{TSE} and not the machine barrel (Frankland 2019). While increased fiber attrition can be attributed to increased n_{TSE}, simultaneous increase in processing temperature and change in shear stress, higher temperature - lower η, can decrease fiber attrition (Bumm et al. 2012, p. 2147).

Key characteristic: throughput ratio $\dot{Q}^*$

The complexity of $\dot{Q}^*$ was outlined in 2.5.2 (p. 17). It is rarely the subject of active investigation and thus the results available, collected in Table 2.4, are contradictory.

Table 2.4 Influence of key characteristics: throughput ratio $\dot{Q}^*$. Sorted from global to specific effects from general twin-screw extrusion to LFT-D compression molding.

$\dot{Q}^*$ (∧∨)	Effect on (∧∨)	Summarizing statement	Source (*LFT-D)
Global influences of throughput ratio, $\dot{Q}^*$			
∧	Dispersion ∨	Less dispersion for higher $\dot{Q}^*$.	(Kohlgrüber 2016, p. 74)
Influence of throughput ratio, $\dot{Q}^*$, on fiber length l_f (l_n, l_w)			
∧	l_w ∧	Probability of finding longer fibers increased.	(Inceoglu et al. 2011, p. 1846)
∧	l_f ∧	Less attrition for higher $\dot{Q}^*$.	(Kohlgrüber 2016, p. 74)
∨	l_f ∨	Decreasing $\dot{Q}^*$ increases shear rate and promotes attrition	(Hirata et al. 2013, p. 374)

Further effects

Other observations are shared in publications: however, it is hard to form a coherent picture from so few statements. Noteworthy is the observation that fiber bundles are retaining l_f by supporting themselves against abrasion (fiber-fiber effects) (Rohde-Tibitanzl 2015, p. 95). Bundles exhibit much higher resistance to attrition by buckling (fiber-polymer effects) (Priebe and Schledjewski 2011, p. 377). At the point in the TSE where a bundle disperses, l_f is high. When bundles disperse is highly dependent on material combination and specific machine setup. This might explain divergent observations regarding the optimization problem dispersion and retention of l_f.

2.7.2 Resulting Microstructures

Fiber fraction

The general phenomenon of fiber migration for FRP was discussed in 2.6.2 (p. 26). Radtke reported maximum deviations in w_f of PP GF LFT-D of up to $w_f = 10$ %*pt*. (Radtke 2009, p. 18). Osswald reported a w_f gradient for PP GF LFT-D from charge position ($w_{f,charge} = 25.25$ %) towards the end of the flow path ($w_{f,flow} = 32.04$ %) with nominal $w_{f,nominal} = 30$ % (Osswald 20.05.2014, p. 37). Hümbert worked with PA6 GF and found that desired w_f was surpassed for high screw speeds but found no consistent correlation between flow length and w_f (Hümbert 2016, p. 52). Working with PA6 CF LFT-D, Rohan found w_f "relatively consistent" for all trial points from $w_f = 30$ % to 45 % (Rohan et al. 2014, p. 18). Not subject to w_f deviations are PC GF LFT-D materials (Schelleis et al. 2023b, p. 5). However, w_f was underestimated by equation (2.11) (p. 19) and proper characterization of v_{intake} was recommended (Schelleis et al. 2023c, p. 2051).

No clear picture can be formulated. However, it seems that fiber types interact differently depending on polymer-fiber combination and resulting fiber morphology.

Fiber length

With remarks on the challenges of l_f measurements in mind (cf. 2.2.2 (p. 8)), Table 2.5 summarizes reported l_n and l_w from LFT-D developments. The table is sorted by material system and then by w_f. Universal tendencies can be seen as l_n decreases for more viscous polymers as well as for growing w_f (Kohlgrüber 2016, p. 74). Microscopy methods with smaller sample sizes lead to higher l_n for PP, but not for PA6. Minimum l_f are found where shear stresses necessary to further break fibers are rising exponentially and thus are not present in processing (Hirata et al. 2013, p. 375). This is the case for PC GF LFT-D where no parameter variation could significantly change l_f (Schelleis et al. 2023a, p. 6).

Table 2.5 Reported l_n and l_w from LFT-D development campaigns. Sorted by material system and fiber fraction w_f. Characterization method and source are given.

Material system	w_f in %	l_n in mm	l_w in mm	Method	Source (all LFT-D)
PP GF	10 - 60	20	-	Microscopy	(Tröster 2004, p. 55)
PP GF	25	11	-	FASEP	(Buck et al. 2015, p. 162)
PP GF	30	3[9]	-	FIBASTAT	(Radtke 2009, p. 55)
PP GF	30	1.2	15	FASEP	(Fliegener 2015, p. 79)
PP GF	40	7	30	Microscopy	(McLeod et al. 2010, p. 117)
PA6 GF	30	1.5	5-10	Microscopy	(Hümbert 2016, pp. 47–50)
PA6 GF	42	1.2	4.9	FiberShape	(Scheuring et al. 2024, p. 8)
PA6 CF	9 - 25	0.3	-	Microscopy	(Bondy et al. 2017, p. 191)
PA6 CF	30 - 45	0.3[10]	-	(Dahl et al. 2011)	(Rohan et al. 2014, p. 19)
PA6 CF	33	6.4	1.6	FiberShape	(Scheuring et al. 2024, p. 8)
PA6 CF	34	4.4	-	FASEP	(Christ et al. 2023, p. 2)
PC GF	20	0.8	-	FASEP	(Schelleis et al. 2023a, p. 6)
PC GF	40	0.5	1.4	FASEP	(Schelleis et al. 2023c, p. 2052)

[9] Radtke worked with cut fibers with a starting length of 25 mm.
[10] Rohan et al. separated fibers over 2 mm before measuring.

Fiber orientation

The general behavior was discussed in 2.6.1 (p. 25) and existence of charge and flow area as well as shell and core phenomena established.

Flow induced fiber orientation in the LFT-D flow area (cf. Figure 2.6 (p. 23)) is expected to match the main 0° flow direction (Folgar and Tucker 1984). However, throughout LFT-D development, systematic deviations were noticed. Bondy et al., sampling in ±45° direction, noticed that stiffnesses were higher in +45° than in –45° direction. They hypothesized that fiber orientation asymmetries in the plastificate (Bondy et al. 2017, p. 191) might be accountable and associated these asymmetries to TSE2 screw pitch (Bondy et al. 2017, p. 181).

Characterizing anisotropy in the flow area, Radtke found similar behavior and could also explained plate warpage (Radtke 2009, p. 63). Radtke described temperature differences from old to new plastificate ends to be influential (Radtke 2009, p. 40). The assumption that the main fiber orientation φ_v coincides with flow direction cannot be made (Tröster 2004, pp. 82–83). Turning the plastificate 180° around its yaw axis reversed FO deviation in plates, corroborating Bondy's as well as Radtke's claims that the plastificate is indeed at the center of the phenomenon (Tröster 2004, p. 87).

The anisotropy ratio was found to be highest (more fibers oriented in the main direction) in the middle of plates between charge and flow area (Radtke 2009, p. 45) and to be generally increasing for higher w_f (Tröster 2004, p. 88). Fiber orientation in the flow area was found to be consistent across plate thicknesses for various material systems and w_f (Radtke 2009, p. 53).

2.7.3 Mechanical Properties from LFT-D Material Development

Table 2.6 summarizes quasi static tensile properties of LFT-D materials sampled in the flow area in 0° flow direction, however, this description might vary a lot as sampling schemes are not always reported. In a few sources the conditioning state of the material is given. Considering reported microstructure

development and fiber migration the nominally given w_f is to be viewed with caution. Deviations from $w_{f,nominal}$ to w_f at the actual sample location must be expected.

Various characterization methods are reported, with different testing velocities and sample geometries. Overall, a reliable comparison is difficult and Table 2.6 shall be seen as an overview of tensile properties of LFT-D materials. A wide spectrum of mechanical properties is covered by LFT-D DiCo materials. Deviation of properties is in the single digit percentage area but can present a considerable spread typical for LFT materials in general (Schemme 2008, p. 33).

Table 2.6 Tensile properties from LFT-D development. Sorted by material system, fiber fraction and characterization method. Values were rounded to one decimal where applicable. The variances were recalculated where given (noted by r). Data taken out of a plot is noted by p.

Material system	w_f in %	E in GPa	σ in MPa	Method, conditioning	Source
PP GF	10	3	-	EN ISO 527-4	(Tröster 2004, p. 79)
	20	4.8	-		
	30	6.2	-		
	40	7.3	-		
	50	10	116		
	60	10.3	116		
PP GF	20	4.4 (2.5 %^{r})^p	-	DIN EN ISO 3167	(Fliegener 2015, p. 97)
	30	6.6 (8.2 %^{r})^p	~100^p		(Fliegener 2015, p. 97;117)

Material system	w_f in %	E in GPa	σ in MPa	Method, conditioning	Source
PP GF	30	7.8	-	DIN EN ISO 3167	(Garesci and Fliegener 2013, p. 143)
PP GF	30	-	60	DIN EN ISO 527-4	(Krause et al. 2003, p. 295)
PP GF	40	7.6[p]	-	DIN 527	(Geiger et al. 2006, p. 33)
ABS GF	30	7.3[p]	-		
ABS GF	30	-	78	DIN 527	(Krause et al. 2003, p. 295)
PET GF	30	-	126		
SAN GF	30	9.7[p]	-		(Geiger et al. 2006, p. 33)
PA6 GF	30	5.5 (7.5 %[r])[p]	108.3 (4.5 %[r])[p]	ASTM D638 V, conditioned (20 °C, 28 % *RH*)	(Mohammadkhani et al. 2023, p. 6)
	30	7.2 (6.4 %[r])[p]	154.1 (8.5 %[r])[p]	ASTM D638 V, dry as molded	
PA6 GF	30	9.7 (4.6 %[r])[p]	172.5 (4.5 %[r])[p]	ISO 527-4	(Hümbert 2016, 56 - 58)
PA6 GF	30	-	112	DIN EN ISO 527-4	(Krause et al. 2003, p. 295)
PA6 GF	30	7.1	151.3	ASTM D638 V, dried	(Khapra et al. 2025, p. 12)
PA6 GF	45	11.3	175.3		
PA6 CF	9	8.2 (3.9 %)	134[p]	ASTM D638, conditioned	(Bondy et al. 2017)

Material system	w_f in %	E in GPa	σ in MPa	Method, conditioning	Source
PA6 CF	12	10.4 (3.8 %)	152^{p}	(25 °C, 30 % *RH*)	(Rohan et al. 2014, p. 15)
	18	14.5 (6 %)	190^{p}		
	25	20.8 (6.3 %)	241^{p}		
	30	15^{p} (49 %^{r})^{p}	173^{p} (31 %^{r})^{p}	ISO 527-4, as received/ room temperature	
	35	25.7^{p} (4.4 %^{r})^{p}	227^{p} (7 %^{r})^{p}		
	40	27.2^{p} (3 %^{r})^{p}	227^{p} (6.1 %^{r})^{p}		
PA66 CF	40	24.0 (8.5 %)	206.8 (6.5 %)	Based on ASTM, vacuum dried	(Bondy et al. 2022, p. 7678)
PA66 CF	40		255.2	Dried	(Khapra et al. 2025, p. 12)
PA66 CF	20	-	175	ISO 527, dry as molded	(Dahl et al. 2011)
PA66 CF	35	23.5	190.2	ASTM D3039M-17	(Smith et al. 2020, p. 20)
PA66 CF/ GF hybrid	35 (3:1 ratio)	24.4	198.7		
PC GF	40	10.8 (12 %^{r})^{p}	134.8 (11 %^{r})^{p}	DIN EN ISO 527-4, adapted sample geometry	(Meierhans 2022, p. 19 f)
PC GF	20	6.3 (7.4 %)	121 (4 %)	DIN EN ISO 527-4, adapted sample geometry	(Schelleis et al. 2023a, p. 8)
	40	10.8 (6.4 %)	130 (7 %)		

Plateaus of tensile properties can be seen across all material systems. Between $w_f = 35$ % and 40 % stiffness and strength have peaked for PA6 CF (Rohan et al. 2014, p. 15). For PP GF this plateau was detected between $w_f = 50$ % and 60 % (Tröster 2004, p. 79). The increase in tensile strength of PC GF from $w_f = 20$ % to 40 % is minimal, indicating the plateau in close proximity (Schelleis et al. 2023a, p. 8).

Figure 2.9 a) visualizes reported LFT-D stiffnesses (cf. Table 2.6). The density ρ was calculated for all composites according to their reported w_f (Osswald and Menges 2012, p. 95). Assumptions were made about matrix and fiber densities according to literature (Ashby 2017). Clearly, CF LFT-D stands out with exceptional stiffness at medium densities. For GF, an increase in E necessitates a higher increase in ρ making the FRP heavier at a faster rate than stiffer. Reported E for PA6 GF break out towards lower stiffness at medium to high ρ (green circles). Figure 2.9 b) depicts reported tensile strength σ over ρ in similar fashion as before. The high range of reported σ between 112 MPa and 172.5 MPa for PA6 GF30 becomes apparent (light green circles).

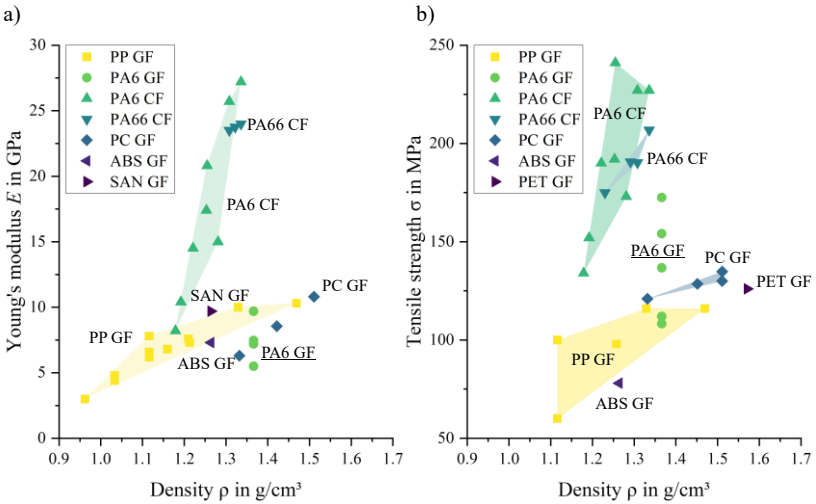

Figure 2.9 Plots of Young's modulus E a) and tensile strength σ b) from reported LFT-D trials over calculated composite density ρ.

2.8 Open Questions from the State of the Art

Various works concerning LFT-D were written over the last two decades with widely different goals and approaches. Materials were benchmarked focusing on PA6 and PA66 (cf. Table 2.6 (p. 40), half of reported studies). Here, PA6 was noticeably often paired with CF. The lack of studies into PA6 GF, a presumably more common combination in practice, was noticed (Mohammadkhani et al. 2023). No other than $w_f = 30$ % was found in PA6 GF reports to date. The uncertainty about a high range of reported properties, E and σ especially (cf. green circles in Figure 2.9), make those reports hard to utilize.

What are the mechanical properties of PA6 GF across the spectrum of practical use?

Especially in economically attractive direct processing of LFTs from raw materials, the producer is responsible for part quality facing compounding challenges like homogenization, consistency and performance (Schemme 2008, p. 38). Leading mechanisms for fiber attrition and roving dispersion are rooted in complex interactions (Rohde-Tibitanzl 2015, p. 22). Diving into reported insights regarding the process-microstructure relation has shown considerably contradictory statements (cf. tables in 2.7.1 (pp. 29)). No studies with independently varied factors were found. All studies aim for predetermined w_f and set one or more parameters, usually n_{rov}, to match according to equations (2.1) (p. 4) and (2.8) (p. 17). Studies available in literature thus lack methodological rigor regarding the choice of independent parameters and seem to suffer under resource constraints from material costs, material, and characterization efforts.

How do LFT-D parameters interact and influence mechanical properties? Can effects be isolated given closely linked factors?

The fiber microstructure is of importance to mechanical properties and thus for technical applications (cf. 2.1 (p. 3), 2.2 (p. 6) and 2.3 (p. 11)). From injection molding of LFT materials the phenomena of fiber-matrix migration (Gandhi et al. 2020, p. 106) as well as a shell-core effect (Willems et al. 2020, p. 3) are known. These phenomena lead to heterogeneity in the microstructure and are

partially related to, among others, shear forces during molding (Tucker 2022, p. 263).

Microstructure of compression molded LFT-D is similarly complex. However, processing principle and conditions differ from IM so findings can only serve as guidance. The fiber orientation difference between LFT-D charge and flow area is acknowledged in most works (i.e. (Bondy et al. 2019; Rohan et al. 2014)). Fiber-matrix separation was reported by several authors (cf. 2.7.2 (pp. 37)). Still, most results are presented relating to a nominal w_f (cf. Table 2.6 (p. 40)). Deviations of fiber orientations are recognized and attempts to explore the causes are found (cf. 2.7.2 (p. 37)). These deviations are not considered during mechanical characterization. A definite explanation cannot be found. Existing explanations, such as pre-orientation of fibers and temperature differences in the plastificate were found to be insufficient in exploration trials conducted for this work.

What parameter-related mechanisms influence microstructure development?

While the plastificate has received attention in some works (cf. 2.5.4 (p. 20) and 2.5.5 (p. 21)), there is a consistent call for a holistic investigation into the role of the link between compounding and compression molding. Importance of the plastificate regarding the final microstructure and fiber orientation is recognized (Rohan et al. 2014; Buck et al. 2015). No attempts to link plastificate properties to processing parameters were found.

What is the plastificates role regarding microstructure in molded parts?

How is the plastificate influenced by processing parameters?

2.9 Research Hypothesis, Questions and Approach

The state of the art was presented, analyzed, and open questions identified accordingly. One hypothesis is formulated regarding the core processing advice.

Hypothesis

During continuous extrusion of fiber-reinforced semi-finished products for direct processing in discontinuous compression molding, the choice of parameters of the mixing extruder has a significant, positive, influence on specific mechanical properties when fibers are gently mixed at low screw speeds and high fill grades.

Research questions

Two research questions are formulated to accompany the hypothesis.

Question 1: Can key extrusion characteristics such as $\dot{Q}^*$ or the *SME* be correlated with good mechanical properties and thus be used for the selection of the parameters in the mixing extruder?

Owing to complex interactions of processing parameters, especially in the context of the continuous fiber intake, statements calling to process LFT-D compounds at the lowest n_{TSE} possible are derived from research into chopped fibers and, currently, not backed up by LFT-D research. A lot of emphasis is placed on gentle incorporation of fiber materials into the polymer matrix to preserve fiber lengths and improve mechanical performance. This focuses on fiber-polymer and fiber-machine interactions regarding fiber attrition, not considering fiber-fiber interactions as a possibly dominant third factor. To find ideal settings we need to understand general interactions. Ideal in this context implies a mixture of desirable goals like overall mechanical performance but also limited deviations as well as stable reproducibility. Key extrusion characteristics $\dot{Q}^*$ and *SME* comprise different factors as well as machine responses and could represent these interactions.

Question 2: “What role does the plastificate hold at the transition between continuous and discontinuous part of processing regarding fiber microstructure development?”

Fiber orientation, next to content and length is an important but easily overlooked factor for mechanical performance as a uniform orientation is assumed. The semi-finished material is the key driver for resulting fiber microstructure in LFT-D compression molding. The influence of the plastificate regarding the microstructure, for example the differentiation between charge and flow area is known. The extent of influence of the processing factors on the plastificate and in turn on the microstructure is not known.

Approach and limitation

The overall aim of this work is to approach material and process development with the intention to identify an ideal set of processing parameters for PA6 GF LFT-D compounding and to confirm the hypothesis. The following steps are identified:

- Setup and execution of an experimental plan of independent LFT-D factors, spanning a relevant portion of machine capability considering constraints such as resource availability and tool dimensions.
- Characterization of all relevant engineering properties (tensile, flexural and impact) and microstructure (fiber content, length and orientation) as well as the semi-finished material linking compounding and compression molding.
- Development of characterization methods where needed.

This work shall consider factors of the LFT-D line. The compression molding part, while no doubt crucial for developing microstructures, remains constant for all trials.

3 Machines, Materials and Methods

This chapter covers the machines used to run the trials as well as materials used. The vocabulary and general considerations regarding the statistical methods employed are introduced. The developed characterization methods for flow-front and density evaluations are introduced.

Parameters, choice of factors and resulting trial plan are described in the next chapter 4.

3.1 Machines: LFT-D ILC

Polymer granulate dosing was done via gravimetric dosing scales from Brabender GmbH & Co. KG, Duisburg, Germany.

LFT-D processing was conducted on an LFT-D ILC line manufactured by Dieffenbacher GmbH Maschinen- und Anlagenbau, Eppingen, Germany. The LFT-D line comprises two TSEs by Leistritz AG, Nürnberg, Germany. TSE1 was a Leistritz ZSE 40HP GL/32D with 55 kW nominal power. Encoded in the TSEs designation is the inner barrel diameter, d_b = 40 mm, as well as screw length. This length is given as multiples of the diameter. Here, for TSE1 it is 32 x 40 mm = 1280 mm.

TSE2 was a Leistritz ZSE 40 GL/14.5D with a nominal power of 27 kW. TSE2 has a custom barrel setup which is shown schematically in Figure 3.1 with the screw design. It comprises five elements from which two form the fiber intake portion of the line. The fiber intake portion has a higher barrel diameter of d_b = 42 mm to allow for the continuous rovings to be wound around the screw before being sheared once entering the third segment T_{Z3} of TSE2 (cf. Figure 3.1).

3.1.1 Extruder Screw Design

The screw in TSE1 is an all-purpose compounding screw shown in Figure 3.1 (top). Screw design in TSE2 was derived from internal projects optimizing PA6 GF production. Eight screw designs were benchmarked, differences were placement and number of GFM and use of GFK. It was since then used and its suitability was confirmed in related publications (Dahl et al. 2012).

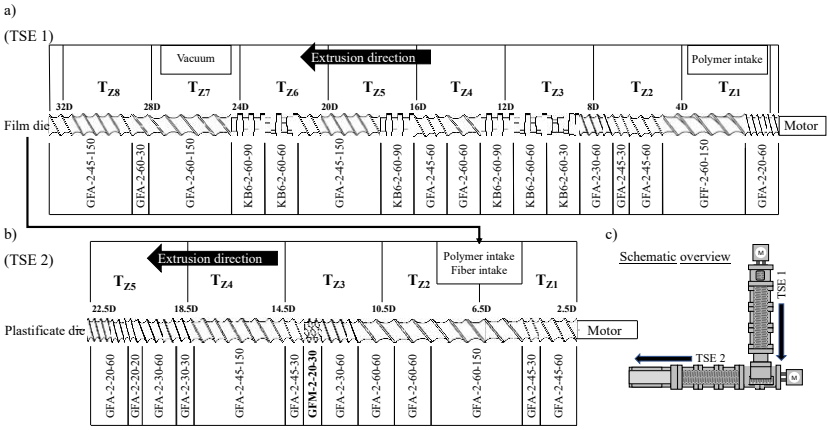

Figure 3.1 Screw design schematics of TSE1 a) and TSE2 b). TSEs are arranged in a perpendicular scheme c). Transfer of polymer melt is indicated by the black arrow from film die (TSE1) to polymer intake (TSE2).

3.1.2 Extruder Die Design

At the end of TSE1 the polymer is fanned out into a film. The polymer enters a channel of 10 mm diameter before being redirected 90° downwards toward a slit with a width of 200 mm and a height of 2 mm.

The plastificate die at the end of TSE2 comprises two parts. A U-shaped fixed lower part and a movable wedge fitting precisely in between the vertical strokes of the U. The height of this die is set by three screws countered by nuts

that define the position of the wedge. This height can be set between 0 mm and 40 mm. The width of the die is 75 mm. The channel of the die is oriented in 30° towards the chain belt where the plastificate is cut and delivered towards the press.

3.2 Machines: Compression Molding

Compression molding was done on a Dieffenbacher DYL 630/500 parallel-guided hydraulic press manufactured by Dieffenbacher GmbH Maschinen- und Anlagenbau, Eppingen, Germany. It has an effective usable press force of 5000 kN while still being parallel guided.

A simple plate mold 400 mm by 400 mm was used to mold plates for characterization. It has a shear edge of approximately 16 mm. Plates are molded to a thickness of 3 mm. The mold is water heated in channels close to its surface.

3.3 Materials

3.3.1 Matrix and Additives

STABAMID PA6 S22 from DOMO was used. It has a melting temperature of 215 °C and a density of 1.14 kg/dm³. A matching masterbatch was specifically produced by DOMO for this work. It is a standard mix of additives for thermal stabilization but without carbon black to preserve the natural color of PA6 which allows for analysis of discolorations as well as experiments with pigments.

For the determination of fiber orientation in the plastificate as well as residence times in the extruder, furnace soot from Printex was used as marker pigment.

3.3.2 Fiber

Glass fiber direct E-glass rovings, StarRov 895 2400, from Johns Manville were used. The linear density is 2400 tex and single filament diameter is 16 µm according to the datasheet. The rovings are coated with a silane sizing compatible with polyamides.

3.4 Methods and Method Development

This part describes the basics of the design of experiments (DoE) method, statistical methods, as well as newly developed methods for the investigation of plastificate density and flow-front skewness. Microstructure characterizations, fiber content, length, and orientation, have been described in chapter 2 State of the Art. Characterization procedure and processing parameters used are described in chapter 4 Experimental.

3.4.1 General Statistical Considerations

Arithmetic mean values are used throughout and marked by the index $()_{mean}$ in this work. Populations of measurement values generated are assumed to be normally distributed (Devore et al. 2021, p. 212). Standard distributions have a mean value µ. Value populations have different distances to µ, 68.3 % of which are in the interval $\mu \pm \sigma$, where σ is the standard deviation. Standard deviation σ is abbreviated SD to cause no confusion with the quantity of strength σ. The coefficient of variation (*CV*) is defined as the ratio of σ and µ and can be given as a fraction in %. (Devore et al. 2021)

3.4.2 Design of Experiments

The design of experiments method is a standardized, statistics backed, tool to investigate a technical system in its boundaries with parameters and factors and determine what effects or interactions influence quality features (Siebertz et al. 2017). Relevant vocabulary:

- System: The object of investigation.
- System boundaries: Delimiting the system from the environment.
- Parameters: The totality of all input variables, controllable and else.
- Factors: Controllable parameters actively changed during the investigation.
- Quality feature: Quantifiable indicator whether a system fulfills its intended function.
- Effect: Impact of a factor on a quality feature.
- Interaction: Occurs when the effect of a factor depends on other factors.

The goal is to learn about the effect of factors on quality features with minimal time and resource effort. Factors are set to at least two levels sufficiently far apart. Factor combinations determine trial points of the investigation. Various experimental designs with suggested factor combinations are available. A Face-Centered-Central-Composite-Design (FCCCD) was chosen for this work after preliminary tests in which processing limits were determined. In FCCCD quadratic relationships between factors can be detected but the factors to be varied do not exceed the maximum allowable processing limits.

3.4.3 Identification and Treatment of Outliers

Discussion of measurement data is sensitive to extreme results leading to high deviations. Sorting all data points n from lowest to highest, the median value can be determined by splitting the data set in half (for odd n). Splitting the halves further leads to the medians of the lower (q_1) and upper quartiles (q_3). The interquartile range (IQR) is defined as the spread of those two data points marking the middle 50 % of measurement data. (Devore et al. 2021, p. 36)

$$IQR = q_3 - q_1 \tag{3.1}$$

Measurement data are subjected to a search for outliers where appropriate. An outlier is defined as all points n in a set whose values x satisfy either (Devore et al. 2021, p. 37)

$$x < q_1 - 1.5\,IQR \tag{3.2}$$

or

$$x > q_3 + 1.5\,IQR \tag{3.3}$$

Identified outliers are excluded from mean value calculations. This procedure is conducted for all results of mechanical testing and w_f measurements.

3.4.4 Determining Significance with t-Test and p-Values

In this work, the null hypothesis H_0 is that there is no difference between groups of measured values while the alternative hypothesis H_a is that there is a significant difference. Test procedures, employed to verify or falsify H_0, comprise a function of sampled data and a rejection region on which this decision is based (Devore et al. 2021, p. 498 ff).

A function of sampled data can be determined via Student's t-test which is used to determine whether two mean values are significantly different. A P-value is attributed to the t value via table (Student 1908) or software. The P-value is the probability of the assumption H_0 being true (Devore et al. 2021, p. 528).

This determination of significance is done via the statistics tool in Origin by OriginLabs and equations used are not listed here. For testing it is assumed both populations are normally distributed and of different variances. The Welch correction for these different variances is applied (Devore et al. 2021, p. 570).

3.4.5 Measuring Plastificate Density

The plastificate is subject to lofting (cf. 2.5.4 (p. 20)) resulting in a reduced density relative to the theoretical value applying the rule of mixture. The method used to determine plastificate density was developed by Sven Löwe for his bachelor's thesis under the supervision of this author (Löwe 2022).

Density is the ratio of mass per volume. Mass is determined by weighing. The volume of the porous plastificate is determined by contactless means. A stereo camera system, GOM ARAMIS by Carl Zeiss GOM Metrology GmbH, Braunschweig, Germany, is deployed to 3D scan plastificates.

The volume of plastificates is determined in the proprietary software of the camera. Limits of this volume measurements were found at high n_{TSE2} = 100 rpm in combination with low w_f = 20 % where big air bubbles in the plastificate negatively impact the measurement result (Löwe 2022, p. 37). The plastificate density ρ_{plast} is calculated via equation (3.4).

$$\rho_{plast} = \frac{m_{plastificate}}{V_{plastificate}} \tag{3.4}$$

With $m_{plastificate}$ as the mass of the plastificate and $V_{plastificate}$ as the volume of the plastificate. Core finding of this investigation was a clear, linear decreasing, correlation between processing parameters, especially n_{TSE} and the density of the plastificate.

3.4.6 Determining Flow-Front Skewness

Flow-fronts develop once the plastificate is in contact with both mold halves during the compression molding step. Basics of mold filling are explained in 2.6 with a visualization of core mechanics in Figure 2.7. By fixing metal blocks onto the tool, the mold is not filled in its entirety and a flow-front is preserved (also called short-shot (Thattaiparthasarathy et al. 2008, p. 1515)). The

progress of mold filling is not evenly distributed in all areas. This leads to the term flow-front *skewness*, not to be confused with the statistical term.

To quantify the skewed shape of the flow-front, a method was developed by Luca Meckes under supervision of this author (Meckes 2024). Figure 3.2 illustrates the approach to flow-front characterization. In parallel, a molding study with accompanying characterization and simulations was conducted by (Schelleis et al. 2025b). Additional information can be found there as well.

The following steps lead to the flow-front skewness characteristic s_{ff}.

- Step a); Molding of an LFT-D plate with frozen mold filling process. The scheme of plastificate placement, extrusion and flow direction is shown as an overlay. The mold is filled to about three quarters.
- Step b); A photograph is taken from above. The photograph is mirrored to ensure that the direction of extrusion matches the direction of the x-axis later. Note that the old and new end of the plastificate change position here.
- Step c); The shape of the flow-front is traced point by point in a free online software called PlotDigitizer by PORBITAL and transferred into a series of x (marking the direction of extrusion) and y (marking the flow distance) -coordinates. This curve can be analyzed in Origin by OriginLabs. A line of constant y-coordinate is drawn through the minimum. This line delimits the rectangle of fully filled plate body, see originally colored photo in step c). The grey colored flow-front area is further analyzed.
- Step d); The x-coordinate of the center of the flow-front area is calculated. Calculating the relation of the x-coordinate and the middle of the mold (x = 200 mm in this case) results in s_{ff} = 22.05 %.

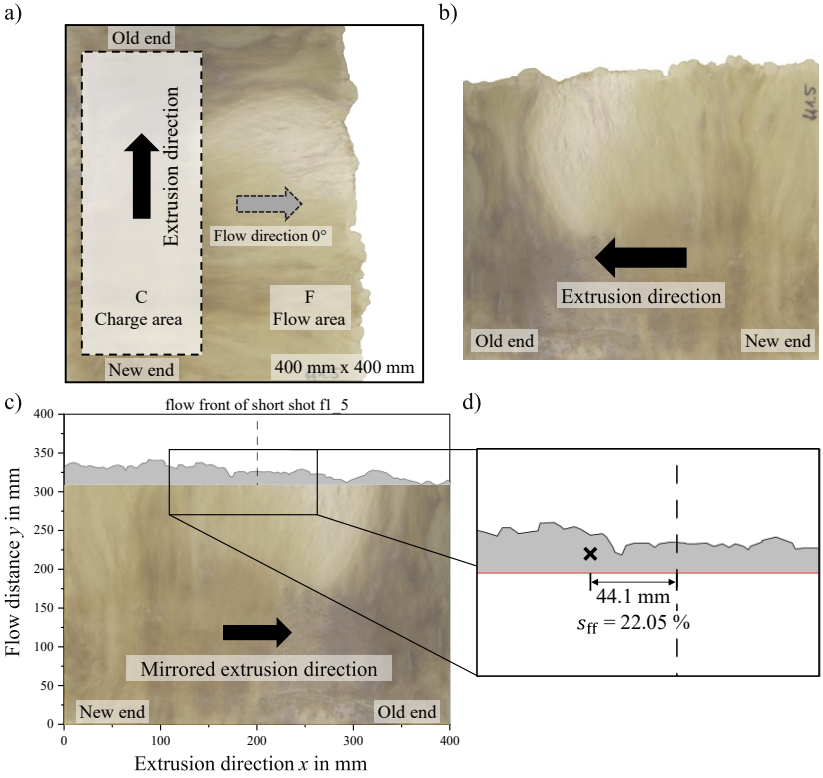

Figure 3.2 Determining flow-front skewness s_{ff} in four steps from top left a) to bottom right d). a) Orientation of the flow-front regarding production; b) photography of the flow-front; c) photograph to curve transformation and processing; d) visualization of s_{ff} as distance to the mold center. (Schelleis et al. 2025b)

Characterized in this fashion, the resulting s_{ff} value is independent of the flow length as the calculation starts from the minimum of the flow-front. It is also generally independent of mold geometry as s_{ff} is calculated in relation to the mold center. The parameter s_{ff} represents the relative distance of the centroid of material distribution from the mold center.

3.4.7 Determining Fiber Orientation through Tensile Discs

While the methodology was introduced and validated by Tröster (cf. 2.3.2 (p. 12) (Tröster 2004)) during this work both the repeatability of single tensile discs as well as the variance between plates of the same test series were quantified. An improved method to determine the resulting preferential fiber orientation from the characterization results was presented by Meckes (Meckes 2024).

The elliptical shape of the tensile strength measurement results can be fitted in Origin after two steps. First, a transformation from polar to cartesian coordinates must be performed. Secondly, Origin assumes the axes of the ellipses to be congruent to the x-y-coordinates. This is not the case as the vertex is not expected to be in 0° direction (x-axis). The coordinates are transformed again via rotation matrix, introducing the angle ψ between the vertex and the x-axis. The resulting function is solved for ψ where measurement results approach the best elliptical fit. This angle ψ equals the main fiber orientation φ_v. (Meckes 2024)

Deploying this fit method improves upon Tröster's approach as it considers all measurements and not only 3 measurements, that of the highest tensile strength and both adjacent tensile strengths (Tröster 2004, p. 87).

The repeatability of single tensile disc measurements is high. Characterizing the same disc five times leads to FOs between φ_v =9.4° and φ_v =10° with one outlier at φ_v =7.2°. These deviations account for user induced inaccuracies while clamping and turning the sample.

Characterizing five tensile discs from five subsequently manufactured plates, Meckes found φ_v to be between 3.7° and 10° which presents a high deviation.

4 Experimental

The general procedure of the tests is described. Choice of experimental factors as well as all relevant machine settings are explained here. Sample dimensions as well as sampling locations are described. Relevant normative standards for testing are listed.

4.1 LFT-D Processing Approach

A plan based on the experiences from previous trials is presented in Table A.1 in the Appendix. It was followed for every trial point and serves as a standard recipe for LFT-D production with a material development aspect. Over the course of three weeks one set of parameters was processed in the morning and one set of parameters was processed in the afternoon.

The run in time $t_{\text{run-in}} = 20$ min should be seen as an absolute minimum for running the LFT-D line in a stable state (Löwe 2022, p. 24).

4.2 LFT-D Factors and Parameters

Kohlgrüber names screw speed, throughput, heating temperatures in combination with screw and die design as the important parameters in extrusion (Kohlgrüber 2016, pp. 683–684). Screw speed as well as polymer throughput and roving amount are chosen as factors. They make up total throughput $\dot{Q}$ as well as w_{f}, as explained in equations (2.1) and (2.11).

- Screw speed of TSE2 n_{TSE2} in rpm.
- Polymer throughput m_{p} in kg/h.
- Number of rovings n_{rov} in pieces.

4.2.1 How Limitations of the LFT-D Equipment Dictate the Parameter Space

Extruder torque M_{TSE} and volume throughput $\dot{V}$ are limited by the TSEs motor (clutch, really) and machine geometry. Factors are varied as per DoE in preferably big steps. The most extreme combinations of factors in LFT-D processing can result in a w_f and high $\dot{Q}$.

- At high w_f , higher M_{TSE} is expected. A w_f limit of 60 % was formulated from experience, the highest w_f produced to that date was $w_f = 55$ %.
- Screw design and n_{TSE2} allow for a certain $\dot{V}$, which, once exceeded, will cause TSE 2 to overflow at the fiber intake area. A lower limit of $n_{TSE2} = 45$ rpm was chosen. Double that, $n_{TSE2} = 90$ rpm, was chosen as the high level.
- The LFT-D line is designed to be fed by $n_{rov} = 24$ at once. This amount can be fed into the fiber intake side by side without overlap. Accordingly, $n_{rov} = 24$ was chosen as the high level. Eight fiber rovings were chosen as the low level. This choice allows the mid-level, $n_{rov} = 16$, to be an integer as fiber rovings cannot be split.
- Dosing scales work reliably in a certain motor speed range. A lower dosing limit of $m_p = 20$ kg/h was determined in trials for this setup. Double that, $m_p = 40$ kg/h was chosen as the high level.

4.2.2 Trial Points DoE

The FCCCD experiment design derived from the boundaries formulated in 4.2.1 is given in Table 4.1 along with run order V and trial name designation N. The run order was determined randomly by the DoE software. The center point was repeated a total of three times to check for reproducibility. The boundaries are respected for all combinations. Calculating w_f from formula (2.1) and (2.11) indicates a distribution of trials between $w_f = 11$ % and $w_f = 60$ %.

Table 4.1 FCCCD trial plan with all factor combinations.

Run order V	Trial name N	Position in DoE	n_{TSE2} in rpm	m_p in kg/h	n_{rov} in pcs.
V1	N11	Face	67.5	20	16
V2	N5	Corner	45	20	24
V3	N15	Center	67.5	30	16
V4	N14	Face	67.5	30	24
V5	N7	Corner	45	40	24
V6	N17	Center	67.5	30	16
V7	N6	Corner	90	20	24
V8	N3	Corner	45	40	8
V9	N12	Face	67.5	40	16
V10	N16	Center	67.5	30	16
V11	N10	Face	90	30	16
V12	N4	Corner	90	40	8
V13	N1	Corner	45	20	8
V14	N2	Corner	90	20	8
V15	N9	Face	45	30	16
V16	N13	Face	67.5	30	8
V17	N8	Corner	90	40	24

4.2.3 Secondary and Resulting Parameters

The LFT-D processing equipment relies on various inputs, and not all can be mentioned here. All settings were documented and are available as an electronic resource for detailed investigations on demand. Relevant parameters that were kept constant are described here.

Temperatures

To facilitate an ideal impregnation of the fiber the temperatures are chosen on the high side of the manufacturer's recommendations throughout both TSEs,

plastificate die as well as chain belt and tunnel after TSE2 exit. All TSE elements are heated to 275 °C and the plastificate die is set to 265 °C.

Plastificate die height

The die height is set to 39 mm so that all plastificates fit the mold as they are shorter at high die heights. Trials set at high n_{TSE2} and high w_f were considered here. It is kept at this height to keep processing conditions similar.

Belt speed

The plastificate exiting TSE2 is discharged onto a chain belt. Its speed is determined by inputs in the LFT-D line (die dimensions, throughput, material density, fiber content). The machine allows for manual correction of the belt speed. This option was not used during the trials.

4.3 Choice of Molding Parameters

The velocity profile in Table 4.2 comprises gap width between mold surfaces and closing speed at which the press ram is moving at that point. The profile follows the points in a linear fashion at the end, when material is filling the mold the closing speed is at a constant 5 mm/s.

Table 4.2 Closing velocity profile of hydraulic press for manufacturing sample plates.

Gap width in mm	Closing speed in mm/s
40	80
30	40
20	30
15	5
0	5

The velocity profile of the press was set to be slow, so that material would not leak out of the mold which leads to increased deviations in plate weight and thickness between plates.

For compression molding of PP GF LFT-D, Henning reported a process optimum at 200 bar in-mold pressure (Henning 2001, p. 177). A press force of 3200 kN was set accordingly. The mold temperature was set to 80 °C and 85 °C for the upper and lower mold half respectively.

4.4 Characterizations

All products of the process were characterized. The plastificate was weighed and measured. Flow studies were assessed for their skewness and plate microstructure as well as mechanical properties have been characterized.

4.4.1 Plastificate Characterizations

Temperature in the plastificate is measured in the moment where it was produced and is ready to mold. A Testo 725-2 temperature logger and matching probes were used manufactured by Testo SE & Co. KGaA, Titisee-Neustadt, Germany.

All other properties are examined after quenching plastificates in water immediately after production at roughly the same time as if they were molded. This stops lofting. The plastificates are dried to equilibrium at 80 °C for all further characterizations. The plastificates are weighed after drying. Dimensions are measured via GOM, and density is derived from those measurements (cf. 3.4.5).

The fiber orientation in the plastificate is also investigated (cf. 2.5.5).

Parameters are introduced to better describe plastificate lofting. Figure 4.1 shows these parameters and visualizes their interactions. In the top right the relation between calculated ρ_{calc} and actual density ρ_{plast} is shown

schematically. The ρ_{plast} will always be lower than ρ_{calc} and the actual plasticate physically bigger than the calculated with $V_{plast} > V_{calc}$. Nominal height h_D and width w_D of the plastificate are denoted with the subscript D for TSE2 die as the die settings are the basis for this calculation. The discrepancy between ρ_{calc} and ρ_{plast} is caused by lofting (cf. 2.5.4). While lofting occurs in all directions it is especially important in extrusion direction (black arrow in Figure 2.6, Figure 3.2 and Figure 4.1). To highlight this, the distance, in extrusion direction, between the middle of V_{calc} and V_{plast} is called D_l. Lofting is also stronger towards the old end as is indicated by different distances between dashed and solid lines.

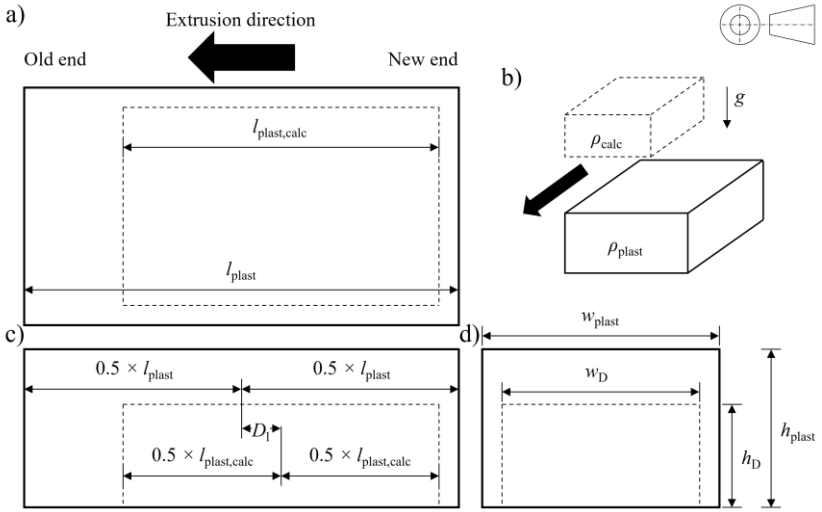

Figure 4.1 Schematic description of plastificate lofting. Dimensions of a plastificate in theoretical considerations (subscript "theo", dashed lines) and how it is processed (subscript "plast", solid lines).

4.4.2 Flow-Front Skewness

Flow-front skewness was characterized according to Meckes (Meckes 2024).

4.4.3 Cutting Schemes and Sample Dimensions

Literature shows, that sample placement is critical and from slightly different locations big property deviations can occur. While sampling for this thesis, charge (C) and flow (F) areas are considered. All samples were taken in 0° direction. All plates were molded to a thickness of 3 ± 0.1 mm. The sample thickness is accordingly. An increased thickness in the middle of the mold is generally observed (Meckes 2024, p. 62).

For the measurements of w_f (via TGA) and l_f (via FASEP) three sample locations are defined according to Figure 4.2 b). The distance between mold wall and center point of the samples is 100 mm. The samples are named C, C-F and F according to their respective positions. The samples have a radius of 25 mm which is determined by crucible size of the TGA itself.

Groups of mechanical samples are placed in C and F areas. The groups are identical, just mirrored along the flow axis of the plate. The general locations of the sample groups are depicted in Figure 4.2 c).

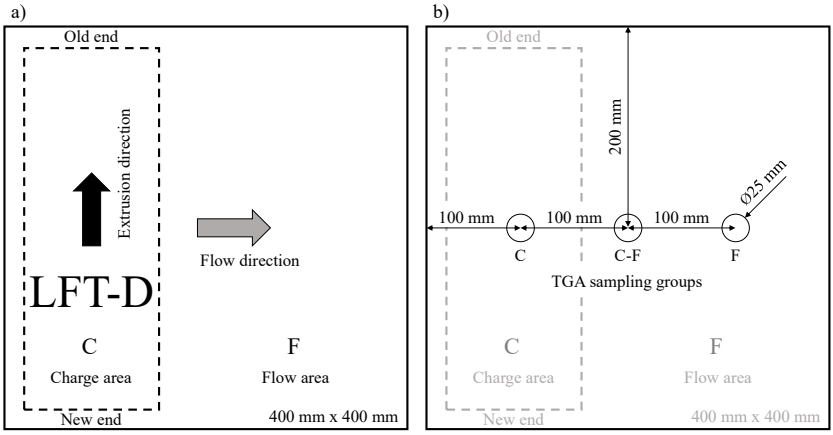

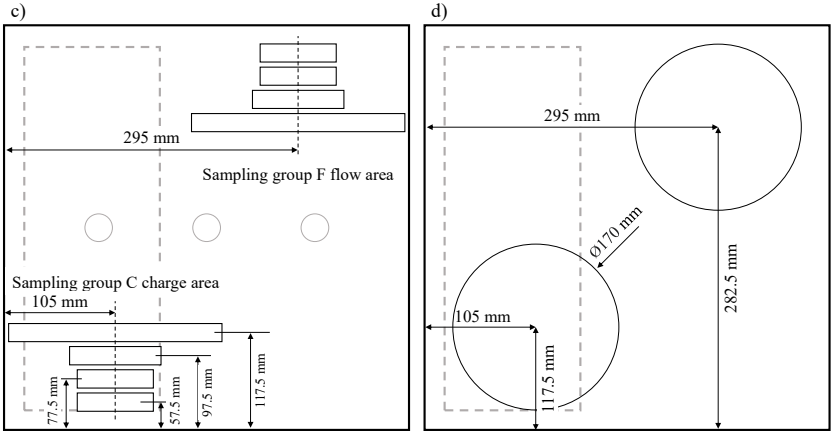

Figure 4.2 Molding, a), and sampling schemes, b) - d). TGA and FASEP samples along the flow direction in C, C-F and F areas b). Mechanical samples c). Tensile discs d).

Exact sample measurements and normative standards are given in Table 4.3. Tensile disc samples are placed at the same location as the tensile bars to have an ideal agreement between fiber orientations at this specific location, as shown in Figure 4.2. d). Tensile disc samples have a diameter of 170 mm.

Table 4.3 Overview of sample dimensions and characterization standard.

Sample	Characterization according to	Length in mm	Width in mm
tensile	DIN EN ISO 527-1 2 mm/min	200	15
flexural	DIN EN 14125 ISO 1.3 mm/min	80	15
impact	DIN EN ISO 179-1/1fU	75	15
tensile disc	ICT development cf. (Tröster 2004; Maertens 2022)	d = 170 mm	
TGA/ FASEP	(Hartwich et al. 2009)	d = 25 mm	

Additionally, to mechanical characterizations, an experiment was conducted where the F area across the entire width of the plate was characterized. As shown in Figure 4.3, nineteen tensile samples were placed side by side in the flow area with as little as 5 mm space in between. The edge areas are considered here to highlight the influence of the proximity to the mold wall. These edge areas are otherwise not characterized.

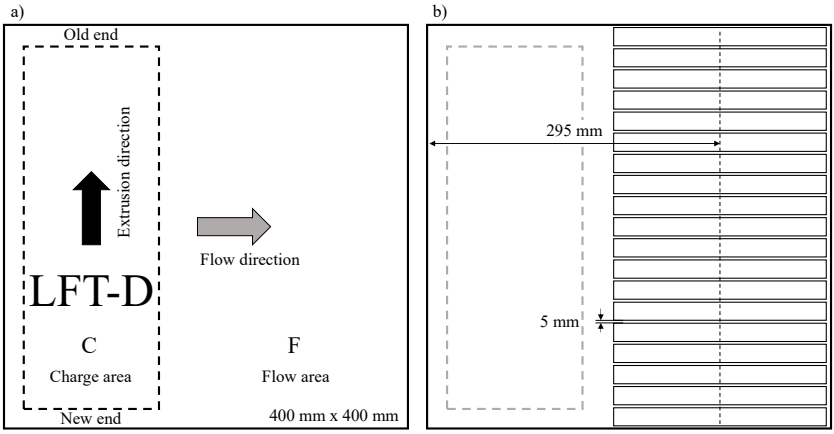

Figure 4.3 Sampling scheme of tensile samples across the entire width of a plate in the flow area.

4.4.4 Determining Fiber Fraction

Fiber fraction is determined by TGA on a TGA801 by LECO Instrumente GmbH, Mönchengladbach, Germany. A heating ramp rate of 10 °C/min is set to the target temperature of 650 °C. The target temperature is held for two hours while the weight change is tracked.

4.4.5 Determining Fiber Length

Samples from fiber fraction characterization are diluted twice in water under gentle stirring and utilization of an ultrasonic bath. In every dilution step a fraction of the sample is discarded and replaced with more water. The suspension is transferred on a flatbed scanner and analyzed via FASEP (Hartwich et al. 2009). For every measurement between 5.000 and 10.000 individual fibers were measured.

4.4.6 Determining Fiber Orientation

The specimens were preloaded once before actual testing to settle the clamping area of the machine. Testing was conducted at Institute for Applied Material Science at KIT on a ZwickRoell GmbH & Co KG, Ulm, Germany, universal testing machine according to Tröster (Tröster 2004) (cf. 3.4.7 (p. 58)). The fiber orientation was calculated according to Meckes (Meckes 2024) (cf. 3.4.7).

4.4.7 Sample Conditioning

All samples have been conditioned after cutting. The samples were stored in a convection oven at 80 °C. The samples were weighed every day and dried to an equilibrium where the change in weight was less than 0.1 % on three consecutive days.

4.4.8 Mechanical Properties

All characterizations are conducted in adherence to or closely based on industry standards. They were carried out at the facilities of ICT, Pfinztal, Germany.

Tensile modulus and strength

Tensile testing was carried out according to DIN EN ISO 527-1 with a testing speed of 2 mm/min on a “inspekt table 10 kN” by Hegewald & Peschke Meß- und Prüftechnik GmbH, Germany.

Flexural modulus and strength

Flexural testing was carried out according to DIN EN 14125 ISO with a testing speed of 1.3 mm/min on a “inspekt table blue 5 kN” by Hegewald & Peschke Meß- und Prüftechnik GmbH, Germany. A pre-load of 2 N was applied to settle the machine.

Impact toughness

Unnotched impact testing was conducted according to DIN EN ISO 179-1/1fU with a span of 62 mm and a pendulum energy of 5 J. Characterizations are carried out on a CEAST9050 by Instron GmbH, Germany.

5 Results: Process Development

Results of process development shown here are taken from machine logs, measurements during production and characterizations of semi-finished materials. This section deals with everything but the final products, plates, which will be discussed in chapter 6. Here, and in the remaining work, key findings and processing recommendations are highlighted with a box.

A set of factor combinations, trial points, are selected for the presentation of the results and discussion. Assigned color schemes facilitate easier reference. The selected trial points are lowest and highest w_f as well as one of the center points. Key information is presented in the following Figure 5.1.

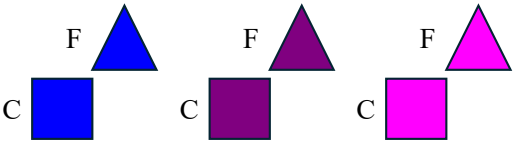

		Lowest w_f	Center point	Highest w_f
$w_{f,mean}$	in %	18.29	30.53	57.95
$w_{f,C}$	in %	16.13	27.14	57.08
$w_{f,F}$	in %	20.93	33.48	58.85
n_{TSE2}	in rpm	90	67.5	90
m_{pol}	in kg/h	40	30	20
n_{rov}	in pcs.	8	16	24

Figure 5.1 Selected factor combinations and their assigned color schemes. The square marks measurements from the C area and the triangle marks measurements from the F area.

In the following tables the selected factor combinations ([S]) and center points ([C]) are also indicated in the "remarks" column.

5.1 LFT-D In Line Compounding

In this section all relevant measurements from the LFT-D line are exhibited.

5.1.1 Fiber Intake Speed

Fiber intake speed v_{intake} determines what length of fiber roving is drawn into the TSE per revolution of the screw. Knowledge of v_{intake} is important for w_f prediction (cf. equation (2.11) (p. 19)). Figure 5.2 shows measured v_{intake} values at respective roving positions. Here, roving 1 is at the beginning of the fiber intake slot and roving 24 is further down extrusion direction (indicated by the arrow) towards the end of the fiber intake. Data points in both graphs are the same, only color coded as sorted by n_{TSE2} a) and n_{rov} b).

While the first roving at position 1 is drawn into the extruder at similar speeds for all trial points, v_{intake} drops off in extrusion direction depending on n_{TSE2} and n_{rov}. A possible explanation is, that the first roving has room to wind around the screw in an elliptical fashion, covering more length per rpm than the subsequent rovings which are blocked by previous rovings. This would make n_{rov} (Figure 5.2 b)) the deciding factor here. Curves are monotonously falling for all, but three parameter sets that are run at the highest LFT-D throughputs. For these m_{LFT-D}, the last rovings are dragged in faster again.

Truckenmüller measured v_{intake} for an injection molding screw with a mechanical device (Truckenmüller 1996, p. 69) and also reported an increase in v_{intake} for higher screw speeds (Truckenmüller 1996, p. 111). Tröster's statement regarding the re-evaluation of v_{intake} for all material and parameter combinations is valid (Tröster 2004, p. 57) as differences in mean v_{intake} will lead to w_f deviations. This was observed for PC GF LFT-D where a fixed v_{intake} led to a systematically heightened w_f throughout (Schelleis et al. 2023c, p. 2051).

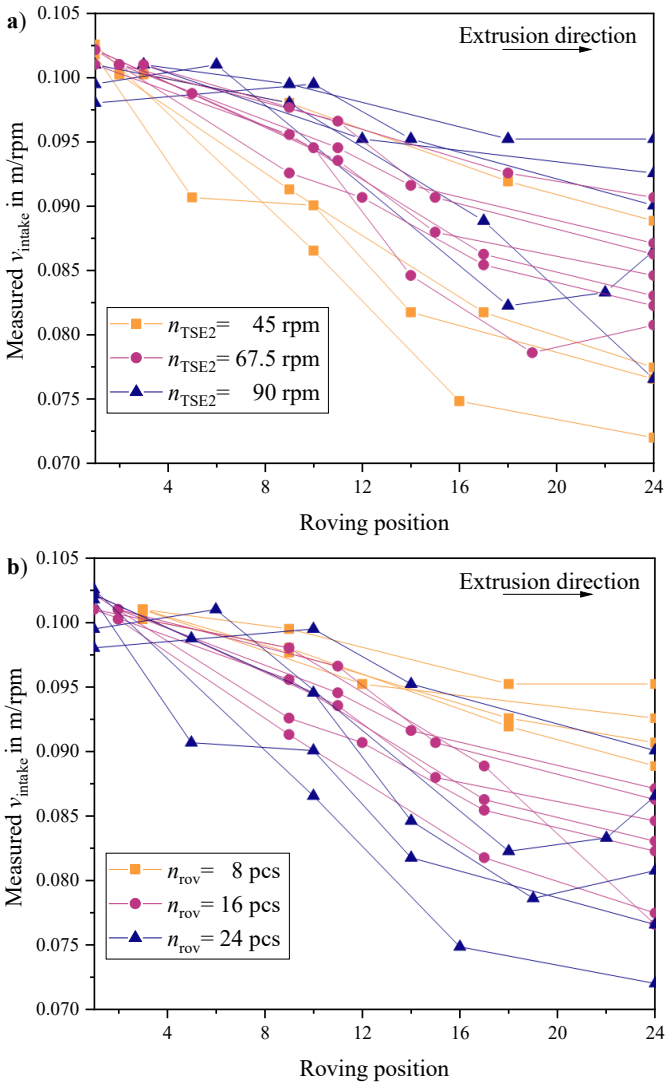

Figure 5.2 Measurements of v_{intake} at roving positions grouped by n_{TSE2} a) and n_{rov} b).

A mean v_{intake} can be measured at roving position 12.

For low n_{rov} and high n_{TSE2} the deviation from $v_{intake,mean}$ would be lower. This $v_{intake,mean}$ is used from here on for calculations of m_f and subsequently all derived parameters ($w_{f,calc}$, m_{LFT-D}, $\dot{V}^*$). The validity of this approach is discussed in 7.2.1 (p. 123) where calculated $w_{f,calc}$ is compared to $w_{f,TGA}$ as well as w_f determined by sampling the entire plate.

5.1.2 Extruder Temperatures and Torque

Temperatures and torque were monitored to ensure that an equilibrium was reached before any sampling took place. Monitoring and data logging started once the machine was in production mode and target n_{TSE2} was reached (cf. Table A.1 (p. 169)). A timeframe of 20 min was defined according to findings from pre-trials as an adequate time for temperatures T_{Z15} and torque M_{TSE2} to be stable. Starting at the 20 min mark, another 20 min of temperature as well as torque measurements of TSE2 were averaged.

In Figure 5.3 both M_{TSE2} a), and T_{Z15} b) are displayed with respect to n_{TSE2} and n_{rov}. Torque clearly increases while increasing n_{rov} at all n_{TSE2}. Processing higher w_f (reference the color palette to the right) requires less torque at higher n_{TSE2}. The same relation between n_{TSE2} and M_{TSE2} was observed during development of PA6 CF LFT-D with reference to favorable electrical usage and related processing costs at higher n_{TSE2} (Dahl et al. 2012, p. 12). Kloke discusses increasing M_{TSE2} via increased throughput for improved fiber lengths (Kloke et al. 2011, p. 68). This is generally possible, selected m_{LFT-D} are shown in Figure 5.3 a) for reference, as increasing m_{LFT-D} will increase M_{TSE2}. However, w_f is dominant regarding torque requirement regardless of m_{LFT-D} as the difference between highlighted data points labelled 53.7 kg/h and 33.1 kg/h shows.

Fiber fraction w_f is the key driver in TSE torque requirements.

Fiber intake temperatures plateau with very low deviations at lower levels for increasing w_f. The placement of data points is almost reversed from torque. Higher polymer viscosities will lead to higher M_{TSE2}, however w_f seems to be the key driver here.

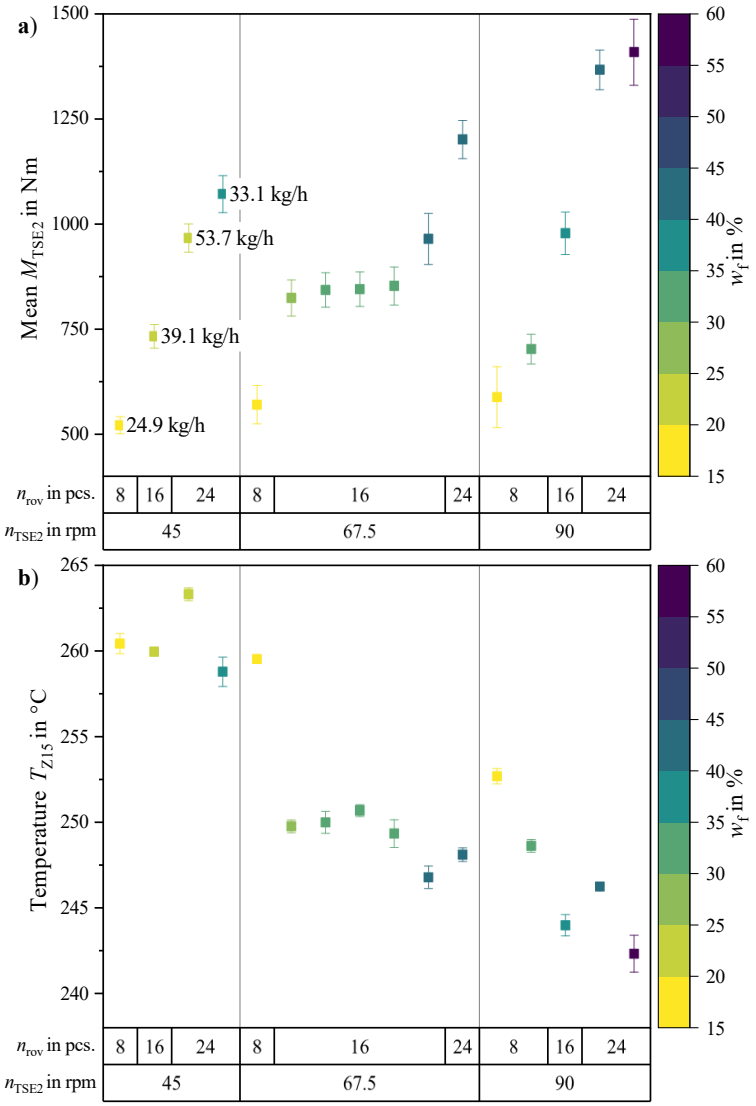

Figure 5.3 Measurements of TSE 2 torque a) and T_{Z15} b). Sorted by n_{TSE2} and n_{rov}. Color coded according to their w_f.

5.1.3 Derived Key Characteristics SME and $\dot{Q}^*$

Closely related to M_{TSE2} is the *SME* (cf. 2.5.2 (p. 17)). The actual *SME* can only be calculated with the actual throughput $m_{LFT\text{-}D}$ in turn calculated with equation (2.11) and v_{intake} (cf. Figure 5.2 (p. 73)). Another key characteristic, the $\dot{Q}/N$ ratio $\dot{Q}^*$ is calculated with $m_{LFT\text{-}D}$ as well. Both are shown in Table 5.1 sorted by $w_{f,mean}$, discussed in depth in 6.1, as well as n_{TSE2} for reference. While unusual, $\dot{Q}^*$ is given in g instead of kg for a clear presentation.

Table 5.1 Derived key extrusion characteristics *SME* and $\dot{Q}^*$ sorted by $w_{f,mean}$.

$w_{f,mean}$ in %	Run order/ remark	$m_{LFT\text{-}D}$ in kg/h	n_{TSE2} in rpm	SME in kWh/kg	$\dot{Q}^*$ in g
18.29[S]	V12, a	50.0	90	6.7	9.3
18.81	V13, a	24.9	45	5.9	9.2
19.63	V16, a	37.4	67.5	6.5	9.2
22.79	V15	39.1	45	5.2	14.5
24.89	V5	53.7	45	5.5	19.9
25.32	V9	54.1	67.5	6.6	13.4
30.53[S,C]	V10	44.2	67.5	7.8	10.9
30.93[C]	V6	44.6	67.5	8.1	11.0
31.19[C]	V3	44.3	67.5	8.0	10.9
33.50	V14	30.1	90	13.3	5.6
37.57	V2, b	33.0	45	7.9	12.3
39.22	V11	48.9	90	11.1	9.1
40.72	V1	34.6	67.5	11.8	8.5
40.76	V4, b	51.0	67.5	9.8	12.6
41.01	V17, b	68.2	90	11.1	12.6
57.95[S]	V7	49.8	90	16.1	9.2

[S] selected parameter set; [C] center point parameter set

Both *SME* and $\dot{Q}^*$ are featured in literature to discuss fiber attrition as it provides certain comparability even across vastly different factors. This is limited to lower w_f as its interaction with $m_{LFT\text{-}D}$ is nonlinear (cf. Figure 2.5).

The first three parameter sets by w_f, from w_f = 18.29 % to 19.63 % (remarked "a" in Table 5.1), are produced across all factor levels except keeping n_{rov} the same. Increasing n_{TSE2} and m_p will increase $m_{LFT\text{-}D}$ while keeping w_f steady. This results in similar M_{TSE2} levels at 500 Nm to 600 Nm (cf. Figure 5.3 a), lowest M_{TSE2} measurements). Accordingly, similar $\dot{Q}^*$ are calculated as more $m_{LFT\text{-}D}$ is processed at higher n_{TSE2}. Another triplet comprises parameter sets V2, V4 and V17 (cf. Table 4.1 (p. 61)). They are shown towards the bottom of Table 5.1 (remarked "b"). The ratio $\dot{Q}^*$ is still comparable while *SME* is not.

5.1.4 Extruder Fiber Length Measurements

Fiber length samples from TSE2 could not be characterized because the fibers were too long (approximately 40 mm to 50 mm).

5.2 Plastificate Properties

Special attention was given to the plastificate as the process interface between compounding and compression molding. Temperature and fiber orientation were characterized as these properties are suspected to influence fiber orientation after compression molding. Weight and density are another focus of investigation as indicators for process stability and, in the case of density, potential cause of fiber orientation deviations. The dimensions, especially length, are also discussed.

5.2.1 Plastificate Temperature before Molding

One influential factor suspected to influence FOD is plastificate temperature T_{plas} differing from plastificates old end $T_{plas,o}$ to new end $T_{plas,n}$ (Radtke 2009, p. 88). Probes stuck 60 mm deep into the old and new end of the plastificate

simultaneously do not show temperature differences exceeding 1 % (e.g. ΔT between 275 °C and 272 °C). All measurements are shown in Table 5.2. The core temperature of plastificates is slightly beneath but close to TSE2 temperature (set to 280 °C).

The plastificate core does not vary in temperature from old to new end.

Similar measurements were conducted for PC GF and PA6 CF LFT-D in different trial campaigns conducted parallel to this work. Both cases showed a similar behavior (Scheuring et al. 2024, p. 14).

It is unclear why two measurements are especially low at 267 °C to 269 °C (remarked “a” in Table 5.2). As no relation to the factors can be found, an inadequate measurement procedure is suspected. The measurement procedure is self-designed and difficult to conduct within a controlled framework. The air entrapped in the plastificate is insulating the probes. This amount of air is not always the same but closely related to the lofting phenomenon. Pressure must be applied to the plastificate without compromising the sampling location (that is, stepping on it, carefully).

From these measurements Radtke’s hypothesis cannot be backed for PA6 GF. An explanation that could work for all observations can be found in Scheuring’s work on orientation dependent properties of LFTs which was conducted in close cooperation and discussions with the author of this thesis (Scheuring et al. 2024, p. 14). Here a cone shaped temperature distribution throughout the plastificate is suggested. This would allow for the temperature along the center line, from old to new end, to be the same while the mantle of the plastificate cools down starting from the old end. This supposed cone shape is backed by observations regarding the plastificate lofting discussed further in this work (cf. Table 5.4 (p. 82)).

Table 5.2 Plastificate temperature $T_{plas,o}$ and $T_{plas,n}$ and the gradient ΔT_{plas} given in absolute and percent values.

$w_{f,mean}$ in %	Run order/ remark	$T_{plas,o}$ in °C	$T_{plas,n}$ in °C	ΔT_{plas} in °C	ΔT_{plas} in %
18.29[S]	V12	274	275	-1	0.36
18.81	V13, a	268	267	1	0.37
19.63	V16	272	270	2	0.74
22.79	V15	274	274	0	0
24.89	V5	275	272	3	1.09
25.32	V9	274	275	-1	0.36
30.53[S,C]	V10	275	274	1	0.36
30.93[C]	V6	275	272	3	1.09
31.19[C]	V3	274	271	3	1.09
33.50	V14	277	277	0	0
37.57	V2, a	269	268	1	0.37
39.22	V11	276	277	-1	0.36
40.72	V1	275	276	-1	0.36
40.76	V4	274	273.5	0.5	0.18
41.01	V17	278	276	2	0.72
57.95[S]	V7	281	278.5	2.5	0.89

[S] selected parameter set; [C] center point parameter set

5.2.2 Plastificate Weight and Dimensions

Both plastificates and molded plates are considered for weight measurements as no mass is lost during molding and $m_{plast} = m_{plate}$ can be assumed. Clearly, m_{plast} correlates with w_f. This connection can be observed in Figure 5.4 as well in Table 5.3. Standard deviation for m_{plast} is between 1 % and 2 % with a cyclical pattern between individual measurements. This pattern is shown in Figure 5.4 where three selected parameters are shown.

Weight and resulting thickness changes can be expected during production.

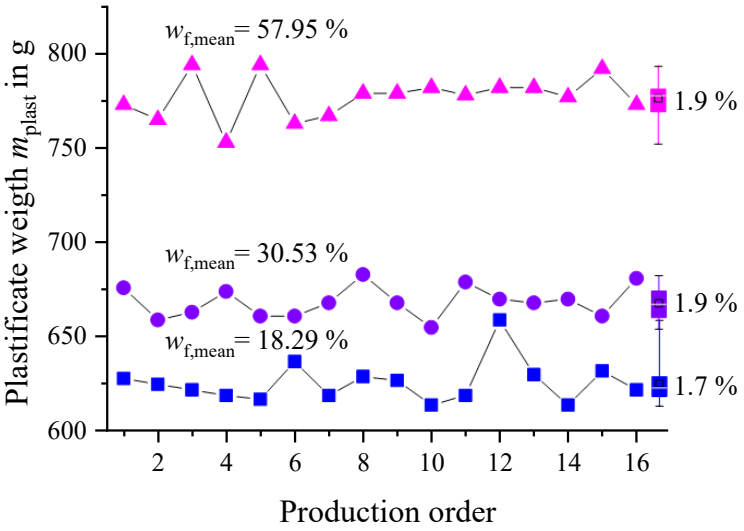

Figure 5.4 LFT-D plastificate weight m_{plas} across production order for select parameters.

Absolute plastificate length l_{plast} is potentially relevant to mold filling because of a developing radial flow (cf. Figure 2.7 (p. 24)). It strongly correlates with ρ_{mean} ($r = -0.85$) and therefore w_f ($r = 0.65$). The length of the plastificate plays a potential role in resulting fiber fractions across molded plates (cf. Figure 6.3 (p. 95)). Lofting, especially at the old end, occurs in the extrusion direction which translates to an increased l_{plast}. This increase becomes very visible when checking the length displacement D_l between the middle point of the mantle and the volume center of the entire plastificate at half of l_{plast} (cf. Figure 4.1 (p. 64)). Length l_{plast} and D_l correlate strongly ($r = 0.88$).

While lofting, as the name suggests, is often understood as a change in height, it is important to also consider the accompanying change in length as it will influence the area covered in the mold. Lofting was observed to increase with w_f in supervised works (Löwe 2022, p. 26) as well as in literature (Rohan et al. 2014, p. 11).

Table 5.3 Plastificate properties 1. Weight m_{plast} and dimensions l_{plast} and D_l, are sorted by w_f.

$w_{f,mean}$ in %	Run order/ remark	mean m_{plast} in g	CV in %	mean l_{plast} in mm	CV in %	D_l in mm	CV in %
18.29[S]	V12	625	2	239	3	14.3	6
18.81	V13	621	3	255	1	8.2	3
19.63	V16	617	2	240	2	12.5	5
22.79	V15	615	1	209	1	3.6	2
24.89	V5	640	3	209	3	0.4	0
25.32	V9	645	1	223	1	2.9	1
30.53[S,C]	V10	671	2	276	3	20.4	7
30.93[C]	V6	671	3	289	2	25.4	9
31.19[C]	V3	654	1	269	2	20.0	7
33.50	V14	690	4	304	1	27.9	9
37.57	V2	672	2	323	2	31.4	10
39.22	V11	728	4	314	3	24.3	8
40.72	V1	734	3	349	1	31.4	9
40.76	V4	724	4	320	2	33.6	10
41.01	V17	718	1	321	2	26.8	8
57.95[S]	V7	781	2	311	2	26.8	9

[S] selected parameter set; [C] center point parameter set

5.2.3 Plastificate Density Distribution

Density measurements were conducted at the old, ρ_{old} and new, ρ_{new} half of the plastificate. Table 5.4 shows these measurements along with ρ_{mean} of each parameter set and the density gradient $\Delta\rho = \rho_{new} - \rho_{old}$ expressed as relative density increase from old to new end.

Table 5.4 Plastificate properties 2. Density ρ_{mean}, ρ_{old} and ρ_{new} are sorted by w_f. Density increase $\Delta\rho$ is given in %

$w_{f,mean}$ in %	Run order/ remark	ρ_{mean} in g/cm³	ρ_{old} in g/cm³	ρ_{new} in g/cm³	$\Delta\rho$ in %
18.29[S]	V12	0.86	0.86	0.86	0.04
18.81	V13	0.89	0.88	0.90	3.20
19.63	V16	0.87	0.88	0.87	−1.04
22.79	V15	1.06	1.04	1.08	4.30
24.89	V5	0.96	0.94	0.98	4.43
25.32	V9	1.00	0.97	1.02	5.03
30.53[S,C]	V10	0.72	0.69	0.75	8.67
30.93[C]	V6	0.71	0.70	0.72	3.47
31.19[C]	V3	0.72	0.71	0.74	5.17
33.50	V14	0.58	0.54	0.61	12.51
37.57	V2	0.59	0.57	0.61	6.63
39.22	V11	0.59	0.58	0.60	2.83
40.72	V1	0.55	0.55	0.55	−0.47
40.76	V4	0.62	0.62	0.62	0.07
41.01	V17	0.60	0.57	0.62	7.47
57.95[S]	V7	0.46	0.45	0.47	2.92

[S] selected parameter set; [C] center point parameter set

A strong negative correlation ($r = -0.86$) between ρ_{mean} and w_f is found indicating that lofting is closely related to w_f (cf. following Figure 5.5). No clear correlations for the inhomogeneity of ρ expressed by $\Delta\rho$ can be found. It is clear, however, that ρ_{new} is always larger than ρ_{old} with two exceptions at V16 and V1. This coincides with previous findings about the length displacement D_l towards the old end of the plastificate (cf. Table 5.3).

The calculated LFT density $\rho_{LFT,calc}$ was determined according to equation (5.1) with densities ρ_f and ρ_p from data sheets.

$$\rho_{LFT,calc} = \frac{\rho_p \cdot \rho_f}{w_f \cdot \rho_p + (1 - w_f) \cdot \rho_f} \tag{5.1}$$

Figure 5.5 illustrates the close connection between w_f and plastificate lofting. A lofting quotient was calculated from ρ_{mean} and $\rho_{LFT,calc}$ and is shown over w_f. At the highest w_f, ρ_{mean} is less than 30 % of $\rho_{LFT,calc}$ indicating high amounts of air in the plastificate. Selected factor combinations are highlighted again and are highly correlated to w_f together with other parameters with a $\dot{Q}^*$ between 9 and 11 (r = −0.99). Encircled in the upper left are three parameters significantly breaking out from that correlation, all of those were produced at low n_{TSE2} with low w_f and low *SME* (cf. Table 5.1 (p. 76)). Plastificates here are especially dense and closer to their $\rho_{LFT,calc}$.

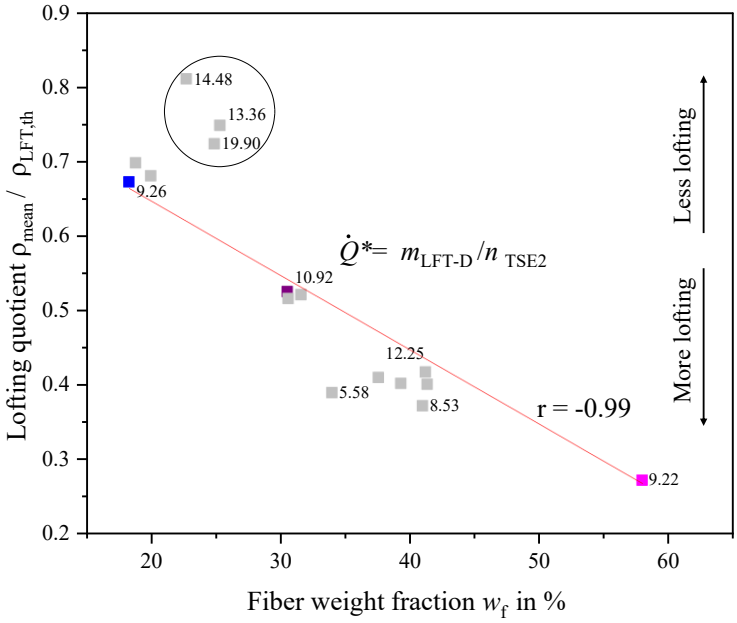

Figure 5.5 Plastificate lofting quotient over w_f. The $\dot{Q}^*$ ratio is shown next to data points. Linear correlation r = −0.99 between samples with similar $\dot{Q}^*$ ratio between 9 and 11.

5.2.4 Plastificate Fiber Length

Like samples extracted from TSE2 (cf. 5.1.4), l_f in the plastificate could not be measured as they were too long.

5.2.5 Plastificate Fiber Orientation

Carbon black was introduced into the fiber intake of TSE2 to serve as a tracer material. The fiber orientation in the plastificate is closely related to the screw channels, among others (cf. 2.5.5 (p. 21)). Figure 5.6 shows a sliced plastificate ($w_f = 25$ %) with tracer pigment. It is sliced in three parts according to the scheme shown in c) with part I representing the vertical section. While plastificates look like solid homogeneous objects they clearly have a pronounced internal structure. This structure is also more complicated than two helical coils side by side (Perez et al. 2013, p. 1120; Schreyer et al. 2022, p. 682). Knitting lines of both helical material strands deposited by the screw channels can be made out and are marked with white dashed lines for reference. For all parameter sets a similar pattern was found.

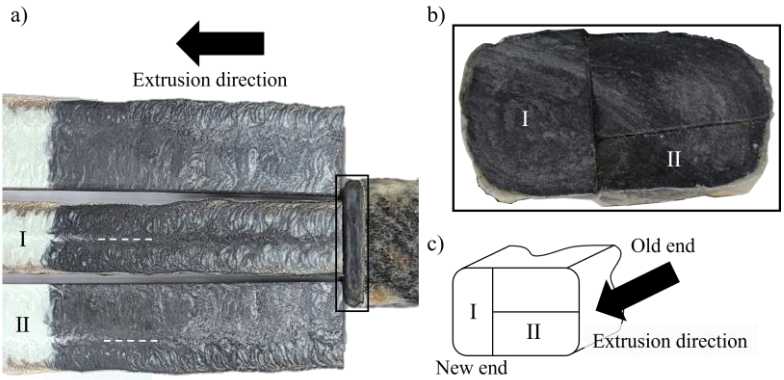

Figure 5.6 Sliced LFT-D plastificate with tracer material a). Surface of the entire plastificate b). Slicing scheme with cuts along the vertical axis I and along the mid plane II in c). Expressions of TSE screws are visible as are knit lines (dashed lines in a)).

Plastificate FO is perpendicular to the extrusion direction for all factor sets.

This was validated for one plastificate of the DoE center point with a CT scan accompanied by an evaluation of fiber orientation. This is shown in Figure 5.7 where the CT scan is overlayed by the tensor glyphs in all 12 areas characterized (brown ellipses, left). An edge section of a cut plastificate is shown on the right for reference. Scan and analysis were conducted by Juliane Blarr at the Institute of Applied Materials at Karlsruhe Institute of Technology. The orientations were determined in a structure tensor-based method, explained, and validated by Pinter et al. (Pinter et al. 2018). Tensor glyphs were plotted according to Blarr et al. (Blarr et al. 2023) based on (Barmpoutis 2010).

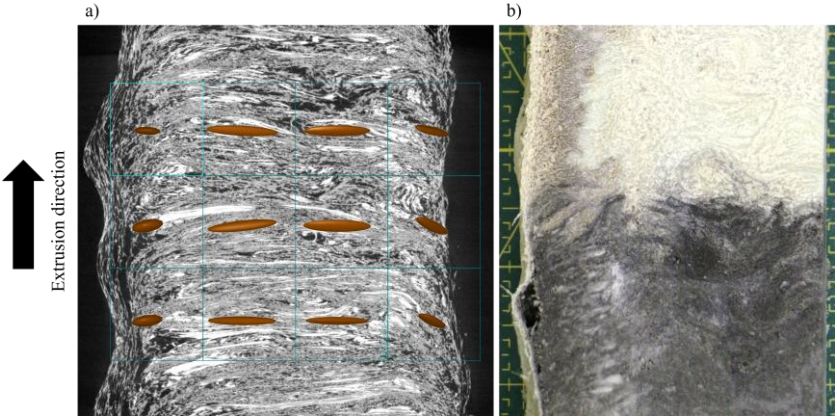

Figure 5.7 CT scan of unsliced LFT-D plastificate with fiber orientation tensors overlay a). Sliced plastificate with tracer pigment b).

These findings do, on a first glance, not agree with Tröster's measurements of a fiber orientation angle of ± 60° in a PP GF plastificate (Tröster 2004, p. 51). In previous studies with PC, a strong dependency of plastificate fiber orientation with TSE parameters, especially n_{TSE2} was found. The internal material flow was also made visible with carbon black. Material viscosities as well as the fiber structure in the plastificate, especially the length and accompanying

entanglement of the fiber, are the most likely factors here. The relationship between the plastificate and secondary processing factors like die temperature and die height were investigated by Meckes (Meckes 2024).

The fact that plastificate FO for all parameter sets are the same is fortunate, as it can be excluded as the sole reason for skewed flow-fronts and resulting FO deviations in LFT-D plates presented and discussed in the following chapter 5.3 as well as in chapter 6.3 (p. 103).

5.3 Flow-fronts in Compression Molding

Flow-fronts were characterized according to Meckes (Meckes 2024). Exemplary shown in Figure 5.8 are the digitized flow-fronts from V4 and V14 having low and high skewness s_{ff}. Shown are all six measurements (thin lines) as well as a mean curve (bold line) for every group. The mold middle is shown at x = 200 mm as well as dashed lines indicating mean $s_{ff,V14}$ = 17 % and $s_{ff,V4}$ = 1 %. Both parameter sets are in the medium w_f area.

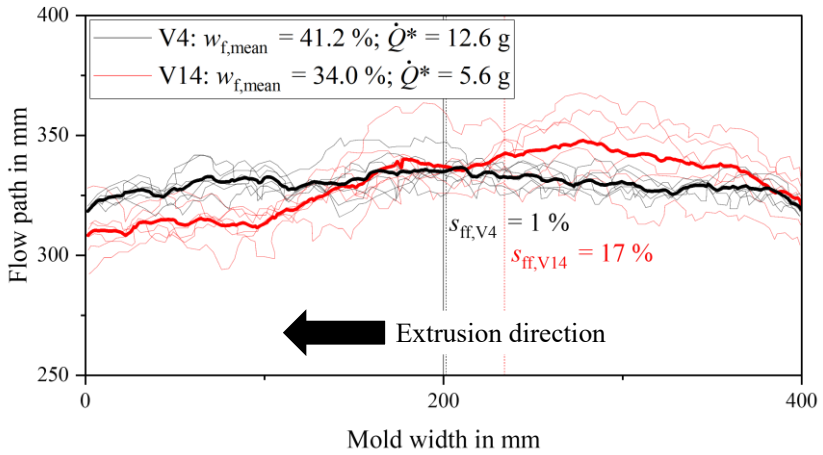

Figure 5.8 Flow-front shapes for low (black) and high (red) s_{ff}. Six curves are averaged each (bold line). Plastificate extrusion direction from right to left is given as black arrow.

Notable is the big difference between $\dot{Q}^*$ resulting from high total throughput at V4 and high n_{TSE2} at V14. While the mean values for s_{ff} speak a clear language, the deviations within data sets, from plate to plate, are very high. For V14 s_{ff} of individual plates varies between $s_{ff,V14\_F1} = -0.5$ % and $s_{ff,V14\_F4} = 26.9$ %. Exhibiting particularly bad mechanical properties, V14 is picked up again in later discussions.

Figure 5.9 exhibits s_{ff} sorted by low and high m_p (columns) and low and high n_{TSE2} (rows). Colored in every graph is low $n_{rov} = 8$ pcs (black) and high $n_{rov} = 24$ pcs (red). Selected parameter sets V7 and V12 have been marked with their respective colors. The calculated values for $w_{f,calc}$ and $\dot{Q}^*$ are given. Factor combinations shown in Figure 5.9 represent the eight edges of the FCCCD cube. This can be seen especially well in $\dot{Q}^*$ given for all parameter sets, the highest in the upper right and lowest in the lower left pair. Missing in the upper right graph is V8 as the parameter set could not be processed.

The round flow-front shape can be made out in all curves as well as in the averaged curves. The skewness is especially visible for V14 where the bulge of material is only visible after the first 100 mm of mold length (cf. Figure 5.9 lower left, black). In all cases the higher w_f variant covers less area as ρ is higher.

All flow front curves are representations of halted mold filling progression. Considering fiber orientation in suspensions during molding (cf. 2.6 (p. 23)) we assume the FO is influenced by the direction of the flow-front although the correlation is only weak (r = 0.49). At least in the outer areas of the plate the LFT-D freezes immediately upon mold contact (Tucker 2022, p. 114) and the then current FO is preserved.

As explained by Radtke, the mold is filled starting from the new end of the plastificate (Radtke 2009, p. 61). This can be seen for some of the parameter sets, especially V5 and V14.

Similar observations were reported by Scheuring after conducting PA6 CF mold filling studies with this author at ICT (Scheuring 2024, p. 198; Scheuring et al. 2024, p. 14). The displacement D_l in the plastificate and s_{ff} are weakly

correlated at r = −0.58 (cf. 5.2.2 (p. 79) and Table 5.3 (p. 81)) which is an indicator that a shifted material distribution in the plastificate is responsible for this behavior.

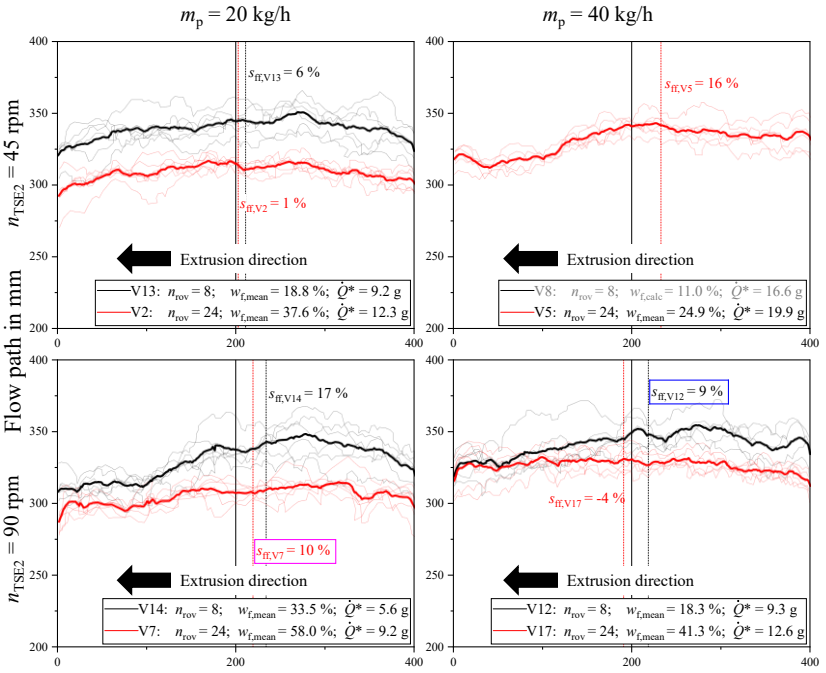

Figure 5.9 Flow-front skewness for low n_{rov} (black) and high n_{rov} (red). Plots are arranged by m_p and n_{TSE2} marking all corners of the FCCCD. Six curves are averaged each (bold line). The mold center is marked by a solid black line at x = 200 mm with s_{ff} marked as color-coded dashed lines. The extrusion direction from right to left is given as black arrow.

All s_{ff} are shown in Table 5.5, previously selected parameter sets V7, V10 and V12 have relatively similar s_{ff}. Both V7 and V12 can be referenced in Figure 5.9 (colored accordingly). In almost all cases s_{ff} skews towards the new end of

the plastificate. Sole exception is $s_{ff,V17} = -4$ % (cf. Figure 5.9 lower right, red) which has the highest $m_{LFT\text{-}D}$. Generally, s_{ff} is higher at lower w_f.

Table 5.5 Flow-front s_{ff} is given in absolute and relative numbers sorted by w_f.

$w_{f,mean}$ in %	Run order/ remark	s_{ff} in mm	s_{ff} in %
18.29[S]	V12	18.7	9
18.81	V13	11.0	6
19.63	V16	25.2	13
22.79	V15	30.0	15
24.89	V5	32.8	16
25.32	V9	26.3	13
30.53[S,C]	V10	22.6	11
30.93[C]	V6	24.9	12
31.19[C]	V3	22.7	11
33.50	V14	34.0	17
37.57	V2	2.7	1
39.22	V11	15.3	8
40.72	V1	5.5	3
40.76	V4	1.5	1
41.01	V17	−8.9	−4
57.95[S]	V7	19.3	10

[S] selected parameter set; [C] center point parameter set

6 Results: Material Development

This chapter deals with characterization results from square plates. Results are sorted by w_f where applicable for easy comparability to other works and to serve as reference. First, the microstructure is discussed followed by mechanical properties. For all plots depicting mechanical properties in the following sections, w_f is differentiated between charge, $w_{f,C}$, and flow area, $w_{f,F}$. Three parameter sets, previously selected, are further highlighted (color coded) for detailed discussion in this chapter. They represent lowest $w_{f,mean}$ = 18.29 % and highest $w_{f,mean}$ = 57.95 % as well as the center point of the DoE, $w_{f,mean}$ = 30.53 %.

All underlying testing data is found in the Appendix (p. 169 ff.). The connection to processing parameters and process development is discussed in chapter 7 (p. 121 ff.)

6.1 Microstructure: Fiber Fraction

Of high interest for material development of LFT-D is w_f, measured at three points on five or six plates per trial point via TGA. Table 6.1 shows mean w_f values for charge (C), intermediate charge-flow (C-F) and flow (F) area as well as an overall $w_{f,mean}$ calculated from all measurements of that trial point. The CV of $w_{f,C}$, $w_{f,C\text{-}F}$ and $w_{f,F}$ as well as $w_{f,mean}$ was calculated and are shown as percentages. Table 6.1 is sorted by $w_{f,mean}$ from lowest to highest. It is apparent that CV within the sample group is highest for lower $w_{f,mean}$ and drops to low single digit percentages at high $w_{f,mean}$.

Table 6.1 TGA results sorted by $w_{f,mean}$. Columns represent mean w_f and respective CV for three areas C, C-F and F.

Run order	$w_{f,mean}$ in %	CV in %	$w_{f,C}$ in %	CV in %	$w_{f,C-F}$ in %	CV in %	$w_{f,F}$ in %	CV in %
V12[S]	18.29	16	16.13	10	17.80	14	20.93	13
V13	18.81	8	17.72	10	19.72	6	19.05	5
V16	19.63	11	18.50	10	18.72	9	21.68	6
V15	22.79	9	20.08	4	22.90	5	25.40	7
V5	24.89	6	23.68	3	24.63	4	26.37	5
V9	25.55	10	22.78	5	25.40	5	28.46	3
V10[S,C]	30.53	9	27.14	1	30.96	4	33.48	2
V6[C]	30.93	11	28.04	3	30.30	8	34.46	8
V3[C]	31.19	13	26.85	5	31.62	7	35.12	7
V14	33.50	7	32.20	8	33.38	4	34.92	8
V2	37.57	9	33.72	3	37.52	3	41.47	3
V11	39.22	7	37.64	6	38.02	3	42.00	6
V1	40.72	7	38.00	5	40.76	5	43.40	5
V4	40.76	7	37.18	2	40.90	2	44.20	2
V17	41.01	6	38.40	2	40.74	2	43.85	4
V7[S]	57.95	2	57.08	1	57.90	1	58.85	1

[S] selected parameter set; [C] center point parameter set

The spread of w_f within sample groups is relevant as it might partially explain the deviation of mechanical properties between plates. A visual representation of this is given in Figure 6.1 and Figure 6.2.

Figure 6.1 visualizes the normal distributions of all TGA samples. The peak of each distribution marks $w_{f,mean}$ from Table 6.1 with the dashes underneath (rug) representing all individual measurements. Distributions are, disregarding exceptions, equally broad towards higher w_f, an observation in line with decreasing CV listed in Table 6.1. The relative deviation is lower for higher w_f. One exception is notably at highest $w_{f,mean} = 57.95$ % where the distribution is

especially tight (CV = 1 %). For the other two selected parameter sets the CV around $w_{f,mean}$ is 16 % ($w_{f,mean}$ = 18.29 %) and 9 % ($w_{f,mean}$ = 30.53 %).

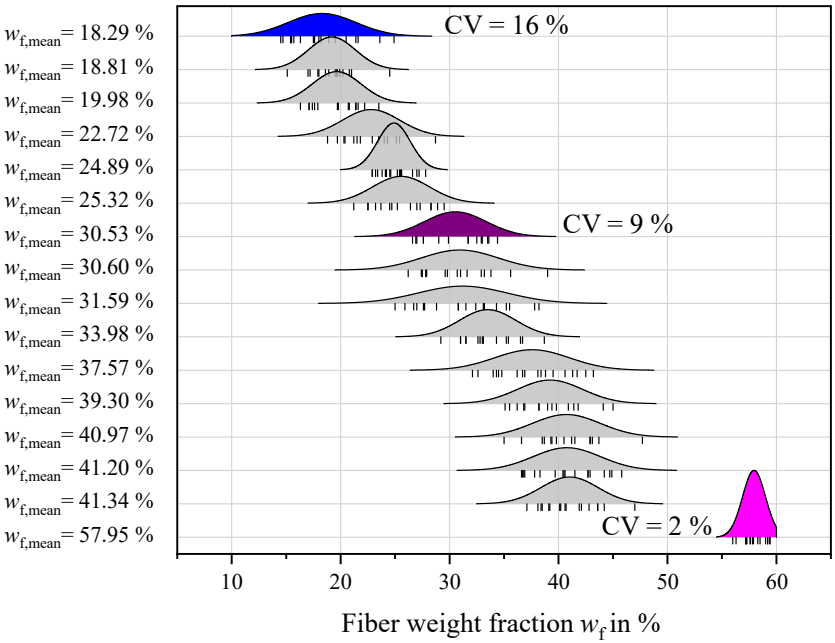

Figure 6.1 Mean fiber fractions $w_{f,mean}$ with associated normal distributions. Rugs (black lines) under each normal distribution indicate single measured values.

Calculating $w_{f,mean}$ values in this fashion, across all TGA samples from C, C-F and F areas, reduces information regarding fiber-migration behavior. It represents the mean fiber content output of the LFT-D line.

Figure 6.2 expands upon Figure 6.1 by separating $w_{f,C}$ and $w_{f,F}$ in adjacent pairs marked on the ordinate by _C and _F. Respective $w_{f,C}$ and $w_{f,F}$ are shown with their normal distribution and rug. The sampling scheme with highlighted sampling positions is given in the top right corner of the plot for reference. Roughly half of trials show clearly separated $w_{f,C}$ and $w_{f,F}$ in tight distributions. The other

half comprises a substantial spread of w_f from the same sampling location indicated by flat, drawn-out distributions. The selected parameter sets are a mixture ranging from CV_C = 10 % and CV_F = 13 % at low $w_{f,mean}$ = 18.29 % to 1 % to 2 % for $w_{f,mean}$ = 30.53 % and $w_{f,mean}$ = 57.95 %. Discussing mechanical properties further, the differentiation between C and F areas is made and respective $w_{f,C}$ and $w_{f,F}$ are calculated to account for the w_f aspect of microstructure.

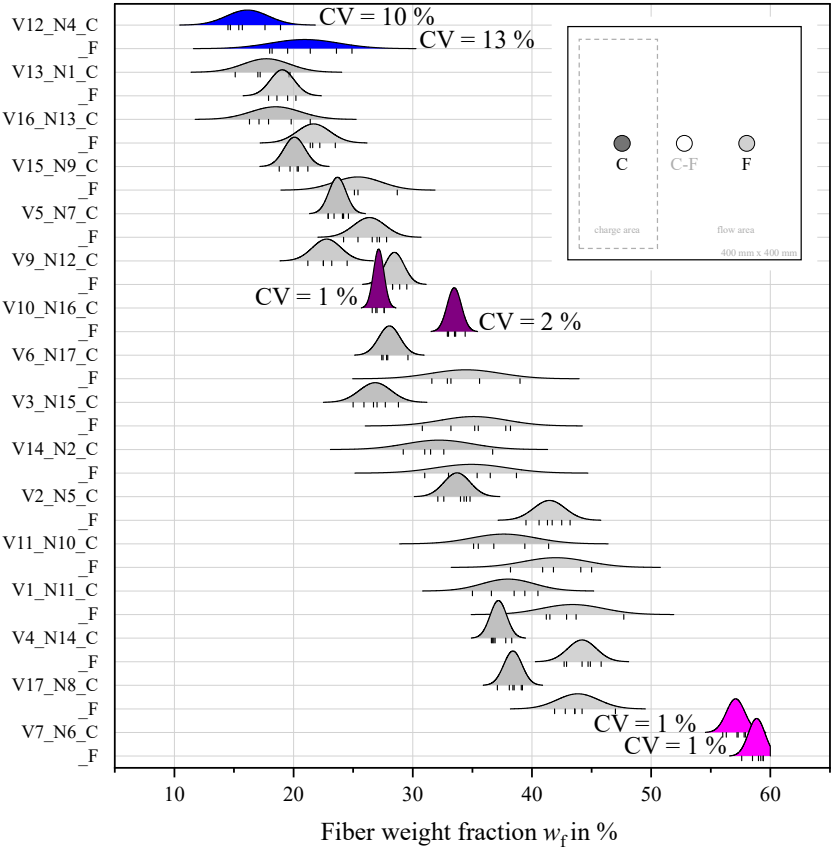

Figure 6.2 Mean fiber fractions $w_{f,mean}$ separated by C and F area. Rugs (black lines) under each normal distribution indicate all measured values.

Detailed investigations into the fiber fraction distribution

Five plates of the center point were characterized in detail (Meckes 2024). These results give an indication of what precision to expect from the LFT-D process output (variation from plate to plate). Also, $w_{f,C}$ and $w_{f,F}$ is clearly different. These results indicate to what extent fiber migration plays a role (variation within plates). Figure 6.3 illustrates mean w_f values and SD from five plates (n = 5) that were segmented into 25, 80 mm by 80 mm, squares. Extrusion as well as flow directions are analogous to all other representations in this work as is the plastificate charge area in the left part of the plate. The initial position of the plastificate is recognized, covering six squares on the left edge of the plot oriented around the horizontal centerline (white frame). Plastificate length in this case is 278 mm (cf. Table 5.3 (p. 81) for plastificate dimensions).

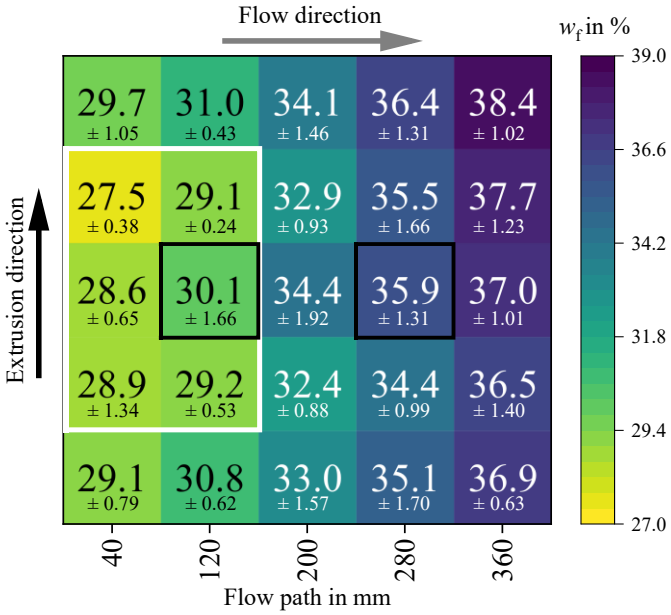

Figure 6.3 Fiber fraction $w_{f,mean}$ and SD given in 25 segments of five entire plates each. Plastificate charge position is marked with a white frame. TGA sampling areas are marked with black frames. Modified from (Schelleis et al. 2025a, p. 472)

Total w_f from plate-to-plate ranges between $w_{f,plate}$ = 32.8 % and 33.4 % (SD = 0.6 %*pt*. (CV = 1.8 %)), indicating the baseline precision of the LFT-D line. Across the flow path (grey arrow), from 0 mm to 400 mm, w_f increases column by column from 28.8 % to 37.3 % with an overall $w_{f,mean}$ = 33.0 %. Line by line, in extrusion direction (black arrow), no such effect can be seen and $w_{f,mean}$ ranges from 32.3 % to 33.9 %. Standard deviations are smaller in the C area (black font).

Examination of w_f in the areas where mechanical samples were taken, four squares in the lower left for sample group C and four squares in the upper right for sample group F, reveals that in the F area the w_f values are higher than in the rest of the column. While not significant at a level of $\alpha = 0.05$, the difference from $w_{f,F}$ = 35.9 % is still noteworthy as it certainly adds to the overall deviations. If one were to draw lines of constant w_f according to these measurements, especially in the F area they would be skewed like the flow-front.

Calculating SD for all squares results in SD_{min} = 0.24 %*pt*. (CV = 0.7 %) to SD_{max} = 1.92 %*pt*. (16 %). Which is lower than most of the deviations reported in Table 6.1. For further comparison, the areas where the TGA samples for the determination of $w_{f,C}$ and $w_{f,F}$ were taken are marked by black frames in Figure 6.3. Here, SD is 1.66 %*pt*. (5.5 %) and 1.31 %*pt*. (3.6 %) for detailed measurements and 0.81 %*pt*. (2.9 %) and 1.9 %*pt*. (5.5 %) for the TGA measurements averaged across all repetitions of the center point (cf. Table 6.1 (p. 92)). Especially this reference square (black frame) exhibits high SD compared to other squares in the C area (black font) or the plastificate placement area (white frame).

Figure 6.4 shows a similar experiment with plates produced using the same TSE settings (center point DoE). The TSE2 die was kept at constant height during the DoE study. In this experiment this height was varied to produce different plastificate lengths l_{plast}. In this case l_{plast} was changed from 280 mm to 360 mm by closing the die from 38 mm to 24 mm. Again, the plastificate placement area, marked white, is clearly visible as is w_f progression across the flow path in flow direction (grey arrow). Fiber migration can be observed as well towards the mold walls in and against the extrusion direction (black arrow).

Fiber migration is influenced by the length of the plastificate as the C area is increased in size. From just changing the die height, w_f at the sample position can be manipulated, as shown in Table 6.2.

Table 6.2 Fiber fraction $w_{f,mean}$ and transverse deviations in the sampling areas C and F for different plastificate lengths indicated as a) and b) in reference to Figure 6.4.

Plastificate length	$w_{f,mean}$	CV	C area transverse deviation	F area transverse deviation
	in %	in %	in %	in %
a) 280 mm	33.1	7.9	2.3	0.3
b) 360 mm	32.9	9.2	2.4	2.6

The overall fiber content $w_{f,mean}$ is the same for both plastificate lengths while CV is lower for the short plastificate (open die). The difference in w_f from the TGA sampling spots (black frames in Figure 6.4) to the entire columns, two (C area) and four (F area), where the mechanical samples would be located, is also determined. This can be described as a deviation transverse to the flow direction. This deviation is evenly distributed at around 2.4 % except in the F area molded from a short plastificate. Here the TGA sampling location is especially representative regarding w_f at the actual sampling location with a transverse deviation of only 0.3 %.

This shows how plastificate length is a factor in the development of the microstructure. Plastificate lengths were measured for all parameter sets and can be inspected in Table 5.3 (p. 81). Further discussion on the topic of fiber content and fiber migration is conducted in 7.2.1 (p. 123) and 7.2.2 (p. 126).

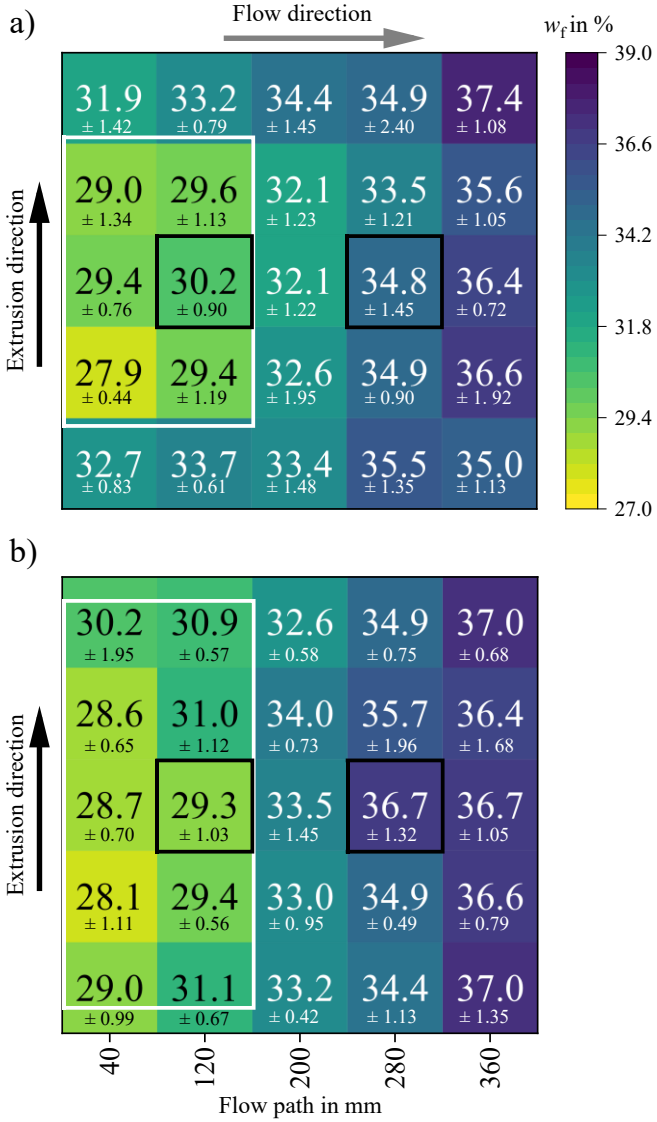

Figure 6.4 Fiber fraction $w_{f,mean}$ given in 25 segments with four samples per segment. Plasticate position is marked with a white frame. Plasticate length is varied from 280 mm, a) to 360 mm, b). Modified from (Meckes 2024, p. 66).

6.2 Microstructure: Fiber Length

Fiber lengths were measured via FASEP in select C, C-F and F samples from TGA. The results are shown as distributions over these three areas, marking 200 mm of flow path (cf. scheme in Figure 4.2 (p. 66)). Figure 6.5 shows l_n sorted by w_f in ascending order. A general tendency of l_n to decrease with increasing w_f is seen. The SD as well as the CV is highest at low to medium w_f range. While $l_{n,mean}$ is significantly different across the entire spread of $w_{f,mean}$, a difference in l_n for similar w_f cannot be observed. No influence of n_{TSE2}, or other factor, can be detected. All results are also given in Table A.2 (p. 170).

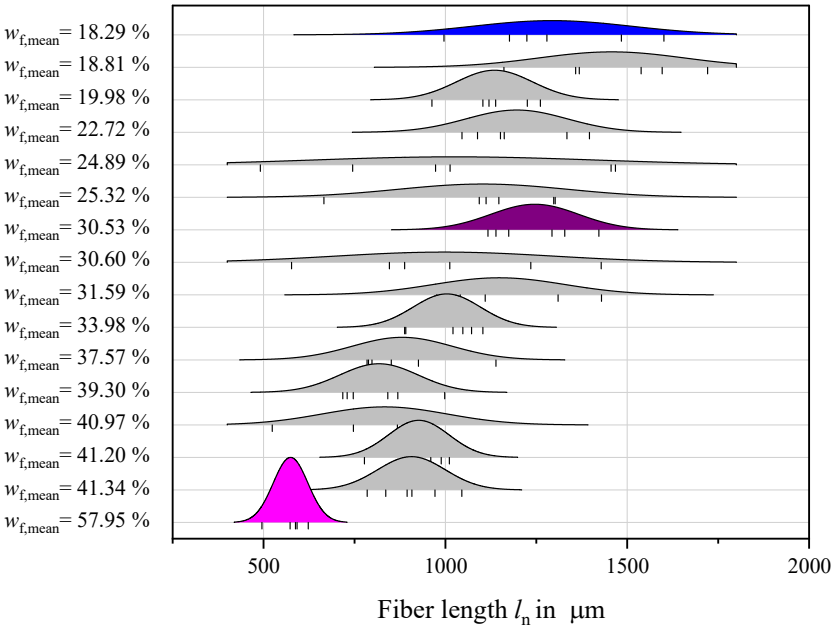

Figure 6.5 Fiber length l_n measurements in µm sorted by w_f visualized as normal distributions.

Fiber length measurements are depicted in nine histograms in Figure 6.6. Columns represent the flow path from C (left) to F (right). The rows represent

selected parameter sets at low and high w_f as well as the center point. Relative frequency is shown on the left ordinate of every histogram. Shorter fibers are more frequent towards the end of the flow path in column F. Shorter fibers are more frequent at higher w_f due to higher fiber-fiber interaction. The function of cumulative percentage (right ordinate) does change with w_f, not with flow path. This means that, while shorter fibers are found towards the F area, so are individual longer fibers. This is reflected in increasing l_w over the flow path. This is strongest for highest w_f where l_w increases from 1622 µm to 5011 µm (box in every plot and dotted lines demarking l_n and l_w). This is in line with observations from the state of the art (cf. 2.6.3 (p. 28)). Various bin sizes were tested; the shape of the curves does not change. No multi-modal distribution patterns can be seen.

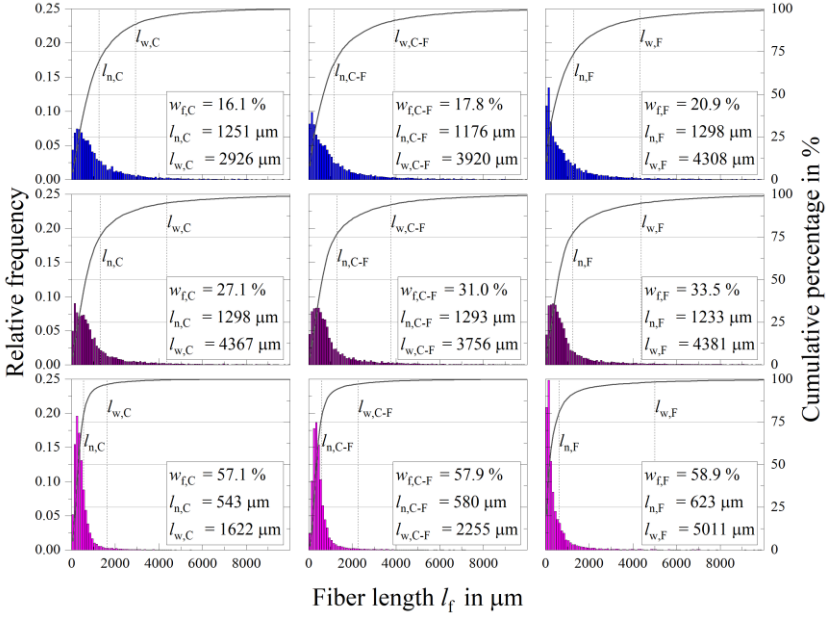

Figure 6.6 Histograms (bin size 100 µm) of l_f measurements for select parameter sets in order of ascending w_f (rows). Columns mark the flow path from C (left) to F (right).

Challenges of Fiber Length Measurement

Managing fiber attrition is a core challenge in processing FRPs (cf. 2.4 (p. 13)). To quantify the quality feature, l_f, the only commercially available characterization FASEP was used (cf. 2.2.2 (p. 8)).

It was planned to sample l_f in TSE2 as well as the plastificate to describe fiber attrition across the entire processing length. These samples comprise essentially fiber rovings in shape and length and could not be measured with FASEP (cf. 5.1.4 and 5.2.4). Similar problems were encountered by Rohde-Tibitanzl who failed trying to sample directly from the screw positions (Rohde-Tibitanzl 2015, p. 111) as did Hümbert (Hümbert 2016, p. 47).

As with w_f before, plates from all parameter sets were sampled to be FASEP characterized along the flow path in the C, C-F and F area (cf. sampling scheme in Figure 4.2 (p. 66)). All measurements overlap from lowest to highest w_f (cf. Figure 6.5 (p. 99)). From these results no influence of factors can be recognized. While l_f was reported across a broad spectrum in literature (cf. Table 2.5 (p. 38)), most results from semi-automated sampling schemes such as FASEP are in line with these newest results.

The discrepancy between measured l_f and simple observation is staggering. Following Figure 6.7 shows in detail the fiber skeleton of a plate segment where the polymer matrix was burned off. It is an 80 mm by 80 mm square from the end of the flow path. The fiber content of this square is $w_f = 37.0$ %, higher than $w_{f,mean}$ for this parameter set (cf. fiber migration in Figure 6.3 (p. 95)). According to the underlying data of Figure 6.5, we expect $l_n = 1.13$ µm and $l_w = 3.92$ µm (cf. Table A.2 (p. 170)). Referring to the scale shown in Figure 6.7, a mismatch becomes apparent. While there is a fraction of fiber dust, an even larger fraction, especially by weight, of fibers in the double-digit mm range is visible. This fiber skeleton forms a coherent, densely packed tangle of fibers.

Figure 6.7 Fiber skeleton of a burned plate segment from the center point ($w_{f,mean}$ = 33 %) towards the end of the flow path.

For LFT-D the employed FASEP method is insufficient to reflect the actual fiber lengths. This could be due to a combination of factors. The sample size (Ø = 24 mm) being too close to the actual fiber length, damaging the fibers in the sampling process. Sub-sampling is done in two steps, the first is done by hand, according to literature this should be biased towards longer fiber lengths (Nguyen et al. 2008). The second step, dilution of the sample, could affect fiber length either by breaking the fiber or inadvertently selecting the shorter fractions of the sample. Previous FASEP measurements of LFT-D materials must not be adopted uncritically (cf. Table 2.5 (p. 38)).

Any criteria of what constitutes an LFT material are met by a large margin.

6.3 Microstructure: Fiber Orientation

Figure 6.8 shows polar plots of the tensile disc characterization in the flow area. Results comprise pairs of disc orientation angle ϕ and maximum force F_{max} at ε = 0.02 %. Two discs were tested for all parameter sets (shown in slightly transparent color in Figure 6.8). The complete results from tensile disc characterization are shown in Table 6.3.

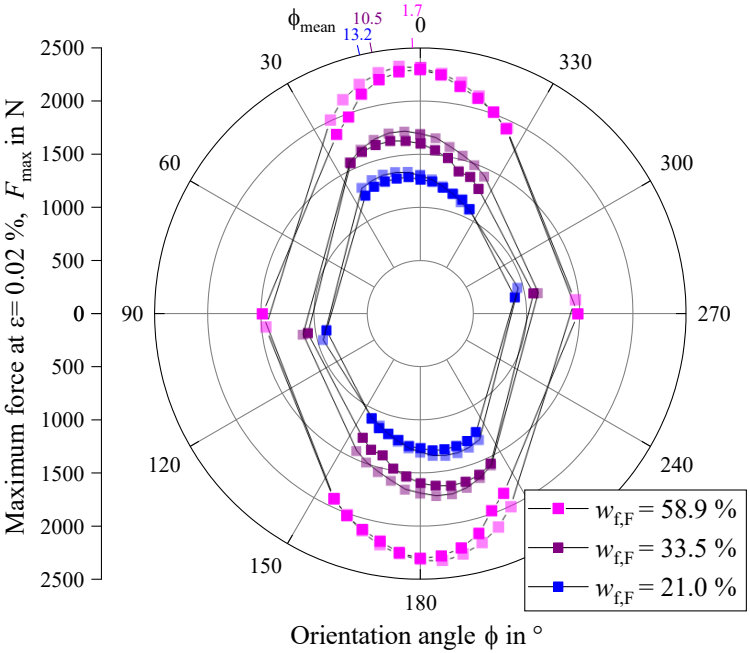

Figure 6.8 Polar plots of tensile disc characterization results of the flow area of select parameter sets. Higher ϕ for lower w_f are noted on top of the polar plot.

Resulting F_{max} increases with w_f (r = 0.99). While selected parameter sets in Figure 6.8 do not differ significantly in anisotropy ratio, the axis ratio R_a generally decreases with w_f (r = −0.64) (cf. Table 6.3). This means that the

difference between 0° and 90° becomes more pronounced with increasing w_f. However, mechanical properties of the unreinforced PA6, predominantly found in 90° stay the same while the samples in 0° perform higher with w_f so this behavior should be expected aside from fiber orientation considerations. Despite this, the reinforcing effect in 90° is very much present with $F_{90°}$ more than doubling from lowest to highest w_f.

Table 6.3 Results from tensile disc characterizations F_{max}, R_a and φ_v sorted by $w_{f,mean}$.

$w_{f,mean}$ in %	Run order/ remarks	F_{max} ($\varepsilon = 0.02$) in N	Axis ratio R_a	φ_v in °
18.29[S]	V12	1320	0.70	13.2
18.81	V13	1353	0.77	15.8
19.63	V16	1349	0.70	12.6
22.79	V15	1507	0.65	5.3
24.89	V5	1541	0.67	17.0
25.32	V9	1499	0.66	6.5
30.53[S,C]	V10	1679	0.65	10.5
30.93[C]	V6	1691	0.67	10.0
31.19[C]	V3	1649	0.67	4.9
33.50	V14	1659	0.64	17.2
37.57	V2	1884	0.64	6.1
39.22	V11	1952	0.67	10.7
40.72	V1	1948	0.68	7.4
40.76	V4	1982	0.65	6.7
41.01	V17	1987	0.59	4.2
57.95[S]	V7	2310	0.64	1.7

[S] selected parameter set; [C] center point parameter set

A similar progression of the axis ratio was found for PP GF LFT-D although the value range is bigger from $R_a = 0.8$ (PP GF10) to $R_a = 0.6$ (PP GF40 to

GF60) (Tröster 2004, p. 88). At PP GF30 Radtke found a similar R_a (Radtke 2009, p. 45).

The φ_v can be determined in correlation to F_{max} (cf. 2.3.1 (p. 11) and 0 (p. 13)). It was determined according to Meckes (Meckes 2024) (cf. 3.4.7 (p. 58)). Each φ_v is indicated at the top of their associated polar plots in Figure 6.8. It is decreasing with w_f from 13.2° ($w_{f,F}$ = 21.0 %) to 1.7° ($w_{f,F}$ = 58.9 %). This is in contrast to Tröster's findings where he reported φ_v to be around 12° for PP GF10 to GF30 and between 17.2° and 20.1° for PP GF40 to GF60 (Tröster 2004, p. 87).

A high φ_v deviation (between 3.7° and 10°) was found between plates (cf. 3.4.7 (p. 58)) and must be considered in this discussion as results can only serve as general indicators. Sample preparation and testing of tensile discs, while affordable compared to other methods, is still resource-consuming.

6.4 Mechanical Properties: Tensile

Young's modulus E is presented over w_f in Figure 6.9. The underlying data is presented in Table A.3 (p. 171) and Table A.4 (p. 172) in the Appendix. All samples have been cut from the 0° flow direction and were taken from charge (squares) and flow area (triangles) (cf. cutting schemes in 4.4.3 (p. 65)). Select pairs were given the same colors. Linear fit curves for C and F results together with their respective Pearson coefficients are given (red lines) and nearly perfect linear correlations (r = 0.99) between w_f and E are found. Fit curves intersect at ~ w_f = 35 % but have a similar gradient.

Despite substantial Δw_f, predominantly at low w_f, shown on top of the plot for select parameter sets, E does not significantly (p = 0.056 and p = 0.027, N = 6) increase from C to F for all but the highest w_f (ΔE shown to the right of the plot). While Δw_f is low at high w_f, ΔE is significant (p = 0.018, N = 6), this could be because of the rough surfaces in the C area. Such defects can initiate failure.

Corrected for w_f along curves of linear fit tensile stiffness E_C and E_F would effectively be the same. The CV does increase with w_f from CV = 1 % to CV = 11 % with no discernible differences between C and F area.

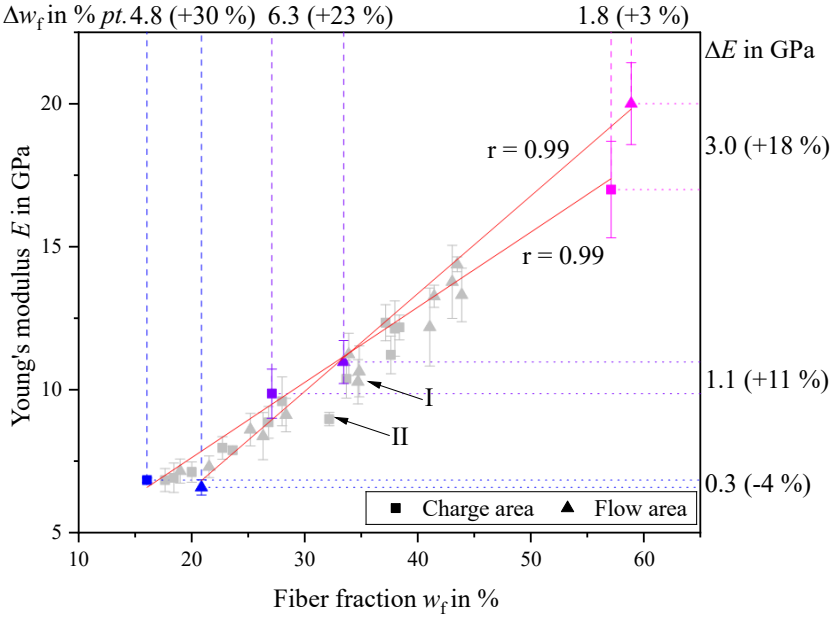

Figure 6.9 Young's modulus E in 0° direction for all sample groups sorted by w_f in C (squares) and F (triangles) area. Every pair of groups is colored the same. Curves of linear fit highlight the correlation between E and w_f.

From earlier investigations into LFT-D materials, the existence of a shell layer in the C area is known (cf. micrograph in Figure 2.8 (p. 26)), where fibers are oriented in extrusion direction and thus 90° to testing direction (cf. sampling scheme in Figure 4.2 (p. 66)). This shell layer does not influence tensile properties as it is small in relation to the total sample height.

The φ_v deviations in the F area could play a significant role here, there are F area tensile results with lower E at higher $w_{f,F}$. While smaller φ_v do not affect

E, Scheuring reported a significant decrease of E towards $\varphi_v = 22.5°$ (Scheuring 2024, p. 112). For both F area results close to the select center point in Figure 6.9 (marked I) conflicting φ_v deviations, 4.9° as well as 17.2°, are measured. In both cases E_{mean} is below average considering the linear relationship with w_f. At lowest w_f, between 15 % and 20 %, $E_{C,mean}$ and $E_{F,mean}$ are similar. For lowest $w_{f,mean} = 18.29$ % (blue) an increase of $\Delta w_f = +30$ % even decreases E_{mean} from C to F by -4 %. The associated φ_v are between 12.6° and 15.8° (cf. Table 6.3 (p. 104)). At highest w_f, where C and F are significantly different ($p = 0.018$, $N = 6$), the lowest $\varphi_v = 1.7°$ is found.

One result from the C area, parameter set V14 at $w_{f,C} = 32.20$ %, performed particularly poorly (marked II). Accompanying E_F is part of the previously discussed group I. The highest $\varphi_v = 17.2°$ was measured here. The set is located on one corner of the parameter space where high n_{TSE2} and low m_p and n_{rov} result in the lowest $\dot{Q}^*$ ratio by far (cf. Table 5.1 (p. 76)). The connection between low $\dot{Q}^*$, high $\Delta\rho$ and high s_{ff} leading to high φ_v and low mechanical properties will be part of an overarching discussion in chapter 7 as multiple characterization results are involved.

Shown in Figure 6.10 is the tensile strength σ_B at break which coincides with the maximum tensile strength σ_M for material behavior of PA6 matrix systems (Grellmann and Seidler 2022, p. 114). The underlying data is presented in Table A.5 (p. 173) and Table A.6 (p. 174) in the Appendix. Here, the increase in properties between C and F is significant for low and medium w_f at select parameter sets ($p = 0.0001$ and $p = 0.001$, $N = 6$). It is borderline not significant ($p = 0.0512$, $N = 6$) for the highest w_f when considering the obviously different CV of both sample groups (Welch correction).

The difference between C and F is highest for low w_f and does taper down to around 15 % for medium and high $w_f > 35$ % ($\Delta\sigma$ shown on the right side of the plot). While the curves of linear fit behave similarly to Figure 6.9 crossing at $w_f = 43$ %, a group of parameter sets noticeably breaks out from this pattern (V1, V4 and V17, marked I). Above $w_f = 40$ %, values for σ_F are higher than the correlation would predict drawing close to σ_C for $w_{f,C} = 57.1$ %. The factors n_{rov} and n_{TSE2} are on medium to high setting here while m_p is varied across all levels.

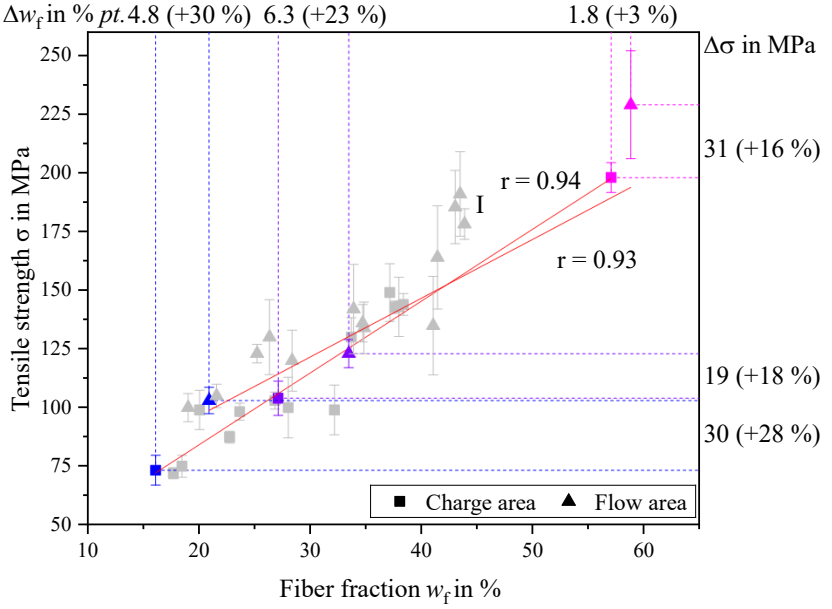

Figure 6.10 Tensile strength σ in 0° direction for all sample groups sorted by w_f in C (squares) and F (triangles) area. Every pair of groups is colored the same. Curves of linear fit for C (lower curve) and F (upper curve)

Plastificate Δρ is non-existent or low and φ_v is between 4.2° and 7.4° (cf. density gradient in Table 5.4 (p. 82) and FO deviations in Table 6.3 (p. 104)).

Standard deviations do increase with w_f with particularly broad distributions for σ_F above $w_f = 40$ %. CV, however, is highest around the center point and medium w_f from 24.89 % to 33.50 %.

Tröster reported that σ for PP GF50 to GF60 plateaued at around 116 MPa (Tröster 2004, p. 76). Similar behavior was reported for PC GF LFT-D where increasing w_f from 20 % to 40 % only yielded an increase in σ_F from 120 MPa to 137 MPa effectively decreasing specific properties (Schelleis et al. 2023a, p. 8).

Specific tensile properties E/ρ and σ/ρ of PA6 GF LFT-D keep steadily increasing. Both are calculated for reported as well as results generated in this work and shown in Figure 6.11. This way of presentation is optimized for finding the lightweight material choice when looking at pure tensile loading of a beam. While weight minimization is one of the key criteria so are material costs. Here, the PA6 GF materials presented have a good overlap with low CF reinforced PA6 systems (grey circles).

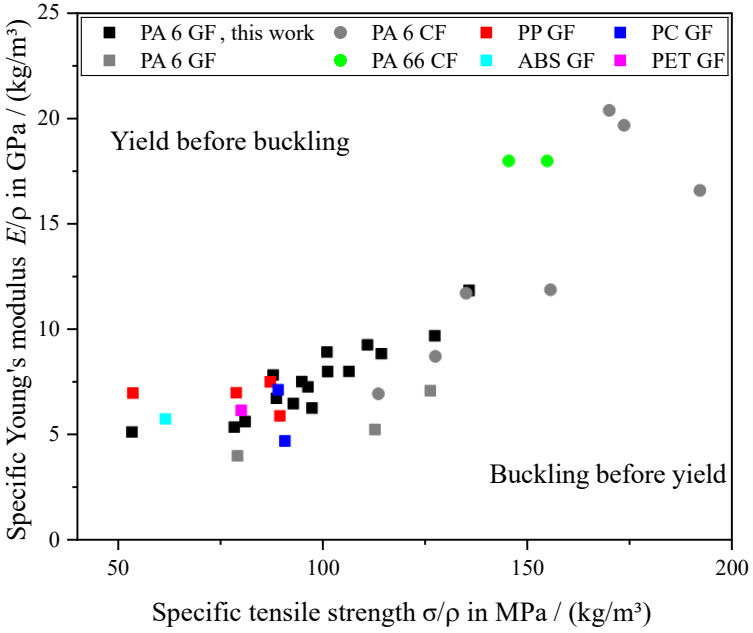

Figure 6.11 Specific tensile properties E/ρ and σ/ρ for the results of this work (black squares) compared to reported LFT-D properties from the state of the art.

Please note that while more mechanical results for LFT-D material combinations exist, the pairs of E and σ required for the figure are not consequently reported. For a more complete picture the Table 2.6 (p. 40) should be consulted as well.

Stress strain curves

Figure 6.12 shows tensile stress-strain curves for selected parameters exhibiting ductile deformation behavior typical for PA6 (Grellmann and Seidler 2022, p. 113). Samples remain in the linear-elastic region until they break (Grellmann and Seidler 2022, p. 119).

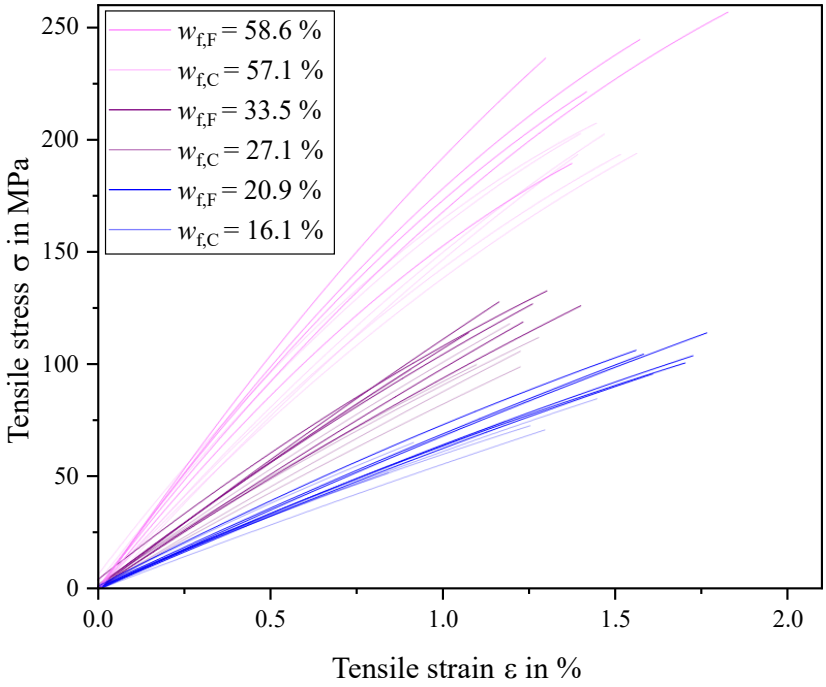

Figure 6.12 Stress-strain curves for select parameter sets. Lighter colored curves are from samples in the charge area.

While samples from C test lower than F in general, the overlap observed in E and σ (cf. Figure 6.9 and Figure 6.10) and w_f (cf. Figure 6.2 (p. 94)) is mirrored here. This overlap in the scattering ranges was also observed for PA6 GF41 as well as PA6 CF33 by Scheuring (Scheuring 2024, p. 114).

6.4.1 Inspection of Selected Fracture Patterns

All tensile samples have been visually controlled after testing. Groups of F area samples for selected parameters are shown in Figure 6.13 sorted by ascending w_f from a) to c).

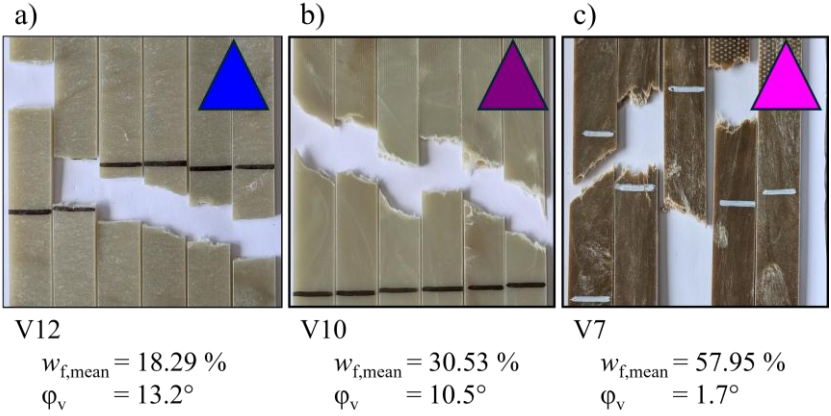

Figure 6.13 Fracture patterns of tensile samples from the F area of select parameter sets V12, V10 and V7 sorted by w_f. FO deviation φ_v is given for reference.

Special attention is given to fracturing behavior as fracture shape is indicative of fiber orientation in the sample. During tensile testing, a shear force occurs oriented less than 45° to the surface normal direction (Grellmann and Seidler 2022, p. 108). An inclined fracture surface hints towards a shear failure attributed to matrix material.

The fracture direction in Figure 6.13 a) is flat, this can be attributed to low w_f where the polymer dominates also in load direction independently of the fiber orientation (φ_v = 13.2° cf. Table 6.3 (p. 104)). A clear directionality can be seen with samples in b) where all but one fractured in a +45° angle. Fracture patterns for V7 in c) are not as clearly defined but predominantly perpendicular

to the load direction. Fracture surfaces, especially second and fourth samples, are irregular and hint at heterogeneous microstructure.

6.4.2 Distribution of Tensile Properties

To gain insight into general fluctuations in LFT-D compression molding five plates from the DoE center point were tensile tested across the plate width (cf. scheme in Figure 4.3 (p. 67)). These results are presented in Figure 6.14.

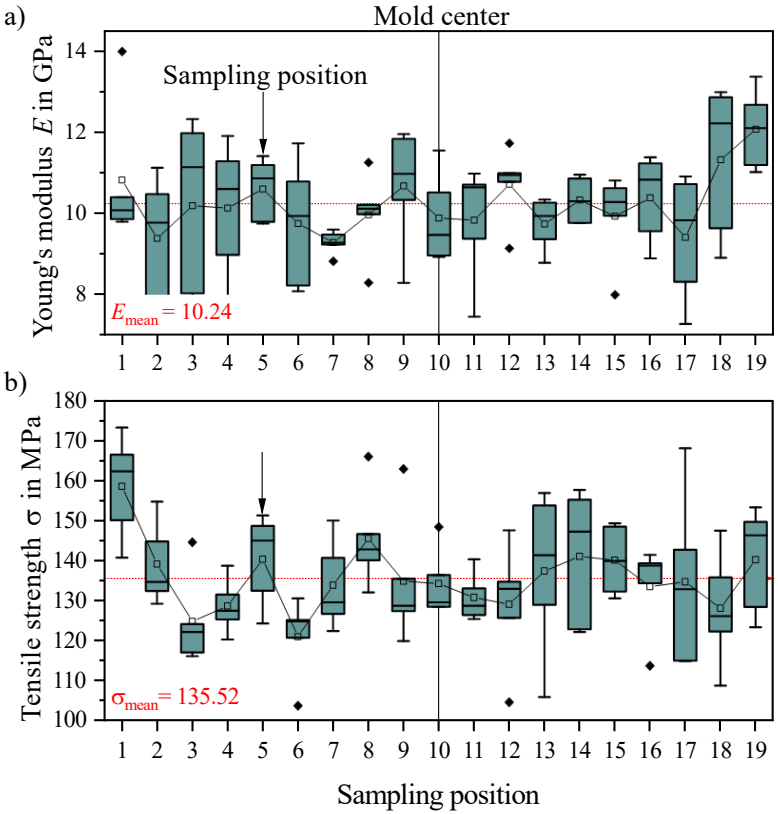

Figure 6.14 E a) and σ b) across plate width. Squares mark the mean value of five samples per position. E_{mean} and σ_{mean} for all samples are given (dashed red lines).

Considering all samples from σ_{min} = 103.7 MPa to σ_{max} = 173.1 MPa with σ_{mean} = 135.5 MPa (*SD* = 14.5 MPa) and E_{min} = 7.3 GPa to E_{max} = 14.0 GPa with E_{mean} = 10.2 GPa (*SD* = 1.4 GPa), a wide range becomes apparent.

Values for E_{mean} and σ_{mean} samples are marked by red dashed lines in a) and b). The standard tensile sampling position, used for all other tensile samples, is marked with an arrow at position 5. Tensile properties at the standard position exceed mean values by 3.5 % (*E*) and 3.4 % (σ). Plate to plate deviations at position 5 are consistently lower than overall deviations (7 % vs. 13 % for *E* and 8 % vs. 10 % for σ).

For σ, an increase in variability with sampling position can be seen. Samples taken from the new end of the plate, position 10 and up (cf. Figure 4.3 (p. 67)), have a bigger IQR concerning σ. For *E* this applies to samples especially towards the plate edges 2-4 and 16-18. But not the very outer samples 1 and 19.

The fracture angle θ was measured for all tensile samples. In Figure 6.15 a) the mean values for five samples per position are given. Fracture patterns are not distributed symmetrically across the plate. Most samples fracture in a positive angle $\theta > 0°$. Only from sampling position 15 onwards do most samples fracture in $\theta < 0°$. The standard tensile sampling position 5 is marked with an arrow. Four out of five samples fractured between $\theta = 37°$ and $\theta = 50°$. In the lower part b) of Figure 6.15 the fractures from one plate are shown. Samples 2 and 14 fractured in the cropped lower part of the picture. Additionally, coherent fractures across multiple samples can be seen (5-7; 11-13; 16-18). Large scale microstructure defects could be the reason for this, matching general dimensions of fiber bundles observed and discussed in 6.2 (p. 99). Connecting the mean values of θ a curve emerges which is reminiscent of the general shape of a skewed flow-front presented in chapter 5.3 (p. 86) (cf. Figure 5.9 (p. 88)).

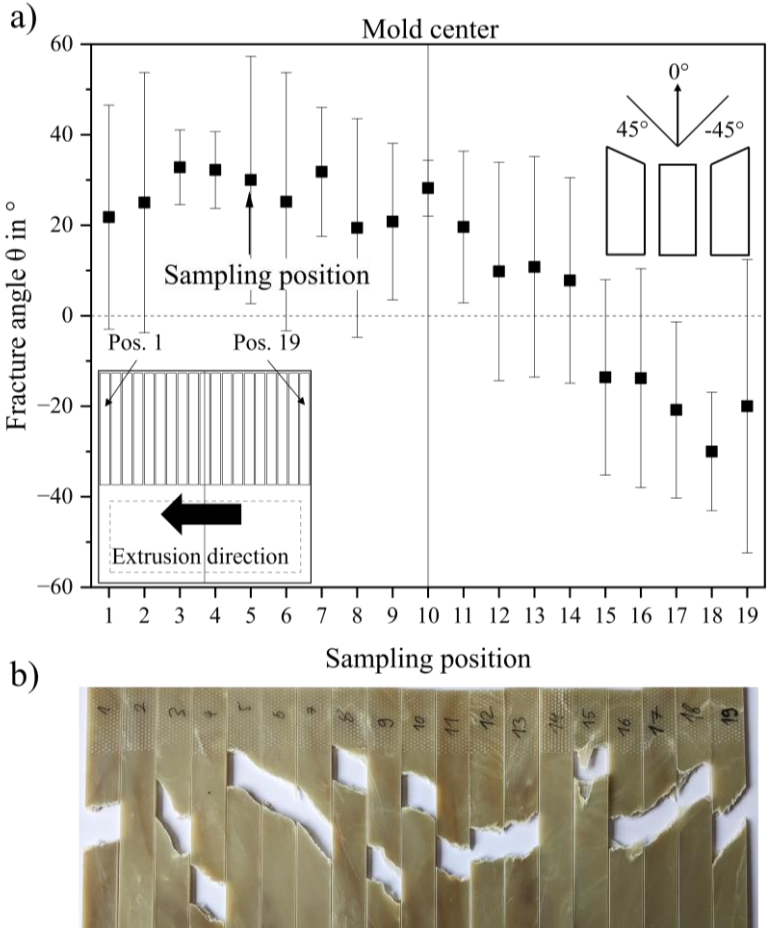

Figure 6.15 Measured fracture angles θ for samples across the entire width of a plate (scheme in the lower left corner a)). Mold center indicated at position 10. Actual tensile fractures are shown in b).

6.5 Mechanical Properties: Flexural

Flexural properties are presented in the same fashion as the tensile properties, sorted by C and F and corresponding linear fit curves. Flexural stiffness E_F is shown in Figure 6.16. The linear correlation to w_f is again strong in C (r = 0.91) and F (r = 0.97) area. The gradient of the fit curves is different between C and F, E_F is not only impacted by w_f but also by the sampling area.

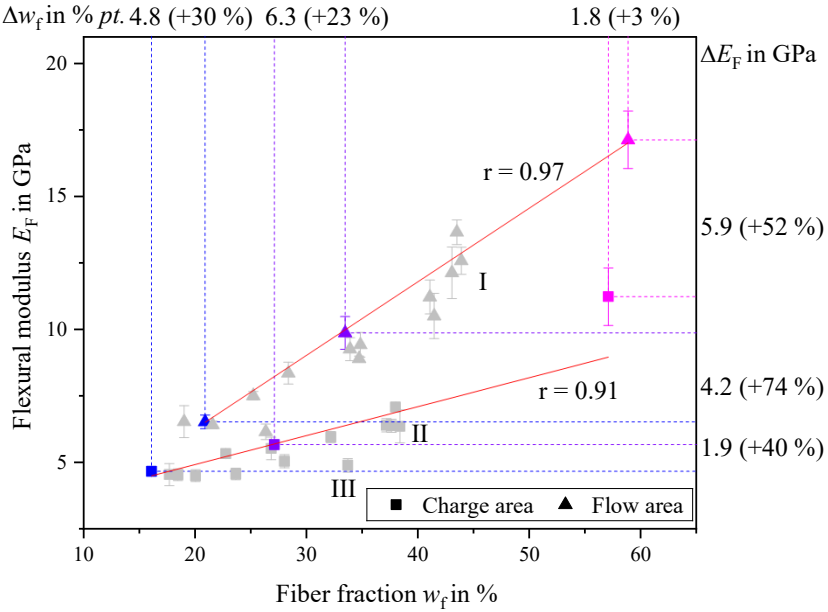

Figure 6.16 Flexural modulus E_F in 0° direction for all sample groups sorted by w_f in C (squares) and F (triangles) area. Every pair of groups is colored the same. Curves of linear fit for C (lower curve) and F (upper curve).

The difference between C and F, up to 114 %, is strongest at medium w_f between $w_f = 30.53$ % and $w_f = 41.34$ %. Those groups (marked I and II) are in the middle of Figure 6.16 right before the highest w_f (in magenta). Similar behavior was reported for PA6 CF and PA6 GF by Scheuring (Scheuring 2024,

p. 151). For the highest w_f, stiffness $E_{F,C}$ is noticeably above the linear fit and closer to $E_{F,F}$. Variances in C are remarkably low at around 4 % except for highest w_f where CV is 10 % (in magenta).

Group I spans from w_f = 41.08 % to w_f = 41.34 % and correspondingly $E_{F,mean}$ from 10.5 GPa to 13.7 GPa. This is apparently mismatched as the low increase of w_f does increase E_F significantly. Parameter set V2 performs particularly poorly. Analysis of factors as well as $\dot{Q}^*$ and *SME* remain inconclusive as all levels are involved here. Fiber lengths l_n and l_w do increase towards higher w_f in this group. Singled out, also from parameter set V2, is a result from the C area (marked III in Figure 6.16). Specific E_F in this case is worse than at the lowest w_f.

Microstructural composition of LFT-D materials, namely the shell-core structure found in the C area, was discussed in 2.6.1 (p. 25) and is schematically depicted in Figure 6.17. This is especially relevant to flexural properties, where outer areas of the specimen are disproportionally more important than areas around the neutral fiber in the middle of the specimen. The fiber orientation in the shell layers is in extrusion direction in 90° to the flow direction and does not contribute.

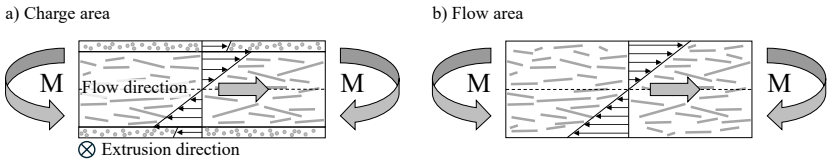

Figure 6.17 Schematic depiction of the influence of layered fiber orientations under flexural load in the C area a) and F area b). Modified from (Schelleis et al. 2023c, p. 17).

Comparable results for flexural properties are rare in the state of the art. Scheuring reported E_F = 12 GPa for PA6 GF44 which is approximately on the fit curve here (Scheuring 2024, p. 152). Scheuring also found results in 11.5° to be higher than in 0°. While no influence could be shown without doubt here, it is certainly to be considered.

Flexural strength σ_F is shown in the next Figure 6.18. In the F area, σ_F is increasing steadily with w_f. Between $w_f = 20$ % and 30 % the results from the C area stagnate below 150 MPa (remark I).

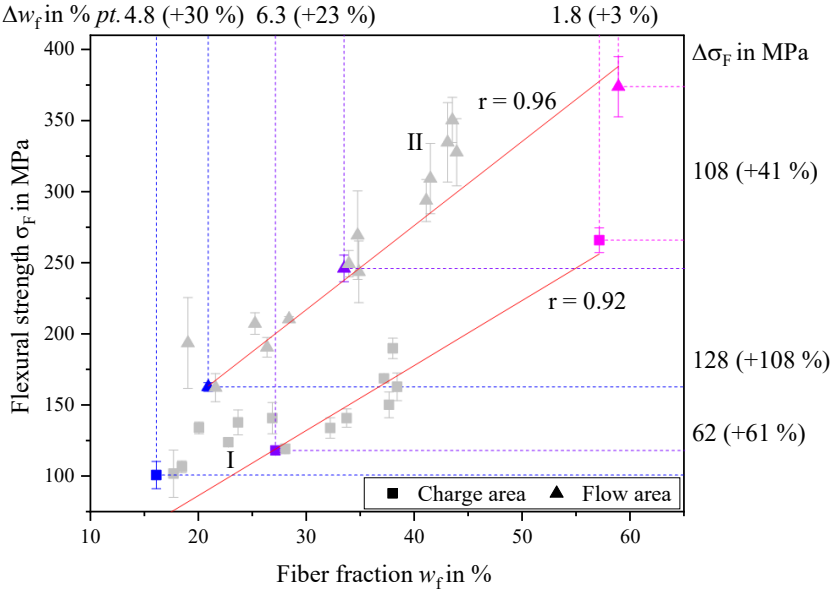

Figure 6.18 Flexural strength σ_F in 0° direction for all sample groups sorted by w_f in C (squares) and F (triangles) area. Curves of linear fit for C (lower curve) and F (upper curve).

Curves of linear fit have similar inclines but $\sigma_{F,C}$ is significantly lower than $\sigma_{F,F}$. The difference is, even more as with E_F, strongest for medium w_f from $w_f = 25.32$ % and $w_f = 41.34$ %. This is well reflected with the selected parameters where $\sigma_{F,F}$ at center point is up +108 % from $\sigma_{F,C}$ while Δw_f is +61 % for lowest w_f and +41 % for highest (noted on the right side of the plot).

Group II, identical to group I from E_F results in Figure 6.16 is outperforming the linear fit curve. Considering ρ, the specific σ_F peaks with this group at 236 $\frac{\text{MPa}}{(\text{kg/m}^3)}$ and drops slightly towards the highest w_f at 221 $\frac{\text{MPa}}{(\text{kg/m}^3)}$. This peak

is V17 with the highest factor levels resulting in highest throughput $m_{LFT\text{-}D}$, medium to high $\dot{Q}^*$ and low φ_v.

6.6 Mechanical Properties: Impact

Impact strength σ_I is exhibited in Figure 6.19. This is the only property tested decreasing towards higher w_f like it was suggested in the state of the art. Linear fit curves without the highest pair are parallel with no exception from C to F area. Again, w_f is the leading influence here. The correlation for the C area is r = 0.90 (r = 0.94 when not accounting for highest w_f) and for the F area the corresponding correlation is r = 0.86 (r = 0.97). In the C area the does not significantly increase between w_f = 20 % and 40 % (p = 0.051, N = 11). This trajectory does roughly match the predictions from Thomason's work, schematically shown in Figure 2.1 (p. 5), where impact properties are expected to fall off at higher w_f.

Differences in w_f result in different properties in C and F with $\Delta\sigma_I$ = 33 % highest at low w_f (blue square and triangle). It remains in this range except for the highest w_f. Variance is high for C area results, CV_{mean} = 20 % and especially high for $\sigma_{I,C}$ at $w_{f,C}$ = 57.08 % with CV = 43 % (magenta square in Figure 6.19). In the C area a considerable surface roughness is present, it does increase with w_f. The outer areas of the plastificate that are subject to lofting are insulated from the hot core by air and therefore cool faster before molding. This rough surface is similar to notches that decrease charpy properties (Grellmann and Seidler 2022, p. 146). Mean CV in the F area is 13 %.

One result from the C area can be singled out breaking the overall trajectory early (remark II in Figure 6.19). It is from V14 which has already been discussed for the poor performance regarding E_C in 6.4 (p. 105). The F area σ_I of V14 is completely in line with other results reiterating the previous remark on the difficult factor-property relationship as C and F area results are often not similarly good or bad in comparison.

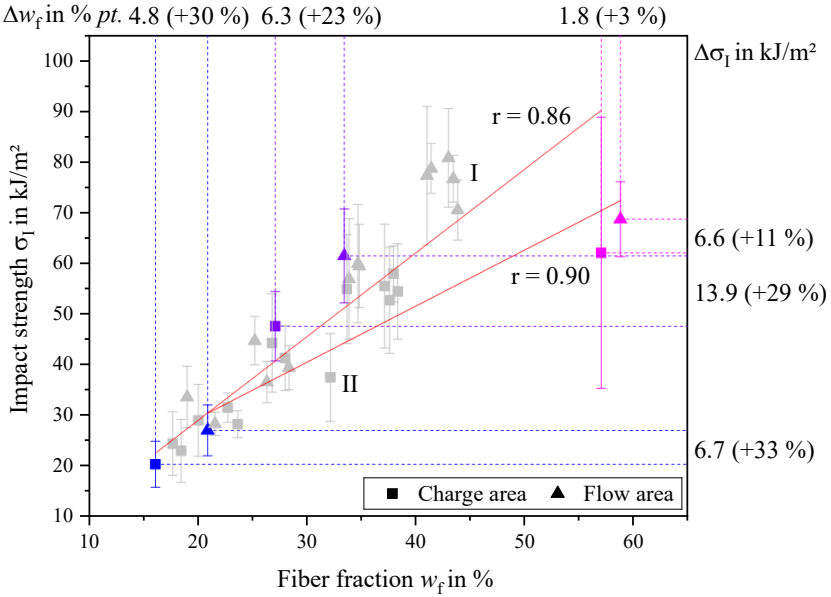

Figure 6.19 Charpy impact strength σ_I in 0° direction for all sample groups sorted by w_f in C (squares) and F (triangles) area. Curves of linear fit for C (lower curve) and F (upper curve).

If connections between factors and mechanical properties exist, it is difficult to make a clear statement about what combinations increase or decrease impact strength. Group I is sorted differently here than in the other graphs, meaning different parameter sets produce the highest E and σ. A factor set cannot be considered universally ideal, only for selected properties. Considering high, occasionally significant, deviations among tensile samples taken next to each other, it might be very difficult to form a coherent picture across all mechanical properties.

7 Discussion

In this section the results from process and material development are put into overarching context with each other and the statistical trial design. Partial answers to the research hypothesis and questions are formulated based on the results. Compatibility of conclusions with observations from literature, where available, is evaluated and discussed.

7.1 Stable and Reproduceable Processing Conditions

Based on observations from previous trials a need for a run-in time in combination with a defined start-up procedure was formulated. A suggestion how such a procedure could look was made and all trials for this work were conducted in close coherence to that (cf. Table A.1 (p. 169)). To monitor processing conditions, measurements were taken at TSE2, the plastificate as well as on plates produced.

Curves of extruder torque and temperature were monitored, analyzed and found to be steady in the relevant production window. A summary of both values can be seen in Figure 5.3 (p. 75). To ensure constant quality, m_{plast} and ρ_{plast} were measured. The weight over production time does exhibit cyclical patterns resulting in around 2 % deviations (cf. Figure 5.4 (p. 80)). This difference in weight will result in a difference in plate height. Although mechanical samples in this work are individually measured, this might not always be the case. It is possible that only one height measurement is taken, and this one value is assumed for all samples. This will add slight deviations just by miscalculating the cross section relevant for the determination of material modulus and strength.

From observations at the LFT-D line, the most likely reason for this is the gap design between the TSE2 die and the subsequent shear and chain belt which

add to a width of approximately 100 mm the plastificate must cover unsupported. The TSE2 die is angled 30° towards the floor. The plastificate hangs in the air until it hits the chain belt. This does elongate the plastificate artificially (Meckes 2024, p. 53). With newer designs of the LFT-D line this problem does not exist anymore as an auxiliary chain belt is installed directly under the die, catching the plastificate immediately after exiting the die.

To ensure consistent w_f, entire plates were burned off to check for the stability of the fiber intake in relation to the polymer throughput. It was found that across five plates $w_{f,mean}$ did deviate as little as 0.6 %*pt.* (1.8 %) (cf. Figure 6.3 (p. 95)). It can be concluded that w_f coming from the LFT-D line is constant.

The center point of the DoE was sampled three times. Comparing processing parameters like M_{TSE2}, v_{intake}, *SME*, $\dot{Q}$*, m_{plast}, ρ_{plast}, between these replicates show variances between CV_ρ = 0.8 % (Table 5.4 (p. 82)) and CV_{MTSE2} = 1.4 % (Figure 5.3 (p. 75)). Flow-front s_{ff} is very similar between the replicates (CV_{sff} = 0.5 %, cf. Table 5.5 (p. 89)).

The replicates for all but one mechanical characteristic in both C and F areas were found to have a small variability compared to the overall variability. Only $\sigma_{F,C}$ was found to have a large variability in the replicates compared to the general variability (cf. Figure 6.18 (p. 117)).

Sufficient run-in time is determined by monitoring M_{TSE} until it plateaus.

One parameter set, V8 (n_{TSE2} = 45 rpm, m_p = 40 $\frac{kg}{h}$, n_{rov} = 8) could not be processed, as the high amount of polymer in the fiber intake zone could not be transported away by the fiber rovings. The same n_{TSE2} and m_p were not a problem with n_{rov} = 16 or n_{rov} = 24.

The trials are run on a timeline with the potential of serial effects occurring. Such effects could be; wear of machinery; environmental conditions like humidity or temperature; physical condition and mood of the operators sustaining weeks of hard work etc.. An analysis of the residuals vs. run order plot from Modde does reveal only localized patterns for some quality features in Figure

A.1 in the Appendix. A residual is the difference between the observed value and the value predicted by the model derived from the DoE. From just a visual inspection the graphs for σ_F, E_F, $E_{F,C}$ follow somewhat localized pattern with the residual vs. run order plot for σ_F being the most obvious one towards the end of the run order (top left sub plot). The material properties modulus and strength are determined at the same time, it is remarkable that respective patterns occur ever only for one of the two. Noteworthy is also that the very first parameter set V1_N11 on position 1 in the run order is singled out in most plots except impact in the last row. This could be because some things in the processing approach (cf. Table A.1 (p. 169)) were not yet properly orchestrated at the very beginning of the trial series.

Next to the production timeline the testing timeline could be a source of a serial effect such as the conditioning of the samples changing during exposition to the climate in the testing facility. Sample preparation, conditioning and tensile testing took place across two blocks, each over the course of several weeks. The samples were vacuum sealed and parameter sets were tested on the same day. No connection to the residual plot can be established except for one sample set. Samples from V1_N11, while subjected to similar procedures as all others, were tested individually one month after the second block.

7.2 Process Microstructure Relation

The microstructure is foundational for all mechanical properties. All aspects of the three fiber related properties are discussed.

7.2.1 Influences on Fiber Fraction

In technical environments, fiber fraction of composites is mentioned often in the product name already to provide an instant classifier of the material. Knowledge of w_f serves comparability to other products and is central to design choices making it the main requirement in production. This work has shown a substantial dependency of mechanical properties on w_f as well as the heterogeneous nature of w_f throughout the plate.

In LFT-D, w_f is determined by choice of the three processing parameters chosen here as DoE factors (cf. 4.2 (p. 59)) and v_{intake} (equation (2.11) (p. 19)) which is a function of the factors in itself (cf. Figure 5.2 (p. 73)). Considering fiber-matrix migration phenomena in LFTs (cf. 2.6.2 (p. 26) and 2.7.2 (p. 37)), w_f cannot be determined by just characterizing one point on a plate. Microstructure characteristics from TGA measurements were presented in Figure 6.1 (p. 93) based on values from Table 6.1 (p. 92), underline the broad w_f spectrum across plates.

General deviations of w_f measurements in LFT-D

Samples from all parameter sets were TGA characterized along the flow path in the C, C-F and F area (cf. sampling scheme in Figure 4.2 (p. 66)). All measurement groups overlap from lowest to highest w_f (cf. Figure 6.1 (p. 93)). The SD of measured values in all three areas are notably highest at lowest w_f and decrease towards highest w_f (cf. Table 6.1 (p.92)).

Evaluating the DoE in Modde, a significant influence of n_{rov} in the distribution broadness of $w_{f,C}$ ($r = -0.89$) and $w_{f,C\text{-}F}$ ($r = -0.71$) was detected, this influence is stronger than the impact of w_f ($r = -0.58$ and $r = -0.51$ respectively). This significant influence evens out towards the end of the flow path at $w_{f,F}$ ($r = -0.62$).

Increasing n_{rov} tightens the w_f distribution which is lower for high w_f.

Optical analysis of selected TGA samples after characterization and discussions with the personnel conducting the measurements reveal a presence of fiber bundles in the samples (cf. fiber skeleton in Figure 6.7 (p. 102)). Fiber bundles are not broken up during compounding and present themselves as twirled rovings of approximately 40 mm to 50 mm length (at $w_f = 33.0$ %). These agglomerations of fibers skew TGA measurements towards higher fiber contents when present. These observations were discussed by Meckes in a characterization benchmark between TGA and a complete characterization of w_f (Meckes 2024, p. 69). This would agree with the following observations regarding the standard deviation.

- SD, especially in the F area, for completely sampled plates is lower, as the relevance of bundles decreases with sample volume.
- SD decreases with increasing w_f, not because there is less chance to measure a fiber bundle but because bundles are so prevalent that the chance nears 100 %.

The TGA sample diameter of 29 mm is determined by the crucible size in the machine. This is close, even lower, to the expected size of the fiber bundles (cf. Figure 6.7 (p. 102)).

TGA measurement of $w_{f,mean}$, inflates SD.

Overall w_f – output of the LFT-D line

Mean $w_{f,mean}$ from TGA characterizations can be compared to $w_{f,calc}$ calculated from measured mean v_{intake} (equations (2.1) (p. 4) and (2.11) (p. 19)). A good agreement, less than 5 % deviation, between $w_{f,calc}$ and $w_{f,mean}$ is found for most parameter sets (mean deviation for all parameters is 3.1 %). The single highest deviation of 8.8 % is found at lowest $w_{f,mean}$ = 18.29 % produced at high n_{TSE2} = 90 rpm, high $m_p = 40 \frac{kg}{h}$ and low n_{rov} = 8. The v_{intake} measurements seem inconspicuous when looking at Figure 5.2 (p. 73). It is one of the flattest curves with little difference from first to last roving. Other than that, no correlations to factors or secondary parameters could be found. Using TGA results, the calculation overestimates w_f for all but four parameter sets, meaning that $v_{intake,mean}$ is too high. Notably, for the replicates of the center point this deviation is between 2.3 % and 6.6 %.

For the center point, five plates were sampled in 25 sections each (cf. Figure 6.3 (p. 95)). With this complete measurement the difference to $w_{f,calc}$ is reduced to 1.8 %. This difference is lower for the highest w_f at 1.6 %.

With v_{intake}, w_f can be calculated if mean processing factors are chosen.

7.2.2 Discussing Fiber Migration

The phenomenon of fiber migration can be expressed as the difference between fiber fractions at two points in parts, for example between the sampling locations $w_{f,F}$ and $w_{f,C}$ (cf. Table 6.1 (p. 92)). It is rooted in different particle movements in suspensions in relation to particle size and suspension viscosity, described in 2.6.2 (p. 26).

An overview of w_f in C and F is given in Figure 6.2 (p. 94) with values found in Table 6.1 (p. 92). A full consideration of the topic is presented in Figure 6.3 (p. 95) and the influence of the plastificate is presented in Figure 6.4 (p. 98). Considering the major correlation between w_f and mechanical properties, the differentiation between $w_{f,C}$ and $w_{f,F}$ for the respective sample groups is crucial and was considered (all Figures concerning mechanical properties in chapter 6).

Fiber content w_f needs to be determined as close to the sample as possible.

There is a moderate negative correlation ($r = -0.6$) between the *SME* (cf. Table 5.1 (p. 76)) and the relative fiber migration, the difference between $w_{f,C}$ and $w_{f,F}$. This is stronger than the correlation with $w_{f,mean}$ ($r = -0.47$).

High *SME* leads to lower fiber migration.

While *SME* is influenced by M_{TSE} which, in turn, is influenced by w_f it is also influenced by the throughput. All the above, particle size, M_{TSE} and *SME* are related to the choice of polymer matrix material and by that, inseparably linked to the viscosity.

Fiber migration needs to be evaluated for every LFT-D material combination.

7.2.3 Fiber Lengths

One of the core ideas of LFT-D process optimization is the possibility to manipulate l_f to one's advantage via choice of processing parameters, especially n_{TSE2} (cf. 2.7.1 (p. 29)). The route chosen to characterize l_f has proven to be

unsuitable for the material microstructure at hand (cf. 6.2 (p. 101)). Even across a large w_f range, measured l_f does not change substantially. The fiber lengths and bundles observed visually after removal of the matrix (cf. Figure 6.7 (p. 102)) however suggest that l_{crit} is far exceeded anyways independently of chosen processing parameters.

7.2.4 Fiber Orientation Development from Plastificate to Plate

The first research question is not conclusively answered at this point, but it became clear that the continuous-discontinuous nature of the process and resulting microstructural implications are to be at the core of the investigation. This puts the focus on the plastificate and links the first research question to the second research question: "What role does the plastificate hold […]?"

Fiber orientations in LFT-D plates were found to be out of a perfect alignment with flow direction in literature (cf. 2.7.2 (p. 37)). The reasons for this are assumed to be either screw pitch at TSE2 exit (Bondy et al. 2017), the fiber orientation in the plastificate (Tröster 2004, p. 87) or the temperature gradient of the plastificate (Radtke 2009).

The plastificate was characterized by measuring the temperature (cf. 5.2.1 (p. 77) and Table 5.2 (p. 79)) as well as determining the fiber orientation (cf. 5.2.5 (p. 84)). Both were found to be almost constant for all sample sets and in any case independent of DoE factors. While the screw pitch was not investigated here, this seems unlikely as the plastificate die where the material is compacted follows immediately after TSE2. Trials with PC GF LFT-D have shown a strong fiber orientation in the plastificate using the same setup and parameters.

Neither plastificate core temperature nor fiber orientation is influenced by LFT-D factors investigated here.

When LFT-D is molded the material is frozen immediately upon mold contact, supposedly preserving the fiber orientation φ in the outer layers (cf.

2.6.1 (p. 25)). The main fiber orientation angle φ_v is determined via tensile disc characterization (cf. Figure 6.8 (p. 103)) and the change in fiber orientation across plates can be seen with the fracture angle analysis conducted (cf. Figure 6.15 (p. 114)).

Figure 7.1 a) through c) illustrates the influence of n_{TSE2} on properties further along the process chain. The general relation between n_{TSE2} and ρ_{plast} is shown qualitatively in a) and was presented in detail in 5.2.2 (p. 79). When n_{TSE2} is increased, ρ_{plast} decreases ($\rho_2 < \rho_1$) and plastificate dimensions increase accordingly ($l_2 > l_1$). The influence of ρ_{plast} on s_{ff}, plot in d), is shown to increase from r = 0.50 to r = 0.74 when excluding three parameter sets (marked red), all on DoE corner points. The density is low for these settings with n_{TSE2} = 90 rpm. The other four parameter sets at low ρ_{plast} , three of which located on the faces of the DoE, are processed at lower n_{TSE2} = 45 rpm and n_{TSE2} = 67.5 rpm. Another value closely related to ρ_{plast} is the length displacement D_l (cf. Table 5.3 (p. 81)) which is also correlated with s_{ff} (r = 0.71).

Flow-front skewness s_{ff} is influenced by plastificate properties ρ_{plast} and D_l.

A flow study is conducted (cf. 4.4.2 (p. 64)), and the skewness s_{ff} of the flow-front is characterized (cf. Table 5.5 (p. 89)). This is qualitatively shown in Figure 7.1 in b) and for the evaluation of s_{ff} and resulting φ_v in c). The s_{ff} can be correlated with φ_v as is demonstrated in Figure 7.1 e). Considering the broad deviations of both s_{ff} and φ_v, discussed in the respective chapters, the linear correlation can be increased from r = 0.43 to r = 0.93 when excluding certain parameter sets (marked red).

The s_{ff} value provides insight into expected fiber orientations φ_v in the F area.

Unfortunately, no similarities between these sets can be found. Clear connections between s_{ff} and DoE factors cannot be found. Especially V7 (lowest φ_v), highest w_f, is an oddity.

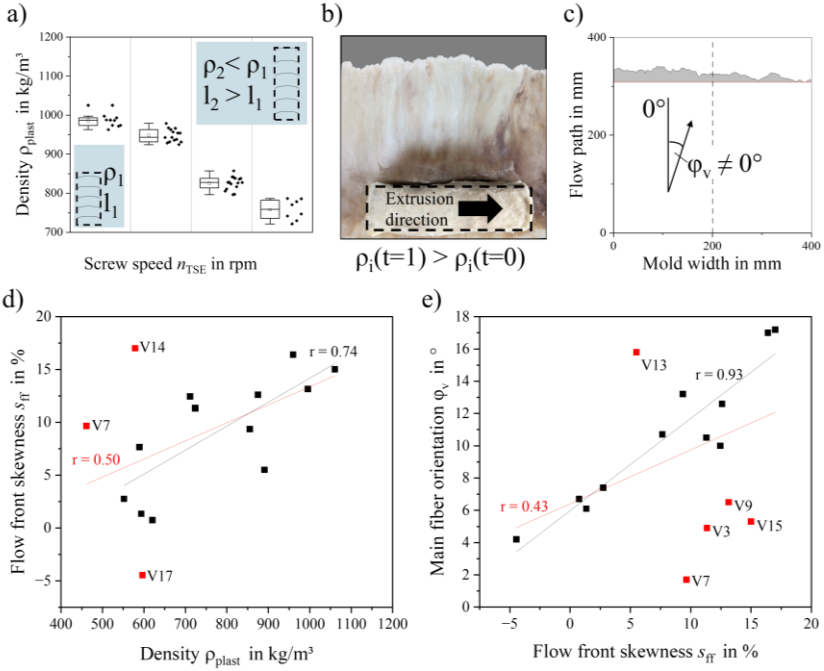

Figure 7.1 Influence of n_{TSE} on microstructure development. Qualitative relation between n_{TSE} and ρ_{plast} a). Schematic view of a flow study and plastificate b). Evaluation of flow study and indicated φ_v c). Complete (red line) and curated (black line) linear correlation between s_{ff} and ρ_{plast} d) and between φ_v and s_{ff} e).

In the development of the flow-front and subsequently the fiber orientations, two mechanisms overlap, both influenced in multiple ways. One aspect is the general “roundness” of the flow-front, visualized in the following Figure 7.2 a) where the flow study was conducted with colored plasticine. Mold coverage influences material flow, resulting in a radial or shear flow as shown in Figure 2.7 (p. 24). The coverage of the mold is influenced by plastificate dimensions, especially length (cf. plastificate dimensions, Table 5.3 (p. 81)), in turn influenced by the density ρ_{plast} ($r = -0.95$) (cf. Table 5.4 (p. 82)) which decreases with w_f ($r = -0.86$).

Plastificate length should be as close to mold length and D_l as low as possible to reduce s_{ff} and φ_v.

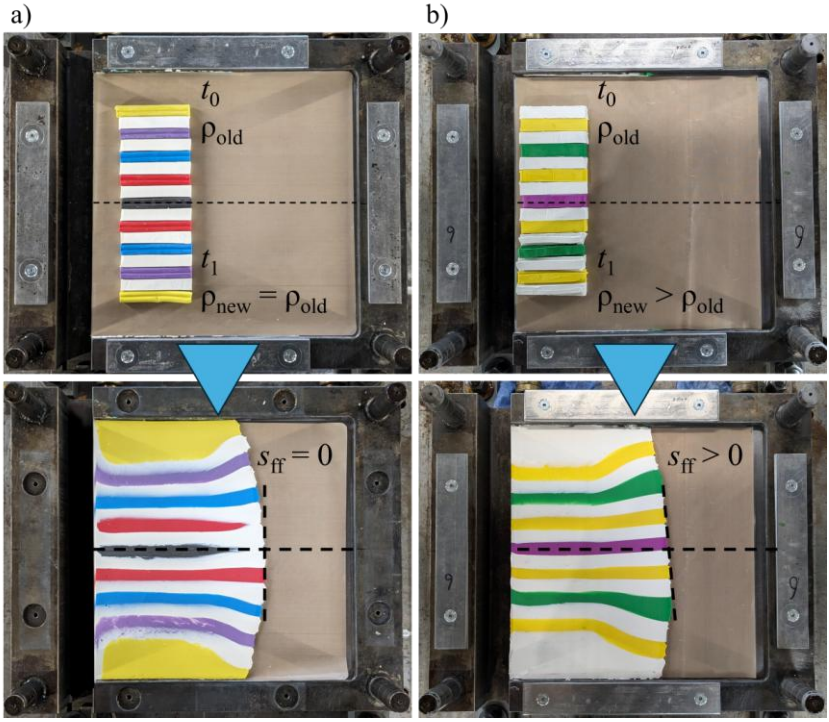

Figure 7.2 Short-shot flow study of colored plasticine blocks. Horizontal dashed lines mark the middle of the mold. Homogeneous distribution of plasticine mass, the dashed line marking the crest of the flow-front is perpendicular to the mold middle a). Simulating a density gradient, resulting in a skewed flow-front b). Modified from (Schelleis et al. 2025b)

The other factor influencing s_{ff} is the plastificate density gradient $\Delta\rho$ interpretable as the center of mass shifting away from the center of volume. This effect, indicated as ($\rho_2 < \rho_1$) in Figure 7.1 b) is expressed as $\Delta\rho$ (cf. Table 5.4 (p. 82)) as well as mentioned before in D_l (cf. Table 5.3 (p. 81)), visualized in Figure

4.1 (p. 64). A simulation with this premise was conducted in the framework of a paper by Schelleis et al. (Schelleis et al. 2025b), showing that the flow-front can be forced into skewness by altering the material distribution in the plastificate mimicking Δρ. This asymmetry can be provoked via shifting material towards the new end of the plastificate. Note the dashed lines intersecting the mold middle lines in b). It is in very good agreement with Radtke's model conception of a skewed flow-front but does provide a different explanation to Radtke's temperature gradient in the plastificate (Radtke 2009, p. 63).

The impact of the extrusion time per plastificate cannot be understated. The step from continuous LFT-D compounding to discontinuous compression molding has, via the plastificate, an impact on microstructure and mechanical properties.

The plastificate cannot, under no circumstances, be perceived as homogeneous.

7.3 Process Parameter Optimization

The DoE experiment was set up to analyze the relationship between parameter selection and mechanical performance. Two types of plots are investigated and presented here, coefficient plots and response contour plots.

DoE analysis – coefficient plots

Coefficient plots show significance of model terms. Insignificant terms were excluded starting with the least significant to consider the effect of exclusion on the model. In the following three Figures, Figure 7.3, Figure 7.4 and Figure 7.5, the coefficients are normalized to enable a comparison between different response ranges. The DoE factors have a similar impact for all properties presented here. An increase in screw speed and roving amount or a decrease in polymer throughput will have a positive effect on the quality features, here an increase in mechanical properties. This correlates with the increased w_f induced by every single one of these actions (cf. 2.5.3 (p. 19)). For a lot of the properties, the impact of the roving amount is strongest. The choice of factor

level is the reason for that. While n_{TSE2} and m_p are doubled, n_{rov} is tripled which has a greater impact on w_f.

Figure 7.3 shows the coefficient plots for the tensile properties E and σ in C and F area. The E_C is influenced by a negative quadratic interaction of n_{TSE2} (Figure 7.3, b)) indicating that the optimal set point for n_{TSE2} is not at the highest value. While n_{TSE2} does generally improve mechanical properties it should not be set to an extreme point. A similar observation can be made for E_F where n_{rov} has a negative quadratic interaction (Figure 7.3 d)). The C area is also critical for the flexural modulus E_F in Figure 7.4 b). Here, two barely significant interactions between n_{TSE2} and m_p and n_{TSE2} and n_{rov} occur. This indicates that the effect of one factor depends on the set point of the other factor. The first interaction between n_{TSE2} and m_p is negative, indicating that the influence of an increased n_{TSE2} is slightly weakened by increasing m_p. The positive interaction between n_{TSE2} and n_{rov} underline this finding. In Figure 7.4 c) a negative quadratic interaction of n_{rov} is displayed while a positive interaction between n_{TSE2} and m_p is just barely significant.

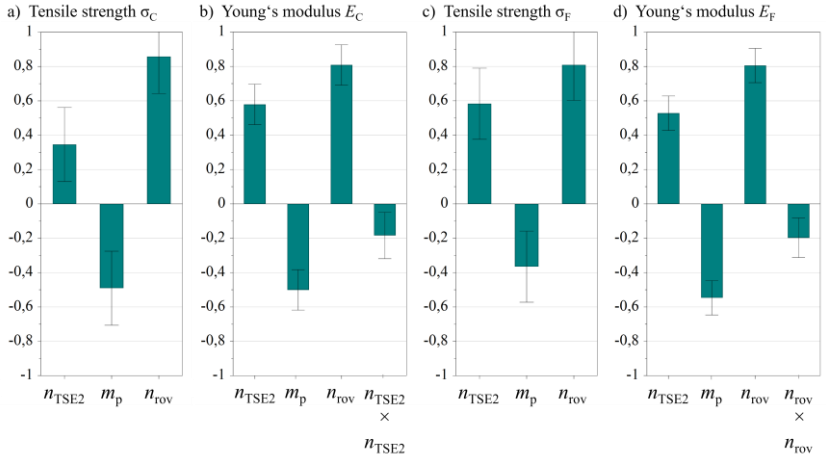

Figure 7.3 Normalized coefficient plot for factor effects on tensile properties, strength σ and modulus E. Sorted by C area (plot a and b) and F area (plot c and d).

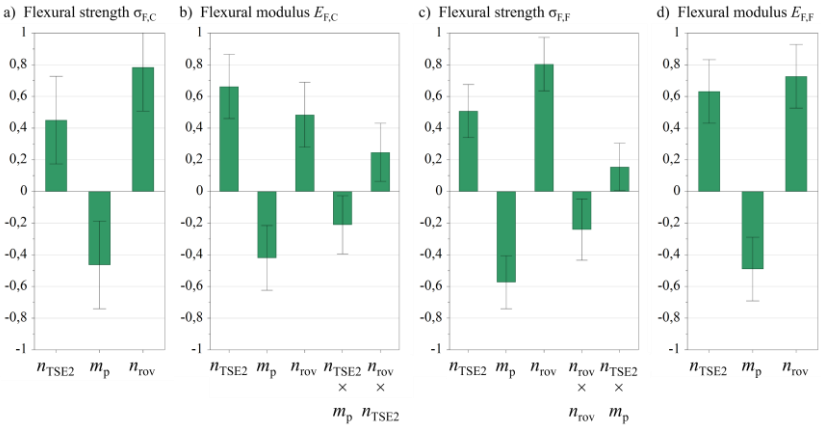

Figure 7.4 Normalized coefficient plot for factor effects on flexural properties, strength σ_F and modulus E_F. Sorted by C area (plot a and b) and F area (plot c and d).

Coefficient plots for the effect of factors on impact strength σ_I in C and F areas area are shown in Figure 7.5. Influences on $\sigma_{I,C}$ are magnitudes higher than in all other plots, this is not clear in the normalized representation chosen here. The same general trend relating to the strong w_f dependence of mechanical properties can be observed here as well. For both areas, a negative quadratic influence of n_{rov} can be seen. This indicates an upper threshold for n_{rov} within the parameter space investigated. The impact strength was the only mechanical property severely dropping off above $w_f = 45$ % (cf. Figure 6.19 (p. 119)).

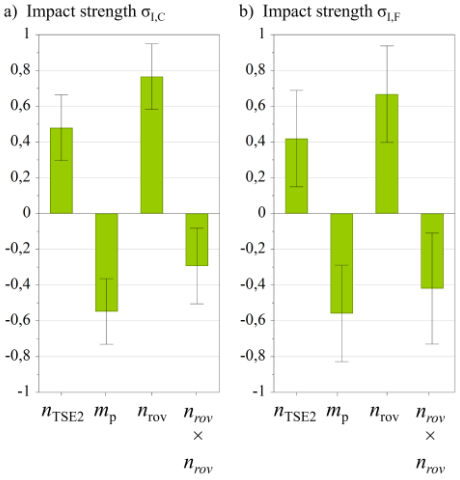

Figure 7.5 Normalized coefficient plot for factor effects on impact properties, σ_I. Sorted by C area, a) and F area, b).

The following general recommendations for the parameter space investigated here can be derived from the previous figures.

If only and broadly judging by mechanical performance, the factors should be set to their respective extremes, n_{TSE2} and n_{rov} at the high setting and m_p at the low setting, just by virtue of increasing w_f.

Usually there are requirements regarding processing boundaries for example the total throughput $m_{LFT\text{-}D}$ and most commonly w_f. In this case, m_p is given and only combinations of n_{TSE2} and n_{rov} are relevant. Here, the current teaching would be to go as low as possible with n_{TSE2} and adjust n_{rov} accordingly until w_f is reached (Tröster 2004, p. 57). Considering the coefficient plots shown, this statement is not backed by the findings presented here, where n_{rov} has more negative interactions than n_{TSE2}.

Maximize n_{TSE2} first, then n_{rov} while keeping m_p low.

While the desired w_f could be reached, in theory, with a very high n_{TSE} and one roving, this is obviously not feasible. Here, further considerations regarding processability come into play and these two recommendations here are superseded by other observations especially regarding the fiber microstructure and in turn the influence of a high n_{TSE2} on plastificate lofting discussed before.

DoE predictions – response contour plots

The following figures show the response contour plots representing a prediction of mechanical properties regarding the investigated parameter space. Response contour plots display the model's predicted mechanical property over the selected factors range while keeping the other factors at their mean value. All are sorted between the C (upper part a) of each figure) and F area (lower part b) of each figure). The contour color is locked in each set of plots in each figure but cannot be compared between figures. For all plots shown, the w_f does decrease from left to right as m_p does increase from 20 kg/h to 40 kg/h. The upper right edge of every plot is an area of high w_f and the lower left edge an area of lowest w_f respectively.

The relation of w_f to n_{rov} and n_{TSE2} was shown for $m_p = 30$ kg/h in Figure 2.5 (p. 20) where the lines of constant w_f are hyperbola-shaped. This hyperbola shape can be seen in some mechanical properties, not all, of the following plots. The linear relation between w_f and all mechanical properties was shown in the respective discussions in chapter 6. The contour lines for w_f are included and are the same in all plots for every set point of m_p. These lines represent the calculated w_f as it is put out of the LFT-D line (cf. 7.2.1 (p. 123)). Mechanical properties are measured at locations on the plate where fiber migration has had a considerable effect on w_f. Accordingly, a comparison between C and F regarding the factor effects can only be made qualitatively, that is, how the contours of w_f and mechanical property relate to each other.

Where the contour approximately follows lines of constant w_f, for example with E_F in the following Figure 7.6 b), the previously observed linear relation between w_f and E_C is upheld (cf. Figure 6.9 (p. 106)). In Figure 7.7 the contour lines follow a simple linear falling trajectory. Both examples are in line with the coefficient plots for the tensile properties in Figure 7.3 (p. 132), where

quadratic effects were found for E but no further interactions were found for σ. When contours are parallel, the choice between the set points of n_{TSE2} and n_{rov} is up to the user. The influence on the mechanical property on display can be neglected. Dealing with a linear contour trajectory, a medium setting of n_{TSE2} and n_{rov} would underperform the general relation to w_f. However, this is an artifact from the underlying model statistics, not necessarily reality. The gradient of a linear contour can nevertheless provide information about a preferable factor selection.

Closer examination of Figure 7.6 reveals, that contour lines for w_f and E align differently between C and F and differently for various levels of w_f. in every plot. This makes blanket statements regarding parameter choices difficult. For the following discussions a fictitious target of $w_f = 35$ % is assumed. This is highlighted by a black frame in each plot. To further focus the discussion, a moderate LFT-D output is also targeted by setting $m_p = 30$ kg/h. In this situation, the contour lines for $w_f = 35$ % and E are parallel.

For E_C at lower w_f, choosing a higher n_{TSE2} is recommended and at higher w_f, a higher n_{rov} should be prioritized.

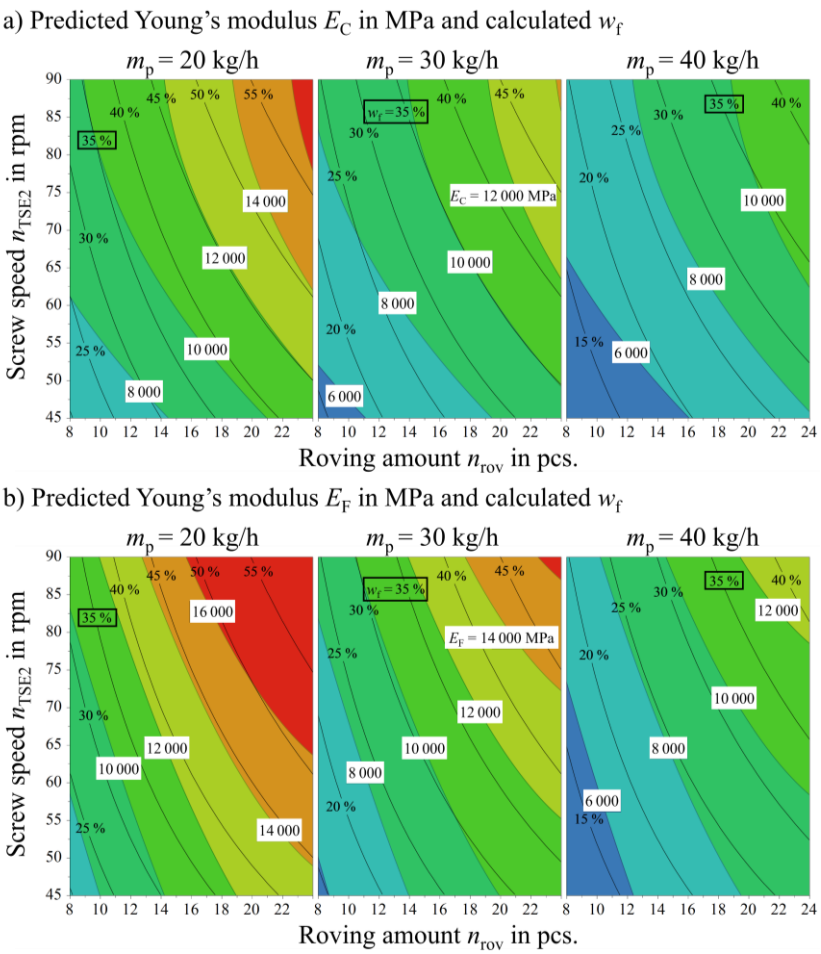

Figure 7.6 Response contour plots for Young's modulus E_C in the C area a) and E_F in the F area b) superimposed on contours of constant w_f.

The plots for tensile strength σ in Figure 7.7 do only show linear factor effects. In Figure 7.7 a) both combinations of high n_{TSE2} and low n_{rov} and vice versa show similar results considering σ_C. A medium setting for each factor is not

recommended. This is different for σ_F, where associated contour lines exhibit steep negative slopes.

To optimize σ_F set n_{rov} high and n_{TSE2} low accordingly.

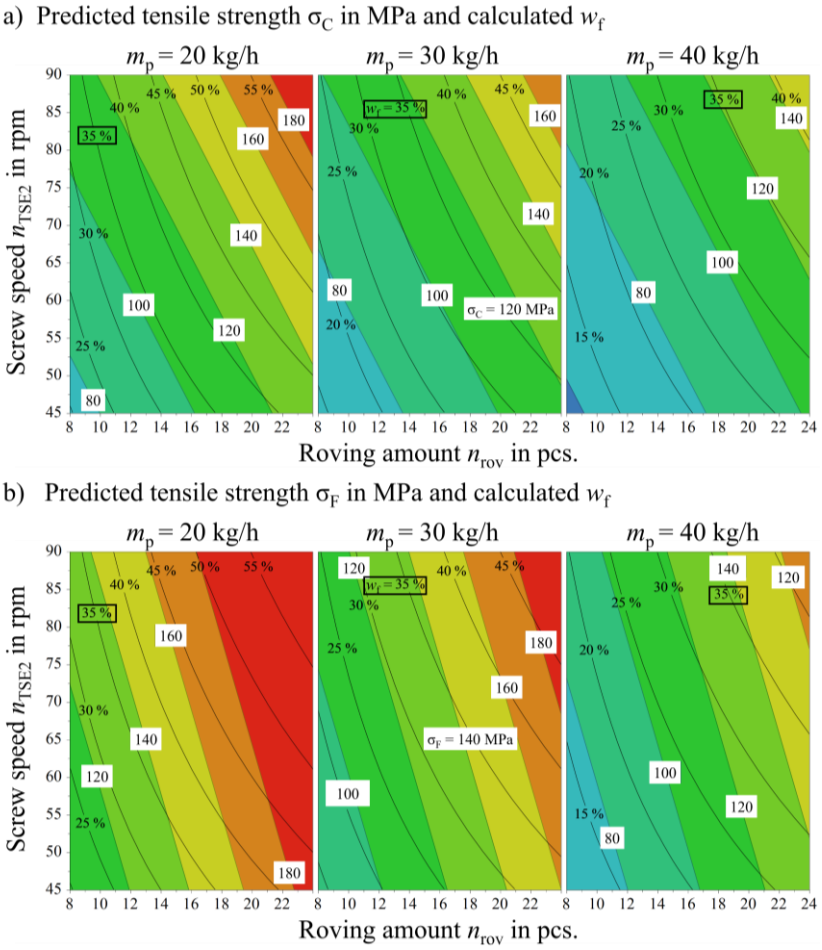

Figure 7.7 Response contour plots for tensile strength σ_C in the C area a) and σ_F in the F area b) superimposed on contours of constant w_f in relation to the DoE factors.

The flexural properties E_F and σ_F are very different between C and F area because of the different fiber orientations originating in plastificate placement (cf. Figure 6.17 (p. 116)). In both areas in Figure 7.8, the general relation between w_f and E_F is similar. In both cases the positive influence of a high set point of n_{TSE2} is apparent.

To optimize E_F, n_{TSE2} should generally be maximized.

This influence of n_{TSE2} is less strong at higher w_f but increasing n_{rov} is not to be recommended.

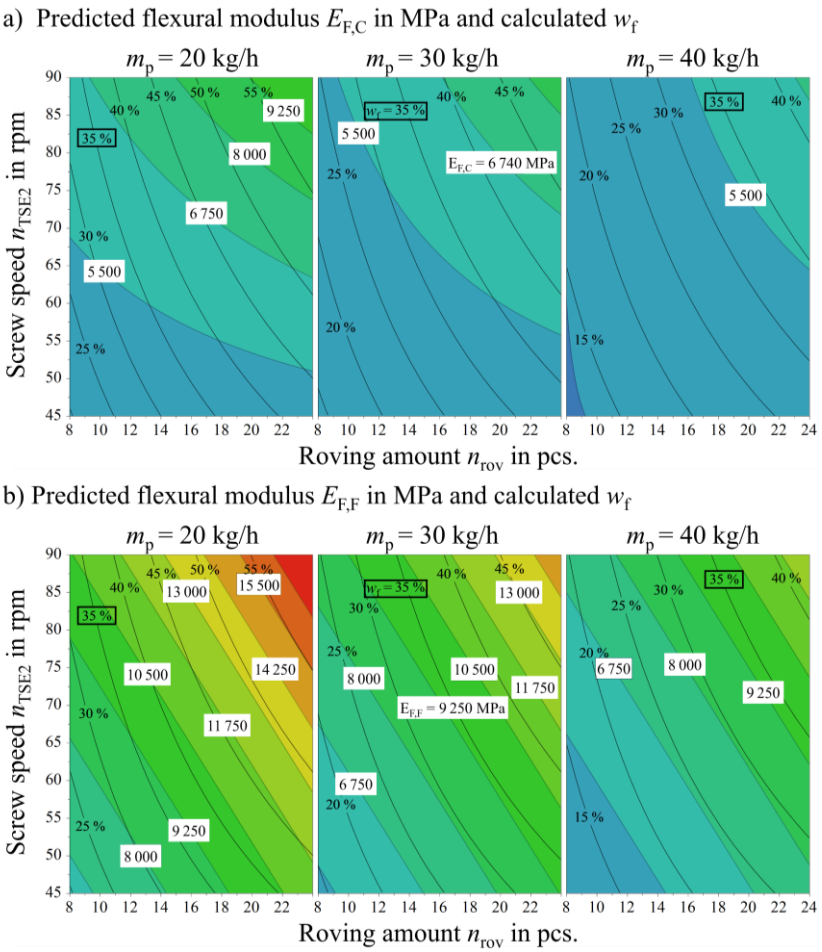

Figure 7.8 Response contour plots for flexural modulus $E_{F,C}$ in the C area a) and $E_{F,F}$ in the F area b) superimposed on contours of constant w_f.

Contour lines for factor effects on flexural strength $\sigma_{F,F}$ in Figure 7.9 b) are very steep for m_p = 20 kg/h. This effect tapers off approaching the highest m_p set-point. In the C area, Figure 7.9 a), $\sigma_{F,C}$ does not increase much with w_f.

To optimize σ_F, n_{rov} should be maximized at low m_p.

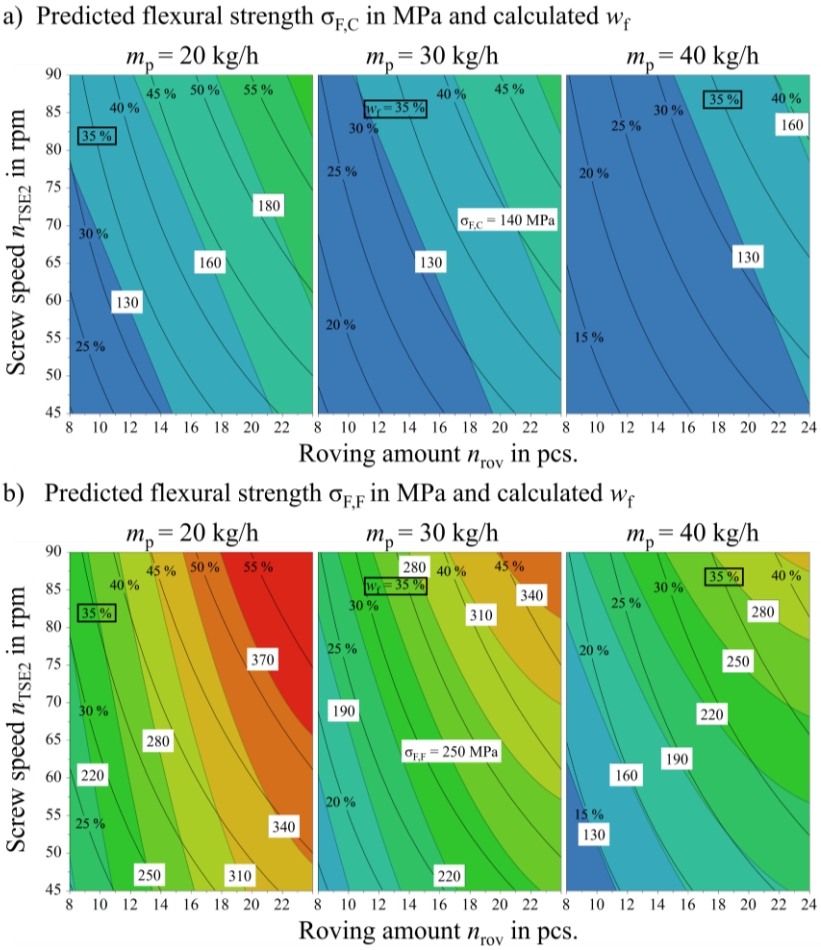

Figure 7.9 Response contour plots for flexural strength $\sigma_{F,C}$ in the C area a) and $\sigma_{F,F}$ in the F area b) superimposed on contours of constant w_f.

The last response contour plot, Figure 7.10, considers the impact strength σ_I. In the C area for m_p = 20 kg/h and 30 kg/h at low w_f < 35 % it is recommended to prioritize n_{rov} over n_{TSE2} This finding is even stronger for $\sigma_{I,F}$. Crossing the w_f = 35 % threshold, both $\sigma_{I,C}$ and $\sigma_{I,F}$ decrease when increasing n_{rov} instead of n_{TSE2}.

To optimize σ_I at $w_f \geq 35$ %, n_{TSE2} should be maximized for all m_p.

The maximum of n_{rov} within the parameter space investigated here is clearly visualized in Figure 7.10 b) for $\sigma_{I,F}$ as it is the only mechanical property decreasing for high w_f (cf. Figure 6.19 (p. 119)).

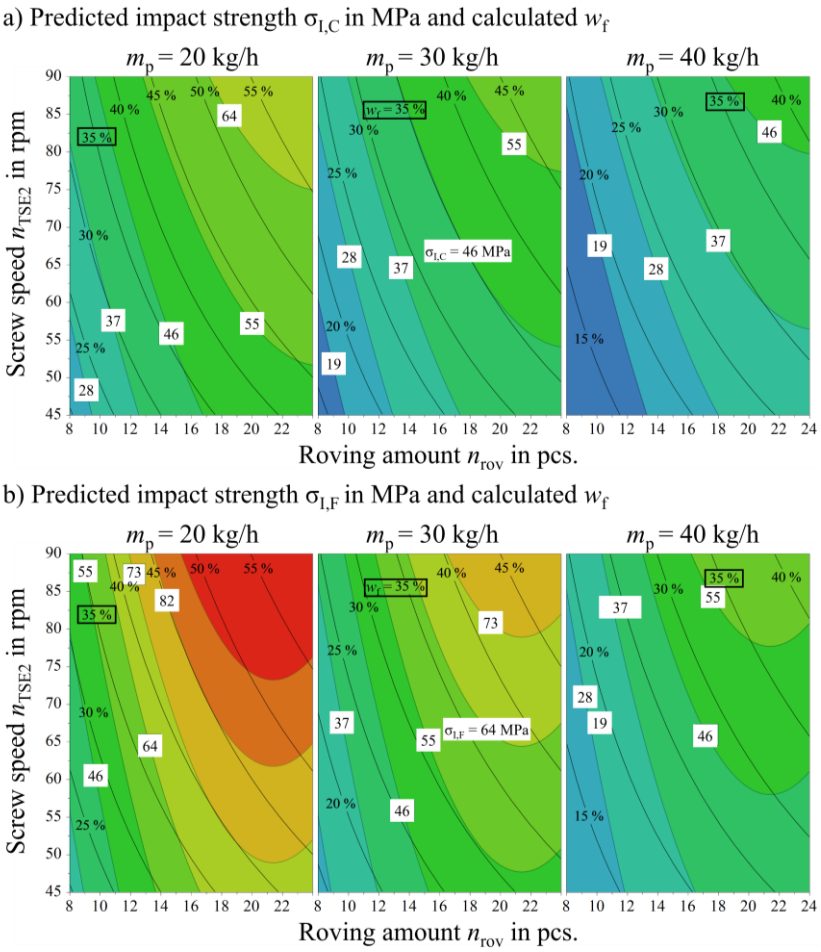

Figure 7.10 Response contour plots for impact strength $\sigma_{I,C}$ in the C area a) and $\sigma_{I,F}$ in the F area b) superimposed on contours of constant w_f.

8 Conclusions, Limits and Outlook

This work revolves around material characterization and process factor development for a compression molded glass fiber reinforced PA6 composite. A DoE study with the key LFT-D extrusion factors polymer throughput, screw speed, and roving amount, was conducted. Three types of test specimens were prepared for this study. Plastificates were quenched at the extruder exit. A short-shot flow study was conducted and plates for microstructural and mechanical characterizations were molded.

The influences of processing parameters as well as resulting fiber content on the semi-finished material, the plastificate, were characterized. Plastificate dimensions as well as the density were measured. Both dimensions as well as density are highly dependent on fiber content and processing parameters, especially screw speed.

The importance of fiber microstructure development was introduced in the state of the art. Throughout this work, the influence of the plastificate on the microstructure is highlighted. Suitable characterization methods were developed and presented here.

The fiber orientation in the flow area was determined by tensile disc testing and found to be skewed out of flow direction. This was backed by fracture pattern investigations. This phenomenon could be linked to the skewness of the flow-front during mold filling which was in turn determined to be caused by a density gradient in the plastificate. Flow-front skewness as well as the plastificate density evaluation are valuable tools for further material and process development.

The fiber migration across the flow path was characterized and considered in the evaluation of mechanical properties. An approach to complete fiber fraction characterization was presented and utilized. Fiber content increases with flow length for all factor combinations mainly driven by the mean fiber

content. The influence of the dimension of the plastificate charge area, determined by plastificate length, was discussed.

Tensile, flexural and impact properties were characterized in flow direction. All mechanical characteristics except impact toughness feature a steady increase with increasing fiber content. Via the fiber content, the mechanical properties are thus indirectly related to all process factors influencing the plastificate.

Mechanical properties were chosen as quality features in the DoE evaluation where coefficient and response contour plots were discussed. From the coefficient plots no clear recommendation regarding an ideal factor setting can be made. A high roving count, however, has the most negative interactions and should be avoided. Accordingly, the screw speed should be set at a medium to high level. The response contour plots show no clear recommendations either and need to be studied carefully for individual optimization goals under given boundary conditions.

The research hypothesis and accompanying questions are repeated and answered here.

Research hypothesis

"During continuous extrusion of fiber-reinforced semi-finished products for direct processing in discontinuous compression molding, the choice of parameters of the mixing extruder has a significant, positive, influence on specific mechanical properties when fibers are gently mixed at low screw speeds and high fill grades."

No. This hypothesis cannot be backed by the findings of this work. While some properties profit from low n_{TSE2}, this statement cannot be generalized. From the recommendations given over the course of chapter 7, no clear conclusion regarding ideal factor settings can be drawn. As presented in chapters 5 and 6, factor interactions are multifaceted and often counteracting at all processing stages.

Research Questions

Question 1: Can key extrusion characteristics such as $\dot{Q}^*$ or the *SME* be correlated with good mechanical properties and thus be used for the selection of the parameters in the mixing extruder?

No. While promising simplification, summarization of factors in key characteristics cannot be translated into general statements about the resulting quality. The use of $\dot{Q}^*$ could support factor selection in experiment design, since parameter sets with a similar $\dot{Q}^*$ behave predictable. For example, the relationship between w_f and lofting is linear for similar $\dot{Q}^*$.

Question 2: "What role does the plastificate hold at the transition between continuous and discontinuous part of processing regarding fiber microstructure development?"

The plastificate is the decisive link between both the LFT-D and compression molding processes. What became clear over the course of this work is the immense impact the plastificate has on resulting microstructure. It is heavily influenced by processing parameters and material system. Following is a non-exhaustive selection of implications to be considered in the future:

- Different processing parameters accounting for different part sizes or cycle times, will result at least in different dimensions and densities of the plastificate.
- The influence on fiber orientation or fiber content is important and even things as trivial as changing the extrusion direction relative to the mold can alter the parts properties and performance.
- Changing the matrix material has a profound effect on viscosity and thereby all other effects shown. Industries desire to keep the press forces as low as possible is understandable, being directly linked to investment costs. Not only is moldability to be considered in this context but also the processability. A lower viscosity means various things in extrusion but does increase lofting of the plastificate in any case. The influence on the density gradient is hardly predictable until investigated.

8.1 Limits and Transfer Strategies

This thesis cannot provide a definitive solution to LFT-D material development. However, it presents a framework in which such a development can be structured and helps to explain common phenomena observed. Core investigations on any new LFT-D material system should comprise microstructure investigations into fiber-migration and orientation deviation φ_v. Fiber migration is most important here and can be qualitatively investigated with very simple means. While φ_v can be determined in tensile disc testing, a flow-front study can be conducted and evaluated during trials with very little extra effort.

The relation of mechanical properties between C and F area shown in this work is tied to fiber migration and can only be transferred to other systems if the fiber migration behaves similarly. Fiber migration was investigated for other LFT-D material systems parallel to this work. For the more viscous PC GF LFT-D the fiber-migration was found to be negligible (Schelleis et al. 2023c, p. 2051). Scheuring did investigate PA6 with GF, CF as well as a GF CF hybrid. The higher CF filament count increased the suspension viscosity and thus the fiber migration of PA6 CF LFT-D is less pronounced than with PA6 GF (Scheuring et al. 2024, p. 8).

Plastificates can be cut by simple means as well and evaluation of the cut surfaces allows for quick insight into density distribution in extrusion direction. For PC GF LFT-D these investigations were conducted and while much denser than the PA6 GF plastificates discussed here, the general phenomenon, including the φ_v deviation was observed.

8.2 Outlook

The following list of topics warrants further investigations:

- Can the findings of this work be transferred to bigger, industrial sized machines? The throughput to screw speed ratio could play an important role.
- This work has not considered screw configurations in the compounding extruder. Different screw elements can affect the fiber length and dispersion. This could, on top of direct influences on mechanical properties, additionally affect the lofting of the plastificate and all associated effects.
- How does lofting affect fiber orientations through the part thickness in the C area? This is of great importance to flexural properties and could be one aspect of parameter optimization. Additionally, does lofting affect the interface quality in the C area by cooling a bigger volume of material?
- How do molding parameters influence the microstructure? Closing speeds could alter the shear conditions in the mold and thus fiber migration. Mold temperatures are rarely homogeneous, this could influence mold filling and resulting fiber orientations.
- How does particle migration work for other fillers like flame retardant additives? This is a safety relevant aspect of a phenomenon that has not received too much attention.
- How to measure fiber lengths for LFT-D materials where l_f is exceeding the capability of current methods? A suitable characterization method can support more detailed investigations into factor effects on the LFT-D material.
- How do the findings of this work transfer to complex part geometries? Are features like ribs, beads and weld lines influential regarding flow-front (re-) orientation and fiber migration?

List of own Publications

Journal articles as main author

Schelleis, C.; Scheuring, B.M.; Liebig, W.V.; Hrymak, A.N.; Henning, F. (2023): Approaching Polycarbonate as an LFT-D Material: Processing and Mechanical Properties. In *Polymers* 15 (9), pp. 2041–2065. DOI: 10.3390/polym15092041.

Schelleis, C.; Scheuring, B.M.; Schreyer, L.; Liebig, W.V.; Hrymak, A.; Kärger, L. et al. (2025): Skewness of Flow Front and Fiber Orientation in LFT-D Compression Molding considering Processing, Characterization and Simulation. In *Journal of Thermoplastic Composite Materials* 38 (8), pp. 2922-2944. DOI: 10.1177/08927057251344252.

Journal articles as contributing author

Christ, N.; Scheuring, B.M.; Schelleis, C.; Liebig, W.V.; Montesano, J.; Weidenmann, K.A.; Hohe, J. (2024): Characterization and Simulation of the Interface between a Continuous and Discontinuous Carbon Fiber Reinforced Thermoplastic by Using the Climbing Drum Peel Test Considering Humidity. In *Polymers* 16 (7), pp. 976–1003. DOI: 10.3390/polym16070976.

Conference proceedings and presentations

Peer reviewed proceedings and presentations

Schelleis, C.; Henning, F.; Hrymak, A. (2024): Comprehensive material development of glass fiber reinforced polyamide 6 LFT-D: Proceedings of ITHEC. 7th International Conference and Exhibition on Thermoplastic Composites. Bremen, Germany, 09.10.-10.10.2024, pp. 94–97. DOI: 10.24406/h-477934.

Schelleis, C.; Meckes, L.; Henning, F. (2025): Fiber migration in compression molded LFT-D materials: characterization proposal and first results: Material Forming: ESAFORM 2025. The 28th International ESAFORM on Material

Forming. Paestum, Italy, 07.05.-09.05.2025: Materials Research Forum LLC (Materials Research Proceedings, 54), pp. 468–477. DOI: 10.21741/9781644903599-51.

Other proceedings and presentations

Schelleis, C.; Scheuring, B.M.; Hrymak, A.; Henning, F. (2023): Study on mechanical characteristics of glass fiber-reinforced polycarbonate LFT-D for codico structures: Proceedings of the 23rd ICCM. International Conference on Composite Materials. Belfast, UK, 30.07.-04.08.2023. DOI: 10.24406/H-451656.

Schelleis, C.; Hrymak, A.; Henning, F. (2023): Optimizing processing parameters for glass fiber reinforced polycarbonate LFT-D composites: Proceedings of the SAMPE Europe Conference. SAMPE Europe Conference. Madrid, Spain, 03.10.-05.10.2023. DOI: 10.24406/PUBLICA-2084.

Ugresic, V.; Park, D.; Schelleis, C.; Connolly, M.; Henning, F. (2017): New Developments in Polyurethane Sheet Moulding Compound: Proceedings of the 17th Annual SPE ACCE. 17th Annual Automotive Composites Conference and Exhibition. Novi, MI, USA, 06.09.-08.09.2017.

Presentations without proceeding contributions

Schelleis, C. (2024): Polycarbonat im LFT-D Fließpressprozess: Erkenntnisse aus Material- und Prozessentwicklung. Symposium Verbundwerkstoffe und Werkstoffverbunde 2024. Freiburg, Germany, 22.05.2024.

Schelleis, C. (2024): Material- und Prozessentwicklung von glasfaserverstärktem Polyamid 6 im LFT-D Fließpressen. 10. Technologietag Leichtbau. Leichtbau-Allianz Baden-Württemberg. Stuttgart, Germany, 06.11.2024.

Scheuring, B.M.; Schelleis, C.; Liebig, W.V.; Montesano, J.; Weidenmann, K.A. (2023): Effect of Hybridization on the Mechanical Properties of Continuous Discontinuous Long Fiber Reinforced Thermoplastics: Proceedings of the 23rd ICCM. International Conference on Composite Materials. Belfast, UK, 30.07.-04.08.2023.

Supervised student theses

Kobayashi, Y. (2022): Quantifizierung von Faserbündeln in Erzeugnissen des LFT-D Prozesses. Bachelor Thesis (in german). Karlsruhe Institute for Technology, Institut für Fahrzeugsystemtechnik Institutsteil Leichtbau, Karlsruhe, Germany.

Löwe, S. (2023): Charakterisierung des Plastifikates an der Schnittstelle zwischen Compounding und Fließpressen langfaserverstärkter thermoplastischer Formmassen. Bachelor Thesis (in german). Karlsruhe Institute for Technology, Institut für Fahrzeugsystemtechnik Institutsteil Leichtbau, Karlsruhe, Germany.

Meckes, L. (2024): Charakterisierung des LFT-D Plastifikates: Methodenentwicklung und Ermittlung der Prozesszusammenhänge mit Fokus auf die Dichteeigenschaften. Master Thesis (in german). Karlsruhe Institute for Technology, Institut für Fahrzeugsystemtechnik Institutsteil Leichtbau, Karlsruhe, Germany.

Publication Bibliography

Ashby, M.F. (2017): Materials selection in mechanical design. 5th Edition. Amsterdam, Boston, Heidelberg: Butterworth-Heinemann.

AVK-Industrievereinigung Verstärkte Kunststoffe e.V. (Ed.) (2014): Handbuch Faserverbundkunststoffe/Composites. Grundlagen, Verarbeitung, Anwendungen. 4th Edition. Wiesbaden: Springer Vieweg.

Barbosa, S.E.; Kenny, J.M. (2000): Processing of short-fiber reinforced polypropylene. I. Influence of processing conditions on the morphology of extruded filaments. In *Polymer Engineering and Science* 40 (1), pp. 11–22. DOI: https://doi.org/10.1002/pen.11135.

Barmpoutis, A. (2010): Tutorial on Diffusion Tensor MRI using Matlab. Electronic Edition. University of Florida. Available online at abarmpou.github.io, checked on 16.05.2025.

Bechara, A.; Goris, S.; Yanev, A.; Brands, D.; Osswald, T. (2021): Novel modeling approach for fiber breakage during molding of long fiber-reinforced thermoplastics. In *Physics of Fluids* 33 (7), p. 73318. DOI: https://doi.org/10.1063/5.0058693.

Blarr, J.; Kunze, P.; Kresin, N.; Liebig, W.V.; Inal, K.; Weidenmann, K.A. (2024): Novel thresholding method and convolutional neural network for fiber volume content determination from 3D µ CT images. In *NDT & E International* 144, p. 103067. DOI: https://doi.org/10.1016/j.ndteint.2024.103067.

Blarr, J.; Sabiston, T.; Krauß, C.; Bauer, J.K.; Liebig, W.V.; Inal, K.; Weidenmann, K.A. (2023): Implementation and comparison of algebraic and machine learning based tensor interpolation methods applied to fiber orientation tensor fields obtained from CT images. In *Computational Materials Science* 228, p. 112286. DOI: https://doi.org/10.1016/j.commatsci.2023.112286.

Böhlke, T.; Henning, F.; Hrymak, A.; Kärger, L.; Weidenmann, K.; Wood, J.T. (Eds.) (2019): Continuous-discontinuous fiber-reinforced polymers. An integrated engineering approach. Munich: Carl Hanser Verlag.

Bondy, M.; Mohammadkhani, P.; Magliaro, J.; Altenhof, W. (2022): Elevated Strain Rate Characterization of Compression Molded Direct/In-Line Compounded Carbon Fibre/Polyamide 66 Long Fibre Thermoplastic. In *Materials* 15 (21), pp. 7667–7690. DOI: https://doi.org/10.3390/ma15217667.

Bondy, M.; Pinter, P.; Altenhof, W. (2017): Experimental characterization and modelling of the elastic properties of direct compounded compression molded carbon fibre/polyamide 6 long fibre thermoplastic. In *Materials & Design* 122, pp. 184–196. DOI: https://doi.org/10.1016/j.matdes.2017.03.010.

Bondy, M.; Rodgers, W.; Altenhof, W. (2019): Tensile fatigue characterization of polyamide 66/carbon fiber direct/in-line compounded long fiber thermoplastic composites. In *Composites Part B: Engineering* 173, p. 106984. DOI: https://doi.org/10.1016/j.compositesb.2019.106984.

Brast, K. (2001): Verarbeitung von langfaserverstärkten Thermoplasten im direkten Plastifizier-/ Pressverfahren. Dissertation (in german). RWTH Aachen University, Aachen, Germany.

Buck, F.; Brylka, B.; Müller, V.; Müller, T.; Weidenmann, K.A.; Hrymak, A.N. et al. (2015): Two-scale structural mechanical modeling of long fiber reinforced thermoplastics. In *Composites Science and Technology* 117 (1), pp. 159–167. DOI: https://doi.org/10.1016/j.compscitech.2015.05.020.

Bumm, S.H.; White, J.L.; Isayev, A.I. (2012): Glass fiber breakup in corotating twin screw extruder: Simulation and experiment. In *Polymer Composites* 33 (12), pp. 2147–2158. DOI: https://doi.org/10.1002/pc.22356.

Christ, N.; Montesano, J.; Hohe, J. (2023): Experimental investigation of carbon long fiber reinforced polyamide 6 exposed to environmental conditions. In *Proceedings in Applied Mathematics and Mechanics* 22 (1), Article e202200166. DOI: https://doi.org/10.1002/pamm.202200166.

Cox, H.L. (1952): The elasticity and strength of paper and other fibrous materials. In *British Journal of Applied Physics* 3 (3), pp. 72–79.

Dahl, J.; Blanchard, P.; Latimer, T.; Sudrla, J.; Henshaw, J. (2011): A method for characterizing fiber length distribution in random fiber composites: Proceedings of the 11th SPE ACCE. 11th-Annual SPE Automotive Composite Conference and Exhibition. Troy, MI, USA, 13.09.-15.09.2011.

Dahl, J.S.; Blanchard, P.J.; Rodgers, W.R. (2012): Direct compounding of a carbon fiber reinforced polyamide 66 composite: Proceedings of SAMPE North America. SAMPE 2012. Baltimore, MD, USA, 21.5.-24.5.2012.

Devore, J.L.; Berk, K.N.; Carlton, M.A. (2021): Modern Mathematical Statistics with Applications. 3rd Edition. Cham: Springer International Publishing. DOI: https://doi.org/10.1007/978-3-030-55156-8.

Eyerer, P.; Hirth, T.; Elsner, P. (2008): Polymer Engineering. Technologien und Praxis. Berlin, Heidelberg: Springer Berlin Heidelberg. DOI: https://doi.org/10.1007/978-3-540-72419-3.

Eyerer, P.; Krause, W.; Geiger, O.; Henning, F. (2006): Development of a Technology for the Large-Scale Production of Continuous Fiber Reinforced Composites: Proceedings of SPE ANTEC. SPE Annual Technical Conference. Boston, MA, USA, 01.05.-05.05.2006.

Fliegener, S. (2015): Micromechanical finite element modeling of long fiber reinforced thermoplastics. Dissertation (in german). Karlsruhe Institute for Technology, Karlsruhe, Germany. DOI: https://doi.org/10.5445/IR/1000051015.

Folgar, F.; Tucker, C.L. (1984): Orientation Behavior of Fibers in Concentrated Suspensions. In *Journal of Reinforced Plastics and Composites* 3 (2), pp. 98–119. DOI: https://doi.org/10.1177/073168448400300201.

Forgacs, O.; Mason, S. (1959): Particle motions in sheared suspensions. In *Journal of Colloid Science* 14 (5), pp. 457–472. DOI: https://doi.org/10.1016/0095-8522(59)90012-1.

Frankland, J. (2019): Why Barrel Temperatures Have a Small Effect on Melt Temperature. Available online at www.ptonline.com, checked on 16.05.2025.

Gandhi, U.N.; Goris, S.; Osswald, T.A.; Song, Y.-Y. (2020): Discontinuous Fiber-Reinforced Composites. Fundamentals and applications. Munich, Germany: Hanser Publishers. DOI: https://doi.org/10.3139/9781569906958.fm.

Garesci, F.; Fliegener, S. (2013): Young's modulus prediction of long fiber reinforced thermoplastics. In *Composites Science and Technology* 85, pp. 142–147. DOI: https://doi.org/10.1016/j.compscitech.2013.06.009.

Geiger, O.; Henning, F.; Eyerer, P.; Brüssel, R.; Ernst, H. (2006): LFT-D: materials tailored for new applications. In *Reinforced Plastics* 50 (1), pp. 30–35. DOI: https://doi.org/10.1016/S0034-3617(06)70870-0.

Gogoi, B.K.; Yam, K.L. (1994): Relationships between residence time and process variables in a corotating twin-screw extruder. In *Journal of Food Engineering* 21 (2), pp. 177–196. DOI: https://doi.org/10.1016/0260-8774(94)90185-6.

Goris, S.; Back, T.; Yanev, A.; Brands, D.; Drummer, D.; Osswald, T.A. (2018): A novel fiber length measurement technique for discontinuous fiber-reinforced composites: A comparative study with existing methods. In *Polymer Composites* 39 (11), pp. 4058–4070. DOI: https://doi.org/10.1002/pc.24466.

Goris, S.; Osswald, T.A. (2018): Process-induced fiber matrix separation in long fiber-reinforced thermoplastics. In *Composites Part A: Applied Science and Manufacturing* 105, pp. 321–333. DOI: https://doi.org/10.1016/j.compositesa.2017.11.024.

Grellmann, W.; Seidler, S. (Eds.) (2022): Polymer testing. With assistance of V. Altstädt, M. Bauer, C. Bierögel. 3rd Edition. Munich, Germany: Hanser.

Halpin, J.C.; Pagano, N.J. (1969): The Laminate Approximation for Randomly Oriented Fibrous Composites. In *Journal of Composite Materials* 3 (4), pp. 720–724. DOI: https://doi.org/10.1177/002199836900300416.

Hartwich, M.R.; Höhn, N.; Mayr, H.; Sandau, K.; Stengler, R. (2009): FASEP ultra-automated analysis of fibre length distribution in glass-fibre-reinforced products: Optical Measurement Systems for Industrial Inspection

VI. SPIE Europe Optical Metrology. Munich, Germany, 15.06.2009, p. 738921. DOI: https://doi.org/10.1117/12.827503.

Henning, F. (2001): Verfahrensentwicklung für lang- und endlosglasfaserverstärkte thermoplastische Sandwich-Bauteile mit geschlossenem Werkstoff-Kreislauf. Dissertation (in german). Stuttgart University, Stuttgart, Germany.

Henning, F.; Ernst, H.; Brüssel, R. (2005): LFTs for automotive applications. In *Reinforced Plastics* 49 (2), pp. 24–33.

Henning, F.; Moeller, E. (2020): Handbuch Leichtbau. Methoden, Werkstoffe, Fertigung. 2nd Edition. München, Wien: Hanser.

Hirata, K.; Ishida, H.; Hiragohri, M.; Nakayama, Y.; Kajiwara, T. (2013): Experimental Assessment of Dispersion Failure of Glass Fiber Reinforced Plastics in a Twin Screw Extruder. In *International Polymer Processing* 28 (4), pp. 368–375. DOI: https://doi.org/10.3139/217.2704.

Hümbert, S. (2016): Influence of the Screw Configuration on the LFT-D Processing of Glass Fiber Reinforced PA6. Master Thesis. Karlsruhe Institute for Technology, Institut für Fahrzeugsystemtechnik Institutsteil Leichtbau, Karlsruhe, Germany.

Huq, A.; Azaiez, J. (2005): Effects of length distribution on the steady shear viscosity of semiconcentrated polymer-fiber suspensions. In *Polymer Engineering and Science* 45 (10), pp. 1357–1368. DOI: https://doi.org/10.1002/pen.20415.

Inceoglu, F.; Ville, J.; Ghamri, N.; Pradel, J.L.; Durin, A.; Valette, R.; Vergnes, B. (2011): Correlation between processing conditions and fiber breakage during compounding of glass fiber-reinforced polyamide. In *Polymer Composites* 32 (11), pp. 1842–1850. DOI: https://doi.org/10.1002/pc.21217.

Jeffery, G.B. (1922): The motion of ellipsoidal particles immersed in a viscous fluid. In *Proceedings of the Royal Society of London. Series A. Mathematical and Physical Sciences* 102 (715), pp. 161–179. DOI: https://doi.org/10.1098/rspa.1922.0078.

Kampker, A.; Heimes, H.H. (2024): Elektromobilität. Grundlagen einer Fortschrittstechnologie. 3rd Edition. Berlin, Heidelberg: Springer Vieweg. DOI: https://doi.org/10.1007/978-3-662-65812-3.

Kelly, A.; Tyson, W.R. (1965): Tensile properties of fibre-reinforced metals: Copper/tungsten and copper/molybdenum. In *Journal of the Mechanics and Physics of Solids* 13 (6), pp. 329–350. DOI: https://doi.org/10.1016/0022-5096(65)90035-9.

Khapra, T.; Altenhof, J.; Beigpour, R.; Dehghanpour, S.; Mohammadkhani, P.; Bondy, M.; Altenhof, W. (2025): Influence of fibre content, moisture content, and anisotropy on the mechanical properties of direct compounded compression moulded carbon/PA66 and glass/PA6 composites. In *Journal of Thermoplastic Composite Materials*, Article 08927057251325166. DOI: https://doi.org/10.1177/08927057251325166.

Kloke, P.; Rudloff, J.; Schöppner, V.; Potente, H.; Kretschmer, K.; Heidemeyer, P.; Bastian, M. (2011): Faserschonend compoundieren. In *Kunststoffe* (2), pp. 66–69.

Knutsson, B.A.; White, J.L.; Abbas, K.B. (1981): Rheological and extrusion characteristics of glass fiber-reinforced polycarbonate. In *Journal of Applied Polymer Science* 26 (7), pp. 2347–2362. DOI: https://doi.org/10.1002/app.1981.070260721.

Kohlgrüber, K. (Ed.) (2016): Der gleichläufige Doppelschneckenextruder. Grundlagen, Technologie, Anwendungen. With assistance of M. Ullrich, R. Rudolf, T. König. 2nd Edition. Munich, Germany: Hanser.

Kohlgrüber, K. (2020): Co-Rotating Twin-Screw Extruders - Two Volume Set. München: Carl Hanser Verlag GmbH & Co. KG.

Krause, W.; Henning, F.; Tröster, S.; Geiger, O.; Eyerer, P. (2003): LFT-D — A Process Technology for Large Scale Production of Fiber Reinforced Thermoplastic Components. In *Journal of Thermoplastic Composite Materials* 16 (4), pp. 289–302. DOI: https://doi.org/10.1177/0892705703016004001.

Kuroda, M.M.H.; Scott, C.E. (2002): Initial dispersion mechanisms of chopped glass fibers in polystyrene. In *Polymer Composites*, pp. 395–405. DOI: https://doi.org/10.1002/pc.10441.

Lankford, W.T.; Snyder, S.C.; Bausher, J.A. (1950): New criteria for predicting the press performance of deep drawing steels. In *Transactions of the American Mathematical Society* 42, pp. 1197–1205.

Laun, H.M. (1984): Orientation effects and rheology of short glass fiber-reinforced thermoplastics. In *Colloid & Polymer Science* 262 (4), pp. 257–269. DOI: https://doi.org/10.1007/BF01410464.

Löwe, S. (2022): Charakterisierung des Plastifikates an der Schnittstelle zwischen Compounding und Fließpressen langfaserverstärkter thermoplastischer Formmassen. Bachelor Thesis (in german). Karlsruhe Institute for Technology, Institut für Fahrzeugsystemtechnik Institutsteil Leichtbau, Karlsruhe, Germany. DOI: https://doi.org/10.24406/publica-785.

Maertens, R. (2022): Process Development and Material Characterization for the Injection Molding of Long Glass Fiber-Reinforced Phenol Formaldehyde Resins. Dissertation. Karlsruhe Institute for Technology, Karlsruhe, Germany. DOI: https://doi.org/10.5445/IR/1000153438.

Maertens, R.; Liebig, W.V.; Elsner, P.; Weidenmann, K.A. (2021): Compounding of Short Fiber Reinforced Phenolic Resin by Using Specific Mechanical Energy Input as a Process Control Parameter. In *Journal of Composites Science* 5 (5), p. 127. DOI: https://doi.org/10.3390/jcs5050127.

Mavridis, H.; Bruce, G.D.; Vancso, G.J.; Weatherly, G.C.; Vlachopoulos, J. (1992): Deformation patterns in the compression of polypropylene disks: Experiments and simulation. In *Journal of Rheology* 36 (1), pp. 27–43. DOI: https://doi.org/10.1122/1.550340.

McLeod, M.; Hétu, J.-F.; Deaville, T.; Bureau, M.; Baril, E. (2010): Morphological and Mechanical Comparision of Injection and Compression Moulding In-Line Compounding of Direct Long Fibre Thermoplastics: Advances in Thermoplastic Composites. 10th-Annual SPE Automotive Composite Conference and Exhibition. Troy, MI, USA, 15.9.-16.9.2010, pp. 109–119.

Meckes, L. (2024): Charakterisierung des LFT-D Plastifikates: Methodenentwicklung und Ermittlung der Prozesszusammenhänge mit Fokus auf die Dichteeigenschaften. Master Thesis (in german). Karlsruhe Institute for Technology, Institut für Fahrzeugsystemtechnik Institutsteil Leichtbau, Karlsruhe, Germany. DOI: https://doi.org/10.24406/h-477101.

Meierhans, M. (2022): Charakterisierung der richtungsabhängigen mechanischen Eigenschaften von glasfaserverstärktem Polycarbonat im LFT-D Prozess. Bachelor Thesis (in german). Karlsruhe Institute for Technology, Institut für Angewandte Materialien, Karlsruhe, Germany.

Mohammadkhani, P.; Magliaro, J.; Rahimidehgolan, F.; Khapra, T.; Altenhof, W. (2023): Moisture influence on anisotropic mechanical behavior of direct compounded compression molded PA6/Glass LFTs. In *Composites Part B: Engineering* 264, p. 110927. DOI: https://doi.org/10.1016/j.compositesb.2023.110927.

Nghiep Nguyen, B.A.; Bapanapalli, S.K.; Kunc, V.; Phelps, J.H.; Tucker, C.L. (2009): Prediction of the Elastic—Plastic Stress/Strain Response for Injection-Molded Long-Fiber Thermoplastics. In *Journal of Composite Materials* 43 (3), pp. 217–246. DOI: https://doi.org/10.1177/0021998308099219.

Nguyen, B.N.; Bapanapalli, S.K.; Holbery, J.D.; Smith, M.T.; Kunc, V.; Frame, B.J. et al. (2008): Fiber Length and Orientation in Long-Fiber Injection-Molded Thermoplastics — Part I: Modeling of Microstructure and Elastic Properties. In *Journal of Composite Materials* 42 (10), pp. 1003–1029. DOI: https://doi.org/10.1177/0021998308088606.

Ning, H.; Lu, N.; Hassen, A.A.; Chawla, K.; Selim, M.; Pillay, S. (2020): A review of Long fibre thermoplastic (LFT) composites. In *International Materials Reviews* 65 (3), pp. 164–188. DOI: https://doi.org/10.1080/09506608.2019.1585004.

Oelgarth, A.; Dittmar, H.; Stockreiter, W.; Wald, H.H. (1998): GMT oder LFT : Eine vergleichende Betrachtung langfaserverstärkter Thermoplaste. In *Kunststoffe* 88 (4), 480-486.

O'Neill, B.C.; Oppenheimer, M. (2002): Climate change. Dangerous climate impacts and the Kyoto Protocol. In *Science* 296 (5575), pp. 1971–1972. DOI: https://doi.org/10.1126/science.1071238.

Osswald, T. (2018): Understanding Polymer Processing. Processes and Governing Equations. Munich, Germany: Hanser. DOI: https://doi.org/10.3139/9781569906484.fm.

Osswald, T.A. (2014): Fiber Orientation and Warpage Prediction of DLFT/Thermoplastic Fiber Mats Hybrid Parts. Simulation and Experimental Validation. WAK-Symposium. Karlsruhe, Germany, 20.05.2014.

Osswald, T.A.; Menges, G. (2012): Materials science of polymers for engineers. 3rd Edition. Munich, Germany: Hanser. DOI: https://doi.org/10.3139/9781569905241.

Perez, C.; Osswald, T.; Goris, S. (2013): Study on the fiber properties of a LFT strand: Proceedings of the 13th Annual SPE ACCE. 13th Annual SPE Automotive Composite Conference and Exhibition. Novi, MI, USA, 11.09.-13.09.2013, pp. 1115–1126.

Pinter, P.; Dietrich, S.; Bertram, B.; Kehrer, L.; Elsner, P.; Weidenmann, K.A. (2018): Comparison and error estimation of 3D fibre orientation analysis of computed tomography image data for fibre reinforced composites. In *NDT & E International* 95, pp. 26–35. DOI: https://doi.org/10.1016/j.ndteint.2018.01.001.

Priebe, M.; Schledjewski, R. (2011): Processing and properties of glass/polypropylene in long fibre compounding extrusion. In *Plastics, Rubber and Composites* 40 (6-7), pp. 374–379. DOI: https://doi.org/10.1179/1743289810Y.0000000035.

ISO 80000-1: Quantities and units. DOI: https://doi.org/10.31030/2007309.

Radtke, A. (2009): Steifigkeitsberechnung von diskontinuierlich faserverstärkten Thermoplasten auf der Basis von Faserorientierungs- und Faserlängenverteilungen. Dissertation (in german). Stuttgart University, Stuttgart, Germany. DOI: https://doi.org/10.18419/opus-1788.

Rohan, K.; McDonough, T.J.; Ugresic, V.; Potyra, E.; Henning, F. (2014): Mechanical study of direct long fiber thermoplastic carbon/polyamide 6 and its relations to processing parameters: Proceedings of the 14th Annual SPE ACCE. 14th Annual SPE Automotive Composites Conference and Exhibition. Novi, MI, USA, 09.09.-11.09.2014.

Rohde-Tibitanzl, M. (2015): Direct Processing of Long Fiber Reinforced Thermoplastic Composites and their Mechanical Behavior under Static and Dynamic Load. Cincinnati, OH, USA: Hanser Publications. DOI: https://doi.org/10.3139/9781569906309.fm.

S. Tsai; N. Pagano (1968): Invariant properties of composite materials.

Schelleis, C.; Hrymak, A.; Henning, F. (2023a): Optimizing processing parameters for glass fiber reinforced polycarbonate LFT-D composites: Proceedings of the SAMPE Europe Conference. SAMPE Europe Conference. Madrid, Spain, 03.10.-05.10.2023. DOI: https://doi.org/10.24406/PUBLICA-2084.

Schelleis, C.; Meckes, L.; Henning, F. (2025a): Fiber migration in compression molded LFT-D materials: characterization proposal and first results: Material Forming: ESAFORM 2025. The 28th International ESAFORM on Material Forming. Paestum, Italy, 07.05.-09.05.2025: Materials Research Forum LLC (Materials Research Proceedings, 54), pp. 468–477. DOI: https://doi.org/10.21741/9781644903599-51.

Schelleis, C.; Scheuring, B.M.; Hrymak, A.; Henning, F. (2023b): Study on mechanical characteristics of glass fiber-reinforced polycarbonate LFT-D for codico structures: Proceedings of the 23rd ICCM. International Conference on Composite Materials. Belfast, UK, 30.07.-04.08.2023. DOI: https://doi.org/10.24406/H-451656.

Schelleis, C.; Scheuring, B.M.; Liebig, W.V.; Hrymak, A.N.; Henning, F. (2023c): Approaching Polycarbonate as an LFT-D Material: Processing and Mechanical Properties. In *Polymers* 15 (9), pp. 2041–2065. DOI: https://doi.org/10.3390/polym15092041.

Schelleis, C.; Scheuring, B.M.; Schreyer, L.; Liebig, W.V.; Hrymak, A.; Kärger, L. et al. (2025b): Skewness of Flow Front and Fiber Orientation in

LFT-D Compression Molding considering Processing, Characterization and Simulation. in press. In *Journal of Thermoplastic Composite Materials*. DOI: https://doi.org/10.1177/08927057251344252.

Schemme, M. (2008): LFT – development status and perspectives. In *Reinforced Plastics* 52 (1), pp. 32–39. DOI: https://doi.org/10.1016/S0034-3617(08)70036-5.

Scheuring, B.M. (2024): Effect of hybridization in CoDico-FRTPs. Orientation-dependent characterization and analytical modeling in various climatic conditions. Dissertation. Karlsruhe Institute for Technology, Karlsruhe, Germany. DOI: https://doi.org/10.5445/IR/1000177112.

Scheuring, B.M.; Christ, N.; Blarr, J.; Liebig, W.V.; Hohe, J.; Montesano, J.; Weidenmann, K.A. (2024): Experimental and homogenized orientation-dependent properties of hybrid long fiber-reinforced thermoplastics. In *International Journal of Mechanical Sciences* 280, pp. 109470–109488. DOI: https://doi.org/10.1016/j.ijmecsci.2024.109470.

Schreyer, L.; Blarr, J.; Höger, K.; Meyer, N.; Kärger, L. (2022): Generation of Initial Fiber Orientation States for Long Fiber Reinforced Thermoplastic Compression Molding Simulation: Proceedings of the 20th ECCM. 20th European Conference on Composite Materials. Lausanne, Switzerland, 26.06.-30.06.2022. DOI: https://doi.org/10.5445/IR/1000155599.

Siebertz, K.; van Bebber, D.; Hochkirchen, T. (2017): Statistische Versuchsplanung. Design of Experiments (DoE). 2nd Edition. Berlin, Heidelberg, Germany: Springer Vieweg. DOI: https://doi.org/10.1007/978-3-662-55743-3.

Smith, G.; Zhao, H.; Shewey, M. (2020): Direct compounding and compression molding of carbon and glass fiber reinforced polyamide 66 – tensile and compressive test results: Proceedings of the 20th Annual SPE ACCE. 20th Annual SPE Automotive Composite Conference and Exhibition. Virtual Conference, 09.09.-11.09.2020.

Song, Y.; Gandhi, U.; Pérez, C.; Osswald, T.; Vallury, S.; Yang, A. (2017): Method to account for the fiber orientation of the initial charge on the fiber orientation of finished part in compression molding simulation. In

Composites Part A: Applied Science and Manufacturing 100, pp. 244–254. DOI: https://doi.org/10.1016/j.compositesa.2017.05.021.

Stratiychuk-Dear, D.; Looney, K.; Oliver, P.; Blackburn, S.; Simmons, M. (2017): Investigating the impact of operating conditions on the extent of additive mixing during thermoplastic polymer extrusion. In *AIP Conference Proceedings* 1914 (1), p. 150002. DOI: https://doi.org/10.1063/1.5016779.

Student (1908): The Probable Error of a Mean. In *Biometrika* 6 (1), p. 1. DOI: https://doi.org/10.2307/2331554.

Tadmor, Z. (1974): Molecular orientation in injection molding. In *Journal of Applied Polymer Science* 18 (6), pp. 1753–1772. DOI: https://doi.org/10.1002/app.1974.070180614.

Teschner, R. (2021): Glasfasern. 3rd Edition. Berlin, Heidelberg, Germany: Springer. DOI: https://doi.org/10.1007/978-3-662-64123-1.

Thattaiparthasarathy, K.B.; Pillay, S.; Ning, H.; Vaidya, U.K. (2008): Process simulation, design and manufacturing of a long fiber thermoplastic composite for mass transit application. In *Composites Part A: Applied Science and Manufacturing* 39 (9), pp. 1512–1521. DOI: https://doi.org/10.1016/j.compositesa.2008.05.017.

The European Parliament and the Council of the European Union (2/20/2024): Regulation (EU) 2023/851. In *Official Journal of the European Union*. Available online at data.europa.eu.

Thomason, J.L. (2002): The influence of fibre length and concentration on the properties of glass fibre reinforced polypropylene: 5. Injection moulded long and short fibre PP. In *Composites Part A: Applied Science and Manufacturing* 33 (12), pp. 1641–1652. DOI: https://doi.org/10.1016/S1359-835X(02)00179-3.

Thomason, J.L. (2005): The influence of fibre length and concentration on the properties of glass fibre reinforced polypropylene. 6. The properties of injection moulded long fibre PP at high fibre content. In *Composites Part A: Applied Science and Manufacturing* 36 (7), pp. 995–1003. DOI: https://doi.org/10.1016/j.compositesa.2004.11.004.

Thomason, J.L. (2006): Structure-property relationships in glass-reinforced polyamide, part 1: The effects of fiber content. In *Polymer Composites* 27 (5), pp. 552–562. DOI: https://doi.org/10.1002/pc.20226.

Thomason, J.L. (2007): Structure–property relationships in glass reinforced polyamide, part 2: The effects of average fiber diameter and diameter distribution. In *Polymer Composites* 28 (3), pp. 331–343. DOI: https://doi.org/10.1002/pc.20260.

Thomason, J.L.; Groenewoud, W.M. (1996): The influence of fibre length and concentration on the properties of glass fibre reinforced polypropylene: 2. Thermal properties. In *Composites Part A: Applied Science and Manufacturing* 27 (7), pp. 555–565. DOI: https://doi.org/10.1016/1359-835X(96)00016-4.

Thomason, J.L.; Vlug, M.A. (1996): Influence of fibre length and concentration on the properties of glass fibre-reinforced polypropylene: 1. Tensile and flexural modulus. In *Composites Part A: Applied Science and Manufacturing* 27 (6), pp. 477–484. DOI: https://doi.org/10.1016/1359-835X(95)00065-A.

Thomason, J.L.; Vlug, M.A. (1997): Influence of fibre length and concentration on the properties of glass fibre-reinforced polypropylene: 4. Impact properties. In *Composites Part A: Applied Science and Manufacturing* 28 (3), pp. 277–288. DOI: https://doi.org/10.1016/S1359-835X(96)00127-3.

Thomason, J.L.; Vlug, M.A.; Schipper, G.; Krikor, H. (1996): Influence of fibre length and concentration on the properties of glass fibre-reinforced polypropylene: Part 3. Strength and strain at failure. In *Composites Part A: Applied Science and Manufacturing* 27 (11), pp. 1075–1084. DOI: https://doi.org/10.1016/1359-835X(96)00066-8.

Tozzi, E.J.; Lavenson, D.M.; McCarthy, M.J.; Powell, R.L. (2013): Effect of fiber length, flow rate, and concentration on velocity profiles of cellulosic fiber suspensions. In *Acta Mechanica* 224 (10), pp. 2301–2310. DOI: https://doi.org/10.1007/s00707-013-0922-2.

Tröster, S. (2004): Materialentwicklung und -charakterisierung für thermoplastische Faserverbundwerkstoffe im Direktverfahren. Dissertation (in german). Stuttgart University, Stuttgart, Germany.

Truckenmüller, F. (1996): Direktverarbeitung von Endlosfasern auf Spritzgießmaschinen. Möglichkeiten und Grenzen. Düsseldorf, Germany: VDI-Verlag (Fortschritt-Berichte VDI Reihe 3, Verfahrenstechnik, 444).

Truckenmüller, F.; Fritz, H.-G. (1991): Injection molding of long fiber-reinforced thermoplastics: A comparison of extruded and pultruded materials with direct addition of roving strands. In *Polymer Engineering & Science* 31 (18), pp. 1316–1329. DOI: https://doi.org/10.1002/pen.760311806.

Tucker, C.L. (2022): Fundamentals of fiber orientation. Description, measurement and prediction. Munich, Germany: Hanser Publishers. DOI: https://doi.org/10.1016/C2021-0-01120-2.

Ville, J.; Inceoglu, F.; Ghamri, N.; Pradel, J.L.; Durin, A.; Valette, R.; Vergnes, B. (2013): Influence of Extrusion Conditions on Fiber Breakage along the Screw Profile during Twin Screw Compounding of Glass Fiber-reinforced PA. In *International Polymer Processing* 28 (1), pp. 49–57. DOI: https://doi.org/10.3139/217.2659.

Wackernagel, M.; Schulz, N.B.; Deumling, D.; Linares, A.C.; Jenkins, M.; Kapos, V. et al. (2002): Tracking the ecological overshoot of the human economy. In *Proceedings of the National Academy of Sciences of the United States of America* 99 (14), pp. 9266–9271. DOI: https://doi.org/10.1073/pnas.142033699.

Willems, F.; Reitinger, P.; Bonten, C. (2020): Calibration of Fiber Orientation Simulations for LFT—A New Approach. In *Journal of Composites Science* 4 (4), p. 163. DOI: https://doi.org/10.3390/jcs4040163.

Witten, E.; Mathes, V. (2023): The European Market for Fibre-Reinforced Plastics and Composites 2022. Market developments, trends, challenges and outlook. In *AVK Market Report*.

Yilmazer, U.; Cansever, M. (2002): Effects of processing conditions on the fiber length distribution and mechanical properties of glass fiber reinforced nylon-6. In *Polymer Composites* 23 (1), pp. 61–71. DOI: https://doi.org/10.1002/pc.10412.

Appendix

Table A.1 Processing approach. This list indicates when samples are produced, and measurements are taken.

Setup of all machines according to trial plan. • Document all settings	
Start LFT-D line (t = 0 min) and logging of machine data	
Adjust n_{rov} to trial plan. • Start run-in time ($t_{run\text{-}in}$ = 20 min) • Check temperature T_{Z15} and M_{TSE2} for equilibrium	
Measure fiber intake speed	v_{intake}
Determine nominal LFT-D length	$l_{plas,nominal}$

Measure mold temperature at start of molding (t = 20 min+).	$T_{mold,u}$ and $T_{mold,l}$
Alternating production • 7 plates • 7 plastificates	
Production of 10 plates	All mechanical samples
Measure mold temperature at end of molding	$T_{mold,u}$ and $T_{mold,l}$

Preparation of the mold for flow front study	
Measure plastificate temperatures	$T_{plas,o}$ and $T_{plas,n}$

Flow front study • 6 plates	s_{ff}
Sampling plastificate fiber length	$l_{f,plas}$
Residence time study with pigment	t_{res}, plastificate fiber orientation
End logging LFT-D data	M_{TSE2}, T_{Z15}

Dead stop of LFT-D line for fiber length sampling in TSE2	
Sampling position 1 fiber intake	l_f
Sampling position 2 mixing element	l_f

Table A.2 FASEP results l_n, l_w and p sorted by $w_{f,mean}$.

$w_{f,mean}$ in %	Run order/ remarks	$l_{n,mean}$ in mm	CV in %	l_w in mm	CV in %	p
18.29[S]	V12	1.29	15	3.72	17	2.9
18.81	V13	1.46	13	3.90	13	2.7
19.63	V16	1.14	8	3.23	20	2.8
22.79	V15	1.20	11	3.88	26	3.2
24.89	V5	1.02	34	4.07	18	4.0
25.32	V9	1.10	19	4.05	15	3.7
30.53[S,C]	V10	1.25	9	4.17	20	3.3
30.93[C]	V6	1.00	28	3.74	27	3.7
31.19[C]	V3	1.15	14	3.84	22	3.3
33.50	V14	1.00	8	3.60	30	3.6
37.57	V2	0.88	14	3.58	30	4.1
39.22	V11	0.82	12	2.93	25	3.6
40.72	V1	0.83	19	3.45	29	4.1
40.76	V4	0.93	8	3.89	13	4.2
41.01	V17	0.91	9	3.38	14	3.7
57.95[S]	V7	0.57	7	2.55	50	4.4

[S] selected parameter set; [C] center point parameter set

Table A.3 Results of tensile characterization, Young's modulus E, tensile strength σ and ultimate strain ε in the C area sorted by $w_{f,mean}$.

$w_{f,mean}$ in %	Young's modulus in GPa	SD in GPa	Tensile strength in MPa	SD in MPa	Ultimate strain ε in %
18.29[S]	6.84	0.27	101.7	3.7	1.65
18.81	6.84	0.40	72.0	2.4	1.15
19.63	6.92	0.51	75.0	4.7	1.18
22.79	7.12	0.35	99.0	8.4	1.53
24.89	7.89	0.14	98.3	3.6	1.40
25.32	7.97	0.39	87.4	2.5	1.21
30.53[S,C]	9.86	0.86	104.0	7.3	1.15
30.93[C]	9.60	0.85	100.0	12.9	1.10
31.19[C]	8.86	0.55	103.0	3.6	1.25
33.50	8.97	0.24	99.0	10.6	1.17
37.57	10.37	0.67	130.0	8.3	1.37
39.22	11.21	0.66	142.8	2.6	1.44
40.72	12.13	0.97	142.9	12.6	1.43
40.76	12.34	0.63	149.0	12.3	1.37
41.01	12.18	0.43	143.9	4.7	1.38
57.95[S]	16.99	1.69	198.0	6.4	1.46

[S] selected parameter set; [C] center point parameter set

Table A.4 Results of tensile characterization, Young's modulus E, tensile strength σ and ultimate strain ε in the F area sorted by $w_{f,mean}$.

$w_{f,mean}$ in %	Young's modulus in GPa	SD in GPa	Tensile strength in MPa	SD in MPa	Ultimate strain ε in %
18.29[S]	6.59	0.08	73.3	6.4	1.15
18.81	7.16	0.42	100.0	6.0	1.57
19.63	7.31	0.38	105.0	5.0	1.61
22.79	8.61	0.57	123.0	4.0	1.58
24.89	8.38	0.82	130.0	16.0	1.69
25.32	9.12	0.59	120.0	13.0	1.48
30.53[S,C]	10.97	0.75	123.0	6.0	1.23
30.93[C]	11.24	0.74	142.0	19.0	1.47
31.19[C]	10.28	0.78	136.0	8.0	1.51
33.50	10.64	0.89	134.0	11.0	1.52
37.57	13.26	0.39	164.0	22.0	1.34
39.22	12.19	1.36	134.9	21.0	1.26
40.72	13.77	1.28	185.4	15.6	1.26
40.76	13.31	0.94	178.2	6.5	1.54
41.01	14.38	0.26	191.0	18.0	1.55
57.95[S]	19.99	1.43	229.0	23.0	1.49

[S] selected parameter set; [C] center point parameter set

Table A.5 Results of flexural characterization, flexural modulus E_F, flexural strength σ_F and ultimate strain ε in the C area sorted by $w_{f,mean}$.

$w_{f,mean}$ in %	Flexural modulus in GPa	SD in GPa	Flexural strength in MPa	SD in MPa	Bending strain ε_f in %
18.29[S]	4.69	0.18	101.0	9.6	2.11
18.81	4.57	0.41	102.0	16.6	2.04
19.63	4.56	0.22	106.8	4.2	2.18
22.79	4.53	0.22	134.2	4.2	2.56
24.89	4.59	0.21	138.0	8.8	2.47
25.32	5.35	0.05	124.0	2.8	2.29
30.53[S,C]	5.69	0.06	118.3	1.4	2.31
30.93[C]	5.07	0.24	119.4	3.3	2.21
31.19[C]	5.55	0.42	141.0	11.0	2.34
33.50	5.97	0.21	134.0	7.1	2.40
37.57	4.92	0.25	141.0	6.4	2.74
39.22	6.40	0.24	150.3	9.1	2.49
40.72	7.10	0.05	190.0	7.2	2.88
40.76	6.41	0.25	168.8	2.1	2.57
41.01	6.37	0.62	163.0	9.8	2.62
57.95[S]	11.24	1.08	265.9	8.7	2.73

[S] selected parameter set; [C] center point parameter set

Table A.6 Results of flexural characterization, flexural modulus E_F, flexural strength σ_F and ultimate strain ε in the F area sorted by $w_{f,mean}$.

$w_{f,mean}$ in %	Young's modulus in GPa	SD in GPa	Tensile strength in MPa	SD in MPa	Ultimate strain ε in %
18.29[S]	6.54	0.26	162.9	3.0	2.52
18.81	6.55	0.60	193.8	31.9	2.57
19.63	6.43	0.15	162.4	9.9	2.45
22.79	7.52	0.16	207.4	7.6	2.71
24.89	6.17	0.29	190.7	7.0	2.60
25.32	8.37	0.41	210.6	1.8	2.48
30.53[S,C]	9.88	0.61	246.1	9.3	2.59
30.93[C]	9.27	0.43	249.5	9.3	2.65
31.19[C]	8.92	0.09	269.5	31.0	2.78
33.50	9.43	0.46	243.8	21.7	2.72
37.57	10.51	0.85	309.3	24.7	2.98
39.22	11.22	0.63	293.8	14.8	2.64
40.72	12.13	0.97	334.7	27.8	2.93
40.76	12.59	0.51	327.7	23.5	2.71
41.01	13.65	0.46	350.4	15.8	2.63
57.95[S]	17.12	1.08	373.8	21.2	2.51

[S] selected parameter set; [C] center point parameter set

Table A.7 Results of impact characterization, impact strength σ_I in the C and F area sorted by $w_{f,mean}$.

$w_{f,mean}$ in %	Impact strength charge in kJ/m²	SD in GPa	Impact strength flow in kJ/m²	SD in MPa
18.29[S]	20.38	4.53	27.1	5.0
18.81	24.43	6.26	33.6	6.1
19.63	23.05	6.20	28.4	2.3
22.79	29.03	7.11	44.7	4.8
24.89	28.30	2.65	36.6	4.1
25.32	31.54	2.88	39.5	4.3
30.53[S,C]	47.60	6.84	61.5	9.2
30.93[C]	41.33	6.40	56.9	11.9
31.19[C]	44.29	9.71	60.0	11.7
33.50	37.50	8.66	59.5	8.2
37.57	54.93	10.76	78.7	4.9
39.22	52.73	10.46	77.3	13.7
40.72	57.93	5.53	80.8	9.7
40.76	55.52	12.20	70.5	5.9
41.01	54.4	4.6	76.70	9.43
57.95[S]	62.08	26.72	68.7	7.4

[S] selected parameter set; [C] center point parameter set

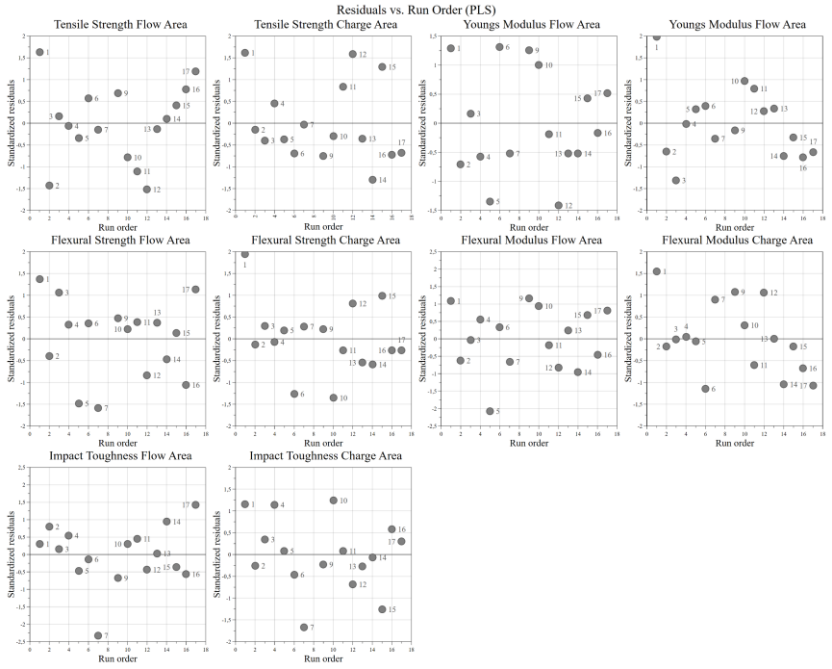

Figure A.1 Residuals vs. run order plots for tensile, flexural and impact properties in C and F area.